University of Southampton

Faculty of Engineering, Science and Mathematics

School of Ocean and Earth Science

Is the Indian Ocean MOC driven by internal wave breaking?

by

Tycho Nout Huussen

Thesis for the degree of Doctor of Philosophy

June 2010

University of Southampton

ABSTRACT

School of Ocean and Earth Science
National Oceanography Centre, Southampton

Doctor of Philosophy

Is the Indian Ocean MOC driven by internal wave breaking?

by Tycho Nout Huussen

This dissertation investigates the energetics of the Indian Ocean Meridional Overturning Circulation (MOC) using hydrographic data (Part I), and the interaction between a broad band internal wave field and a mean flow using idealized numerical simulations (Part II). The main objective of this work is to quantify how much energy is needed to drive the Indian Ocean MOC and to compare this with the energy available in the internal wave field. The turbulent dissipation needed to sustain the MOC is estimated by assuming a 'mixing efficiency' of 0.2 and an advective–diffusive balance in neutral density layers. The advective transport of mass into this box-model is based on published estimates of the flow field at 32°S and the Indonesian Throughflow. A comparison of the large scale dissipation rates with estimates of the input of energy by the tides and the wind shows that most published overturning solutions require more energy than is likely to be available. This result suggests that energy budgets may be useful as constraints in inverse models. Estimates of turbulent dissipation due to internal wave breaking are inferred from in-situ observations of shear and strain using a fine scale parameterization. The isoneutral mean of the inferred internal wave dissipation rates is about one order of magnitude smaller than dissipation rates inferred from the large scale flow fields. This result appears robust when considering potential sampling biases in the internal wave observations and leads to the main conclusion of this work: the Indian Ocean MOC cannot primarily be driven by internal wave breaking. A preliminary investigation into other processes capable of dissipating energy in the ocean interior shows that the MOC may be closed by hydraulic turbulence in the numerous Fracture Zones in the Indian Ocean.

Thesis supervisor: Alberto Naveira-Garabato

Contents

Abstract **i**

Abbreviations **xvii**

Acknowledgements **xviii**

1 Introduction **1**

I MOC energetics **7**

2 Large scale box-model **8**
2.1 Introduction 8
2.2 Methods 9
2.2.1 Advection–diffusion balance 9
2.2.2 Mass transport into density layers 13
2.2.3 Turbulent dissipation 15
2.3 Data 16
2.3.1 Hydrography at 32°S 18
2.3.2 Transport across 32°S 19
2.3.3 Indonesian Throughflow (ITF) 24
2.3.4 Red Sea (RS) and Persian Gulf (PG) 25
2.3.5 Climatology 27
2.4 Errors 28
2.4.1 Inverse model errors 28
2.4.2 Interpolation errors 31
2.4.3 Neutral density errors 32
2.4.4 Error propagation 32
2.5 Results 33
2.5.1 Transport into density layers 33
2.5.2 Turbulent mass transport 37
2.5.3 Turbulent dissipation and diffusivity 41
2.6 Discussion 44
2.7 Summary and conclusion 47

3 Fine scale observations **50**
3.1 Introduction . . . 50
3.2 Methods . . . 51
3.2.1 Finescale parameterization of turbulent dissipation . . 51
3.2.2 Normalization of variance spectra . . . 55
3.2.3 Spectral corrections . . . 56
3.2.4 Buoyancy frequency and strain . . . 57
3.2.5 Shear-to-strain ratio . . . 58
3.2.6 Summary of model configuration . . . 60
3.3 Data . . . 61
3.4 Results . . . 62
3.4.1 Shear and strain spectra . . . 62
3.4.2 Comparison of shear and strain variance . . . 64
3.4.3 ADCP noise . . . 69
3.4.4 Inferred dissipation patterns . . . 74
3.4.5 Comparison with previously published estimates . . . 75
3.5 Discussion . . . 81
3.6 Summary and conclusion . . . 83

4 Reconciliation of scales **85**
4.1 Introduction . . . 85
4.2 Null hypothesis . . . 87
4.3 Exploratory statistics . . . 87
4.3.1 Ensemble statistics . . . 87
4.3.2 Isopycnal statistics . . . 89
4.3.3 Mixing hotspots . . . 90
4.3.4 Temporal variability . . . 93
4.4 Sampling biases . . . 93
4.4.1 Latitude . . . 93
4.4.2 Bottom roughness . . . 98
4.4.3 Internal tides . . . 100
4.5 Hypothesis testing . . . 102
4.5.1 Perfect data assumption . . . 102
4.5.2 Lognormal assumption . . . 103
4.5.3 Parametric bias . . . 108
4.6 Discussion . . . 110
4.7 Summary and conclusion . . . 111

II Numerical simulations **113**

5 Wave mean flow interaction **114**
5.1 Introduction . . . 114
5.2 Conceptual model . . . 117

5.3 Numerical model . . . 121
5.3.1 Model equations . . . 121
5.3.2 Numerical viscosity . . . 122
5.4 Initial conditions . . . 125
5.4.1 Linear plane waves . . . 125
5.4.2 Boundary conditions . . . 126
5.4.3 GM76 wave amplitudes . . . 127
5.4.4 Ambient shear flow . . . 130
5.5 Diagnostics . . . 132
5.5.1 Energetics . . . 132
5.5.2 Hyperdissipation . . . 132
5.6 Numerical experiments . . . 133
5.6.1 Mean flow stability . . . 133
5.6.2 Single wave . . . 135
5.6.3 Two waves . . . 141
5.6.4 The broadband wave field . . . 147
5.6.5 Dissipation versus mean flow shear . . . 149
5.6.6 Dissipation versus mean flow strength . . . 155
5.6.7 Sensitivity to the number of initial modes . . . 157
5.6.8 Sensitivity to the choice of viscosity parameters . . . 162
5.7 Discussion . . . 164
5.8 Summary and conclusion . . . 167

6 Conclusion 168

Appendices 170

A Density resolution advection–diffusion model 171

B Bottom roughness 173

C Bootstrap resampling 175

List of Figures

1.1 Schematic of global overturning circulation. Color indicates approximate density ranges. Red: upper, $\gamma < 27.0$; yellow: intermediate, $\gamma \approx 27.0 - 27.6$; green: deep, $\gamma \approx 27.6 - 28.15$; blue: bottom, $\gamma > 28.15$. Gray surface with dashed edges is $\gamma = 27.6$ at 32S, separating upper and lower cell transformation in the Southern Ocean [...]. Dashed arrows indicate Indian-to-Atlantic westward exchange between Africa and the ACC. Shallow subtropical cells not included. Format adapted from Schmitz (1996). This figure and the figure caption are reproduced from [Lumpkin and Speer, 2007] p.2556.] 2

1.2 Salinity as measured during the 2002 occupation of the 32°S Indian Ocean section. [McDonagh et al., 2008] find that Indian Ocean MOC consists of a northward inflow of Lower Bottom Water (LBW), with neutral density $\gamma > 28.23$, Upper Bottom Water (UBW), with $28.11 < \gamma \leq 28.23$, and Lower Deep Water (LDW), with $27.96 < \gamma \leq 28.11$, and a southward retro-flow of Upper Deep Water (UDW), with $27.70 < \gamma \leq 27.96$. The northward flowing water masses consist of modified Antarctic Bottom Water (AABW), Circumpolar Deep Water (CDW), modified North Atlantic Deep Water (NADW), and the southward upper limb of the overturning is often referred to as Indian Deep Water (IDW). This figure is reproduced from [McDonagh et al., 2008] p.23. . . . 5

2.1 This schematic of a simple two-layer system illustrates the effect of mass advection and mass diffusion. a) initial state; b) advective transport T into the bottom layer raises the layer interface; c) diffusive mass transport F due to turbulent mixing moves the interface downward and restores the initial state. 12

2.2 Schematic of the mass fluxes into the Indian Ocean. The transport across 32°S is given by hydrography and is volumetrically balanced by the Indonesian Troughflow (ITF). The advection of Red Sea water and Persian Gulf water is restricted to the upper density layers and effectively entrains mass into these layers, as indicated by the horizontal mass diffusion F'. The vertical mass diffusion, $F_{i,i+1}$, is solved for by assuming a balance between mass advection and diffusion. Finally, the total mass budget is closed by the exchange of mass with the atmosphere, as symbolized by the net precipitation Q. 12

2.3 Schematic of the fractional assignment of transport to an inner ocean density layer. Note that some layers require special attention, for example at the surface or bottom and if the layer is very thin ($p(\rho_2) - p(\rho_1) < dp$). 14

2.4 Indian Ocean map with main basins and topography. The depth contour is at 4000m and B.=Basin; DFZ=Diamantina Fracture Zone; FZ=Fracture Zone; ITF=Indonesian Throughflow; P.=Plateau; R.=Ridge; SEIR=Southeast Indian Ridge; SWIR=Southwest Indian Ridge. 17

2.5 Hydrographic stations during the 1987 and 2002 occupation of the 32°S section. The depth contour is at 4000m. 18

2.6 Temperature at 32S as measured in 1987 and 2002. The temperature anomaly is the temperature at 2002 stations minus the temperature at the nearest 1987 stations. Note that the measurements were taken in different seasons: 12 NOV – 17 DEC 1987 and 1 MAR – 15 APR 2002. 20

2.7 Vertical cross-section at 32°S with Sandwell and Smith bathymetry (v8.2) and the neutral density layers used in our advection–diffusion model. 34

2.8 The overturning streamfunction (OSF) for various solutions for the transport across 32°S (Table 2.1). Left: the OSF calculated in depth coordinates. Right: the OSF calculated in density coordinates. The density coordinates in the right panel are transformed to depth by calculating the mean isopycnal depth using the Hydrobase climatology in a central Indian Ocean area with $\mathbf{lat} = [-41 : 1 : -21]^\circ$ and $\mathbf{lon} = [60 : 1 : 80]^\circ$. 36

2.9 Comparison of overturning streamfunctions (OSFs) based on transport across 32°S without ITF (dashed line) and with ITF (solid line). The OSF is calculated in density space and the ITF strength is chosen to balance the transport across 32°S (refer to Section 2.3.3). The depth labels are based on the interpolated depth of the density layers at the deepest station of the section. Positive transport is northward and the label 'OC' means 'outcropping' and indicates that isopycnals come to the ocean surface. 38

2.10 Turbulent mass transport, F, obtained from the density distribution, ρ, and the layer transport T. The overturning streamfunction ψ is the bottom-up integrated layer transport. 40

2.11 Mixing estimates inferred from a basin-wide mass balance in density layers for five different overturning solutions. Top: dissipation estimates [Wkg^{-1}] with error estimates (based on the uncertainties discussed in Section 2.4). Bottom left: Isoneutral mean buoyancy frequency based on the Hydrobase climatology. Bottom right: diffusivity estimates as calculated using the Osborn relation Osborn [1980], $K_\rho = 0.2\epsilon/N^2$. The horizontal black lines indicate neutral density levels that we use to distinguish between bottom water and deep water. . . 42

3.1 Buoyancy frequency and strain. Left: Comparison of the mean buoyancy frequency from a 2nd order fit $\langle N^2 \rangle_{simple}$ and from adiabatic levelling $\langle N^2 \rangle_{adia}$. The buoyancy frequency is calculated by first differencing of 2m density bins. Right: Comparison of strain variance calculated using $\langle N^2 \rangle_{simple}$ and $\langle N^2 \rangle_{adia}$. 59

3.2 Locations of hydrographic stations used for the estimation of turbulent dissipation. Open circles/diamonds indicate depth profiles with CTD and LADCP data and the plus signs mark the locations of CTD only measurements. 62

3.3 Median level of shear (red) and strain (blue) variance at given density. Dotted spectra indicate the GM spectral levels. Vertical lines correspond to wavelengths of 320, 150 and 10m (from left to right). The number between brackets is the number of spectral estimates at the given density level. 65

3.4 Quantile–quantile plots of the logarithm of the shear spectral level versus the logarithm of the strain spectral level at different density levels. Both the shear and the strain spectra are normalized by their respective GM spectral values. The red dashed line joins the first and third quartiles of each distribution. 67

3.5 Scatter plots of the logarithm of shear-and-strain dissipation estimates (horizontal axis) versus the logarithm of strain only dissipation estimates (vertical axis). The red lines indicate the range of factor three difference. 68
3.6 Shear-to-strain ratio versus GM-normalized shear variance. Note that we have excluded $R \leq 1.01$ and $R = 7$ from the ensemble and that $< R >$ denotes the median value. 70
3.7 Shear-to-strain dependence, $h_1(R)$ (3.4) in the shear-based parameterization (3.3), and $h_2(R)$ (3.8) in strain-only parameterization. 71
3.8 Number of acoustical pings going into a LADCP bin-average for the I02 section. Left: average number of pings for each depth level. Right: number of pings (vertical axis) versus bin-averaged buoyancy frequency (horizontal axis). 72
3.9 Observed vertical shear variance at section I02 and estimated ADCP noise spectra. The blue solid line is the mean spectrum for data segments at low stratification, with $N < N_{err}$, and the blue dotted line is based on data in the depth range from 1340m to 1660m. The red lines are estimated ADCP noise levels for different number of pings. The number of pings going into a velocity estimate determines its accuracy and depends on the local abundance of acoustical scatterers. . . . 73
3.10 Dissipation estimates for zonal sections. The color scale is logarithmic. White spaces indicate missing data or noisy data. 76
3.11 Dissipation estimates for meridional sections. The color scale is logarithmic. White spaces indicate missing or noisy data. . 77
3.12 Comparison of UVic and NOCS diffusivity estimates based on the Dec 1995 to Jan 1996 WOCE occupation of the I02 hydrographic section. Top: station positions. (a) UVic estimates [Kunze et al., 2006]. (b) NOCSvI estimates [Palmer et al., 2007]. (c) New NOCSvII estimates. 79
3.13 Comparison of UVic and NOCSvI. Left: comparison of 320m segment mean buoyancy frequency. Right: comparison of dissipation estimates for the same segments. Both scatter plots compare data with a difference in position of less than one second and segments depths differ by at most 80m (the segment overlap will not be perfect as UVic segments go bottom-up and NOCSvI goes top-down). 80
3.14 Depth mean dissipation rates in 500m bins. 81

4.1 Basic statistics of all estimated values for the dissipation rate. Left: frequency histogram. Right: logarithmic density histogram. The red line is a normal distribution with fit parameters $\hat{\mu} = -9.74 \pm 0.01$ and $\hat{\sigma} = 0.77 \pm 0.01$. The range indicates 95% confidence intervals. 89
4.2 Dissipation hotspots red circles at four different density levels. The hotspots are marked with red circles and defined as locations where the fine scale dissipation rate is larger than the median of the large scale basin wide estimates. Grey circles indicate locations that do *not* satisfy this criterion. Depth contours are drawn every 750m. 92
4.3 Comparison of dissipation estimates inferred from the 1995 and 2007 occupation of I09N. Top left: station track with 500m depth contours. Top right: depth mean dissipation rate. Bottom: station mean dissipation rate. The number at the top of the grey bars indicate whether the means of $\log_{10}(\epsilon)$ are different (1 means different) at 0.05 significance. . 94
4.4 Estimated probability density P(lat) for station locations and random locations in the Indian Ocean between 45°S and 30°N. 95
4.5 Upper ocean dissipation estimates (1000m≤z<500m) versus latitude (blue dots) and averaged over 1° latitude bins (red line). The analytical dissipation rate $\epsilon_0 \times L(f, N)$ is also shown for reference (black dots). 97
4.6 Square-root of bottom roughness and hydrographic stations in red. The roughness is calculated in 0.5×0.5 degree non-overlapping grid cells (refer to App. B). 99
4.7 Scatter plot of the logarithm of the roughness parameter r versus the logarithm of the dissipation rate ϵ. The parameter ρ is the linear correlation coefficient. 99
4.8 Comparison of roughness at all Indian Ocean grid points with roughness at the location of hydrographic stations. Left panel: empirical probability density histogram. Right panel: empirical cumulative density function. 100
4.9 Energy conversion to internal tides [Wm^{-2}] for one third degree grid cells and with a logarithmic colour scale (courtesy J. Nycander). Red circles indicate hydrographic stations. . . 101
4.10 Empirical probability density histogram of the energy flux to internal tides at all Indian Ocean grid cells and at station locations (tidal conversion rates from J. Nycander). 102

4.11 Logmean of the fine scale dissipation estimates (red) and the largescale dissipation estimates for the various overturning solutions considered in this study. The Garret-Munk background dissipation rate ϵ_0 is plotted for reference. Refer to Table 4.1 for the layer densities and to Table 2.1 for the meaning of the large scale abbreviations. 106
4.12 Quantile–quantile plot of the logarithm of the ensemble of all dissipation estimates versus the standard normal distribution. Q1 and Q3 are the first and third quartile value of $\log_{10}(\epsilon)$. . 108
4.13 Ratio of the mean of $\log_{10}(\epsilon)$ and mean of the interquartile range at a given density layer. Note that we only display layers with a density larger than 27.00. 109

5.1 Location and bathymetry of Atlantis II Fracture Zone (AFZ). Left: map of the South-west Indian Ocean with a red square around the area of the AFZ and 1000m depth contours. Right: multi-beam bathymetry of the AFZ. 115
5.2 Magnitude of the hyperviscosity term in the non-dimensionalized Fourier transformed equations of motion, with characteristic units $L_z = 4000$m and $U_0 = 0.1\text{ms}^{-1}$, and hyperviscosity order $p = 10$, and various values for T_{diss}. For reference are also plotted the Newtonian viscosity, $\nu U_0^{-1} L_z^{-1} k^2$ (with $\nu = 10^{-6}$ m^2 s^{-1}), and the inverse Rossby number, $Ro^{-1} = f L_z U_0^{-1}$. . 124
5.3 Comparison of hyperdissipation (5.33) and the loss rate of total energy dE/dt (refer to (5.31) and (5.32)). The simulation is initialized with a broadband GM-like wave field without a mean flow. 133
5.4 Horizontally averaged dissipation profiles for three different mean flows *without* internal waves. The maximum flow speed is 0.5 ms^{-1} for all three cases, but the shear differs, and therefore also the bulk Richardson number $Ri = N^2/U_z^2 \approx d^2 N^2/U_0^2$. The straight blue line is a reference showing the GM dissipation level for free waves. 134
5.5 Time evolution of a single wave packet without a mean flow. The wave is initialized with modes $[ik, im] = [2, 8]$, displacement amplitude $\xi = 10$m. Top row: four snapshots of the vertical velocity with a variable colour scale in mms^{-1}. Bottom row: vertical velocity spectrum. The time interval between each snapshot is 4 hours. 137

5.6 Time evolution of a single wave packet with a mean flow and a critical layer. The wave is initialized with modes $[ik, im] = [2, 8]$, with displacement amplitude $\xi = 10$m and the mean flow parameters are $U_0 = 0.8\text{ms}^{-1}$, and $d = 400$m. Top row: four snapshots of the vertical velocity with a variable colour scale in mms^{-1}. Bottom row: vertical velocity spectrum. The time interval between each snapshot is 4 hours. The white line indicates the critical level for the initial wave (refer to Table 5.1). 138

5.7 Vertical profiles of velocity and dissipation for the single wave simulation. Left panel: mean shear flow (thick) and wave velocity (thin) at t=0. Right panel: dissipation spatially averaged in the x-direction and temporally averaged over 11 hours (thick), and the 'half maximum' value as defined in Section 5.6.2 (dotted). The wave amplitude is 20 m and the shear parameters are $U_0 = 0.8$ m s^{-1} $d = 600$ m. 139

5.8 Exploration of the single wave parameter space. Dissipation rates are averaged over the entire spatial domain and in time between 5.6 and 12.5 hr. Left: dissipation/energy scaling ($E \propto \xi^2$), with mean flow parameters: $U_0 = 0.8\text{ms}^{-1}$, and $d = 600$m. Middle: dissipation versus mean flow shear, with $\xi = 20$m, and $U_0 = 0.8$ m s^{-1}. Right: width of dissipation peak versus mean flow shear, with $\xi = 20$m, and $U_0 = 0.8\text{ms}^{-1}$. 140

5.9 Time evolution of wave packet with two critical waves, $[ik_1, im_1] = [2, 16]$ and $[ik_2, im_2] = [3, 24]$. Top row: four snapshots of the vertical velocity with a variable colour scale in mms^{-1}. Bottom row: vertical velocity spectrum. The white lines indicate the critical level for each of the waves (lower level corresponds to wave 1). All waves have equal displacement amplitudes, $\xi = 40$ m, and the mean flow parameters are, $U_0 = 0.7$ ms^{-1}, and $d = 600$ m. 143

5.10 Time evolution of wave packet with one critical and one turning wave, $[ik_1, im_1] = [2, 16]$ and $[ik_2, im_2] = [-3, 24]$. Top row: four snapshots of the vertical velocity with a variable colour scale in mms^{-1}. Bottom row: vertical velocity spectrum. The white line indicates the critical level for each of the waves and the black line indicates the turning level. All waves have equal displacement amplitudes, $\xi = 40$ m, and the mean flow parameters are, $U_0 = 0.7$ ms^{-1}, and $d = 600$ m. 145

5.11 Horizontally averaged dissipation profile versus time for two waves: one critical and one turning. Top left: critical wave. Top right: turning wave. Bottom left: critical and turning wave together. Bottom right: dissipation anomaly, i.e. the difference between two waves together and the sum of single waves, $\delta\epsilon = \epsilon(k_1 + k_2) - (\epsilon(k_1) + \epsilon(k_2))$ (refer to Table 5.1 for the used wave numbers). The white line indicates the critical level and the black line the turning point. 146
5.12 Horizontally averaged dissipation profile versus time for two critical waves. Bottom left: two critical waves. Bottom right: dissipation anomaly, $\delta\epsilon = \epsilon(k_1 + k_2) - (\epsilon(k_1) + \epsilon(k_2))$, refer to Table 5.1 for the used wave numbers. The white lines indicate the critical levels. 147
5.13 Modal spectrum. Left: initial state. Right: spectrum after 1 day evolution. 148
5.14 Broadband initial state with all combinations of the 30 lowest horizontal and vertical modes. Left: frequency spectrum. Right: frequencies per horizontal mode. 149
5.15 Velocity and shear spectrum as calculated from the initial velocity field and after 1 and 10 days of free evolution (no mean flow). The dashed red line indicates the GM76 spectral level. 150
5.16 Weakly sheared mean flow with $d = 1000$m and a GM-like wavefield. Top left: initial wave field. Top right: mean flow. Middle: horizontally averaged dissipation rate of waves plus mean flow normalized by dissipation rate of waves only. Bottom: dissipation rate averaged in horizontal direction and between $z = 1000$m and $z = 2000$m for waves only and waves plus mean flow (labeled as 'mean flow'). 151
5.17 Strongly sheared mean flow $d = 200$m and a GM-like wavefield. Top left: initial wave field. Top right: mean flow. Middle: horizontally averaged dissipation rate of waves plus mean flow normalized by dissipation rate of waves only. Bottom: dissipation rate averaged in horizontal direction and between $z = 1000$m and $z = 2000$m for waves only and waves plus mean flow (labeled as 'mean flow'). 152
5.18 Dissipation versus mean flow shear, U_0/d, with $U_0 = 0.5$ ms^{-1}. The dissipation rate is spatially averaged along the horizontal dimension and between $z = 1000$ and $z = 2000$m in the vertical and temporally between day 9 and 10. 153

5.19 Dissipation rate based on a simple model (solid lines) compared to full simulations (dotted lines). The model treats all wave modes as non-interacting except at the critical layer where they transform to smaller scales at a rate, $dm/dt = kU_0/d$, until they dissipate close to the given Nyquist wave number. 156
5.20 Dissipation versus mean flow strength. Top: $U_0 = 0.05$ ms^{-1}. Middle: $U_0 = 0.25$ ms^{-1}. Bottom: $U_0 = 0.5$ ms^{-1}. The shear is the same and has a value of 0.001 s^{-1}. 158
5.21 Dissipation versus mean flow strength with constant vertical shear, $U_0/d = 0.001$ s^{-1}. The dissipation rate is averaged along the horizontal direction and vertically between $z = 1000$ m and $z = 2000$ m and temporally between day 9 and 10. . . 159
5.22 Lowest critical wave numbers for a given mean flow amplitude. The grey shaded area indicates the wave numbers for which the numerical viscosity is smaller than the molecular viscosity of water. 160
5.23 Time evolution of the spatially averaged dissipation rate for a different number of initial modes. There is no mean flow in this simulation. 161
5.24 Spatially averaged dissipation rate for different hyperviscosity coefficients. Coefficients are chosen such that the wave number at which hyperviscosity surpasses Newtonian viscosity remains more or less the same. The coefficients used for the broadband simulations are $p = 10$ and $T_{diss} = 1000$. . . . 163

A.1 Vertical cross-section of a box-volume with hard walls on three sides and a hard bottom. Advective transport is allowed through the open left-hand-side. Note that T is transport per unit depth. 171

List of Tables

2.1 Estimated overturning strength (i.e. maximum bottom-up integrated transport) and overturning depth (i.e. the depth of the maximum) from various studies. The three letter abbreviations indicate the solutions used in this study. 21
2.2 Indonesian Throughflow from various studies. The transport is westward, from the Pacific to the Indian Ocean. 24
2.3 The Indonesian Throughflow (ITF) in density classes from [Koch-Larrouy et al., 2006]. Mass input from Red Sea (RS) and Persian Gulf (PG) is uniformly distributed over layers lighter than 28.11 kg m^{-3}. Note that in our calculations we normalise the ITF to the transport across 32°S. 25
2.4 Red Sea and Persian Gulf data. The dilution factor is based on the 1D streamtube entrainment model by [Price and Baringer, 1994] and calculated by [Bower et al., 2000]. 26
2.5 Estimates of the total dissipated power, P, needed to sustain the deep Indian Ocean MOC. Also shown are, the overturning maximum Ψ_{max}, the depth of the overturning maximum z_{max}, the closing density γ_0, and the approximate depth of the closing density, z_0. The power is calculated by integrating the dissipation rate from the bottom up to the closing density. The closing density corresponds to the zero-crossing of the overturning streamfunction and represents the density level where the the inflow of dense bottom and deep water is balanced by the more shallow and less dense retro-flow. We attribute the difference between the overturning maxima, Ψ_{max}, and the published maxima in Table 2.1 to the fact that we calculated the overturning maximum in density space as opposed to depth space. 43
2.6 Diffusivity estimates in the Indian Ocean. 45
2.7 Energy input to the deep Indian Ocean north of 32°S. 46

3.1 Model configuration 60

3.2 Hydrographic sections used for estimation of turbulent dissipation. The LADCP bin size is given in the Δz column and the asterisk means that both up– and mean cast data are available. All sections prior to 1998 are part of the World Ocean Circulation Experiment (WOCE) and later sections fall under the Climate Variability and Predictability (CLIVAR) program, except for the ACSEX series, which was organised and funded by the Netherlands Institute for Sea Research (NIOZ). The data sets I, II and III contain additional CTD-only profiles from NIOZ, Systèmes d'Informations Scientifiques pour la Mer (SISMER), and the United States National Oceanographic Data Center (NODC). 63

4.1 Statistics of the dissipation rate interpolated onto neutral density levels. 91
4.2 Latitudinal bias estimates. The mean dissipation rate $\langle\epsilon\rangle$ is based on (3.5). 96
4.3 Bootstrap estimates of the mean dissipation rate and the standard deviation with $B = 1000$ for the number of bootstrap replicates (refer to App. C). The logical in the last five columns indicates whether the null hypothesis is rejected (1 means rejection). 104
4.4 T-test of the hypothesis that the logged fine scale dissipation estimates come from a distribution with a mean given by the large scale expected value minus the variance of the logged fine scale estimates. Outcome '1' means that null hypothesis (4.1) is rejected under the assumption of lognormality at a 0.05 significance level. 107

5.1 Model parameters for single wave (I) and two wave (II) simulations. 135

DECLARATION OF AUTHORSHIP

I, `Tycho Nout Huussen` , declare that the thesis entitled:
`Is the Indian Ocean MOC driven by internal wave breaking?`
and the work presented in the thesis are both my own, and have been generated by me as the result of my own original research.

I confirm that:

- this work was done wholly or mainly while in candidature for a research degree at this University;
- where any part of this thesis has previously been submitted for a degree or any other qualification at this University or any other institution, this has been clearly stated;
- where I have consulted the published work of others, this is always clearly attributed;
- where I have quoted from the work of others, the source is always given. With the exception of such quotations, this thesis is entirely my own work;
- I have acknowledged all main sources of help;
- where the thesis is based on work done by myself jointly with others, I have made clear exactly what was done by others and what I have contributed myself;
- none of this work has been published before submission.

Signed: .....

Date: .....

Abbreviations

ADCP	Acoustic Doppler Current Profiler
AFZ	Atlantis II Fracture Zone
BRY	Bryden and Beal (2001)
CIR	Central Indian Ridge
CSIRO	Commonwealth Scientific and Industrial Research Organisation
CTD	Conductivity, Temperature, and Depth
FER	Ferron and Marotzke (2003)
FS	Fine scale
FWHM	Full Width at Half Maximum
FZ	Fracture Zone
G89	Gregg 1989 (first fine scale parameterization)
GAN	Ganachaud and Wunsch (2000)
GCM	General Circulation Model
GM	Garret-Munk (internal wave model)
ITF	Indonesian Throughflow
LADCP	Lowered Acoustic Doppler Current Profiler
LS	Large scale
MCD	McDonagh et al. (2008)
MIT	Massachusetts Institute of Technology (USA)
MOC	Meridional Overturning Circulation
NOCS	National Oceanography Centre, Southampton (UK)
OGCM	Ocean General Circulation Model
OSF	Overturning streamfunction
PG	Persian Gulf
RS	Red Sea
RSW	Red Sea Water
Sv	Sverdrup transport unit ($1\text{Sv}=1\times10^6\ \text{m}^3\text{s}^{-1}$)
SLO	Sloyan and Rintoul (2001)
SWIR	Southwest Indian Ridge
TKE	Turbulent kinetic energy
UVic	University of Victoria (Canada)
WHOI	Woods Hole Oceanographic Institution
WOCE	World Ocean Circulation Experiment

Acknowledgements

First and foremost I want to thank my supervisor at the National Oceanography Centre, Southampton, Alberto Naveira-Garabato. Alberto is a very active scientist in the forefront of oceanography and at the same time an excellent people manager. I have always appreciated his patience and support and the fact that he knew when to coach me and when to let me go. The chair of my advisory panel, David Smeed, has stimulated me with his encouraging feedback at our biannual panel meetings. The other two advisers on my panel, Elaine McDonagh and Harry Bryden, have offered me the luxury of viewing matters from a different angle. Elaine has been particularly helpful when I was getting started with the data and she has taught me the basics of hydrographic inverse modeling. Harry's original viewpoints have always been stimulating and he has helped me to keep focussed on the main picture. I am also indebted to the World University Network for awarding me a grant within International Research Mobility Scheme. This grant gave me the opportunity to work with Jen MacKinnon at the Scripps Institute of Oceanography. I am grateful to Jen for offering me a research cruise opportunity and I have enjoyed working with her. Her willingness to share her understanding of internal wave dynamics and her modeling expertise have added an extra dimension to my dissertation. Finally, I want to thank Eric Kunze for patiently and courteously answering my usually rather naive questions about his implementation of the fine scale parameterization, and Kurt Polzin for sharing his insights in fine scale issues. All these people have been tremendously helpful when working on my dissertation, but without my friends in Amsterdam, Southampton, and San Diego, and my girlfriend and parents I surely would have gone insane.

Chapter 1

Introduction

The ocean circulation transports seawater properties over the globe (see Fig. 1.1). Some of these properties, such as heat and dissolved greenhouse gasses, have climatological impact, others, like nutrients and pollutants, affect living organisms. The global meridional overturning circulation (MOC) consists of both horizontal and vertical motion and is sometimes referred to as the 'great ocean conveyor' [Broecker, 1991]. Vertical movement in the ocean is supported by a delicate balance between deep convective downwelling at a few sites in the North Atlantic and Southern Ocean and upwelling throughout the ocean interior.

The Earth's gravity field has an ordering effect on the ocean, making it density stratified, with lighter water above heavier water. This implies that a vertically moving parcel of seawater must change density, if we are to maintain the stably stratified mean state of the ocean. The only way to do so is by mass exchange with the ambient fluid, or the atmosphere in the case of downwelling at the surface. However, mass exchange through molecular diffusion in laminar flow is too slow to produce sufficient upwelling to close the MOC. We need turbulence. The process of fluid intertwinement by turbulent eddies and subsequent homogenisation by

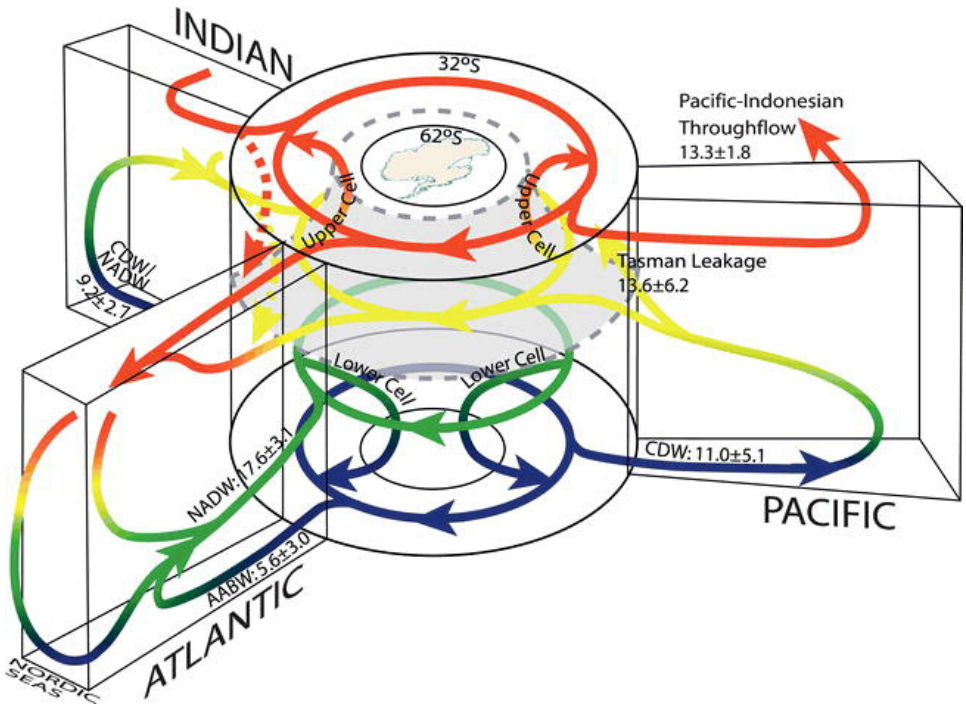

Figure 1.1: Schematic of global overturning circulation. Color indicates approximate density ranges. Red: upper, $\gamma < 27.0$; yellow: intermediate, $\gamma \approx 27.0-27.6$; green: deep, $\gamma \approx 27.6-28.15$; blue: bottom, $\gamma > 28.15$. Gray surface with dashed edges is $\gamma = 27.6$ at 32S, separating upper and lower cell transformation in the Southern Ocean [...]. Dashed arrows indicate Indian-to-Atlantic westward exchange between Africa and the ACC. Shallow subtropical cells not included. Format adapted from Schmitz (1996). This figure and the figure caption are reproduced from [Lumpkin and Speer, 2007] p.2556.]

molecular diffusion is referred to as 'ocean mixing'.

How much vertical mixing is needed to sustain the global MOC depends on its structure and strength. If all the deep water produced at high latitudes upwells in the ocean interior one would need a global abyssal dissipation rate of about 2.1 TW (assuming 20% 'mixing efficiency') [Munk, 1966; Munk and Wunsch, 1998; Wunsch and Ferrari, 2004]. The estimated input of energy is also ∼2.1 TW [Wunsch and Ferrari, 2004; Ferrari and Wunsch, 2009], just enough to sustain the global MOC if there are no losses to processes that do not mix the ocean at 20% efficiency.

More recent insights in the structure of the global MOC alleviate the need for turbulent kinetic energy (TKE) in the ocean interior. A computer model study by [Toggweiler and Samuels, 1998] produces a global overturning sustained by wind driven mixing in the Antarctic Cicumpolar Current (ACC), without vertical mixing in the ocean interior. However, [Wunsch and Ferrari, 2004] point out that the deepest isopycnals in the ocean never outcrop or shoal to within reach of the ACC. These insights give rise to a two cell picture of the global MOC: a deep lower cell driven by abyssal vertical mixing and a more shallow upper cell driven primarily by mixing in the ACC [Webb and Suginohara, 2001].

The Indian Ocean is generally considered to host a large limb of the global deep overturning cell, as depicted in Fig. 1.1. Most of the more recent hydrography based studies find that about half of the global deep upwelling takes place in the Indian Ocean. For example, [Ganachaud and Wunsch, 2000] have estimated worldwide upwelling across the 28.11 kg m^{-3} neutral density[1] surface for all oceans (except the Arc-

[1]Neutral density is a global density variable that minimizes the work needed to move a water parcel along any isoneutral trajectory [Jackett and McDougall, 1997]. Note that

tic Ocean). They find an upwelling rate of 11±5 Sv (1Sv≡ 1×10^6 m^3s^{-1}) in the Indian Ocean, approximately equal to the estimated deep upwelling in the Atlantic Ocean, and about twice bigger than in the Pacific Ocean. This is especially remarkable when we realize that the Indian Ocean is the smallest of all oceans, covering less than 20% of the world ocean.

All hydrography based estimates of Indian Ocean MOC are primarily based on 32°S hydrographic section between South-Africa and Australia. Figure 1.2 shows salinity as measured during the most recent occupation of this section in 2002 and the water masses as identified by [McDonagh et al., 2008]. An inverse model study by [McDonagh et al., 2008], based on the data collected in 2002, also finds a strong overturning cell in the Indian Ocean, similar in strength to previous solutions for the Indian Ocean overturning, but with a deeper return flow. The deep Indian Ocean overturning cell found by [McDonagh et al., 2008] consists of northward flowing bottom and deep water, occupied by modified Antarctic Bottom Water (AABW), Circumpolar Deep Water (CDW), and modified North Atlantic Deep Water (NADW), balanced by a deep southward flow, below 1500m, occupied by Indian Deep Water (IDW), that is fed back into the ACC, where it blends into the upper CDW water mass. The IDW, produced by the Indian Ocean MOC, is oxygen depleted, but rich in nutrients and carbon [Drijfhout and Garabato, 2008], suggesting both a long residence time of the water masses and isolation from the surface. Isolation from the surface means that the water mass transformation in the Indian Ocean MOC must be driven exclusively by abyssal mixing processes. In this thesis we will assess whether one of

all densities in this dissertation are given as a density anomaly with respect to 1000 kg m^{-3}.

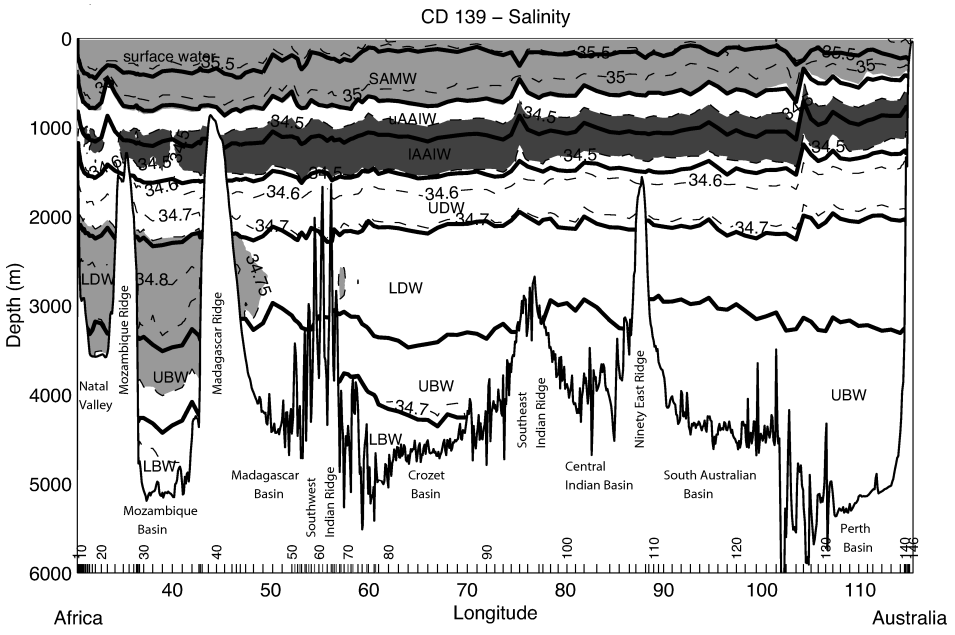

Figure 1.2: Salinity as measured during the 2002 occupation of the 32°S Indian Ocean section. [McDonagh et al., 2008] find that Indian Ocean MOC consists of a northward inflow of Lower Bottom Water (LBW), with neutral density $\gamma > 28.23$, Upper Bottom Water (UBW), with $28.11 < \gamma \leq 28.23$, and Lower Deep Water (LDW), with $27.96 < \gamma \leq 28.11$, and a southward retro-flow of Upper Deep Water (UDW), with $27.70 < \gamma \leq 27.96$. The northward flowing water masses consist of modified Antarctic Bottom Water (AABW), Circumpolar Deep Water (CDW), modified North Atlantic Deep Water (NADW), and the southward upper limb of the overturning is often referred to as Indian Deep Water (IDW). This figure is reproduced from [McDonagh et al., 2008] p.23.

the abyssal mixing processes most favoured in literature, that is internal wave breaking, can account for the mixing needed to sustain the Indian Ocean MOC.

The question whether the Indian Ocean contains enough TKE to balance the high upwelling rates inferred from hydrographic inverse models has motivated this study. In Chapter 2 we estimate the turbulent dissipation needed to sustain the Indian Ocean overturning circulation by assuming a balance between advection and diffusion. Chapter 3 discusses a fine scale parameterization to infer internal wave dissipation from

fine scale shear and strain and presents internal wave dissipation estimates for the Indian Ocean WOCE[2] sections and other hydrographic stations. Chapter 4 compares the large scale, inverse model dissipation estimates with turbulent dissipation estimates inferred from fine scale, internal wave observations. In the final chapter we look at the dissipation of a broad band internal wave field due to critical layer interactions in a sheared mean flow, using idealized numerical simulations. This problem is distantly related to the mixing needed to sustain the Indian Ocean MOC, but will be treated separately.

[2]World Ocean Circulation Experiment.

Part I

MOC energetics

Chapter 2

Box-model mass budget: one-dimensional constraints on the energetics of mixing in the Indian Ocean

2.1 Introduction

In this chapter we consider the energetics of five recent inverse model solutions for the Indian Ocean overturning circulation. Four solutions are based on hydrographic measurements along the 32°S transect [McDonagh et al., 2008; Bryden and Beal, 2001; Sloyan and Rintoul, 2001; Ganachaud and Wunsch, 2000] and one solution is based on a general circulation model assimilating hydrographic data [Ferron and Marotzke, 2003].

We calculate the diapycnal mass transport by assuming a balance between mass diffusion and advec-

tion in density layers. The advective mass transport into the density layers of our Indian Ocean box-model comprises transport across the open boundary at 32°S and the Indonesian Throughflow (ITF). In our model we also account for the high density outflow plumes from the Red Sea (RS) and the Persian Gulf (PG).

We calculate the turbulent dissipation by assuming that the diapycnal mass flux is the result of turbulent diffusion. Writing the turbulent eddy diffusivity in terms of dissipation using the Osborn relation [Osborn, 1980] gives a simple relation between the turbulent mass flux and the dissipation rate, involving quasi-constants like the gravitational acceleration, the 'mixing efficiency', and the mean density.

In the Section 2.6 we compare the dissipation rates needed to sustain the overturning solutions considered in this study with estimates of available dissipation. This comparison shows that the Indian Ocean consumes a large chunk of the globally available energy. This is consistent with the picture that the Indian Ocean hosts an important deep upwelling limb of the global MOC, but also raises questions about the realism of the various circulation schemes. In Chapter 4 we compare the energy demand of the Indian Ocean MOC with the energy supply by what is commonly thought to be the major source of turbulence in the interior ocean: internal waves.

2.2 Methods

2.2.1 Advection–diffusion balance

The stratification of the ocean is preserved if the advective divergence of its properties is balanced. Diffusion is the only available mechanism to balance advection in an ocean volume without sources and sinks for

tracers,

$$\nabla \cdot (\mathbf{U}\phi) = -\nabla \cdot (K\nabla\phi), \tag{2.1}$$

where K is (eddy) diffusivity, ϕ is the tracer concentration, and $\mathbf{U} = (u, v, w)$ the three dimensional flow field. This balance is expected to hold for the interior of the ocean, away from boundaries and biological activity. Assuming that (i) the tracer concentration only has a vertical gradient, (ii) diffusivity K is laterally constant, and (iii) $u, v >> w$ so that $u_x + v_y \cong 0$, gives, $w\phi = -K\phi_z$. [Munk, 1966] used this equation and observed profiles of temperature and carbon 14 to estimate the global upwelling velocity, $w = 0.00014$ mms^{-1}, and diffusivity $K = 1.3$ cm^{2}s^{-1}.

The balance between advective and diffusive divergence given by (2.1) can be written in terms of fluxes through the sides of a box-volume by (i) integrating over volume, (ii) applying the divergence theorem to the left hand side (lhs), (iii) vertical integration of the right hand side (rhs). These manipulations and writing ρ for the 'mass concentration' or density give,

$$\int U\rho \cdot dA = [\overline{K\rho_z}A]_{top} - [\overline{K\rho_z}A]_{bottom}, \tag{2.2}$$

where A is the surface area of the volume and $\overline{K\rho_z}$ the area averaged product of the diffusivity and the density gradient at the top and bottom of the box volume [Sloyan, 2006]. This mass balance holds to good approximation for any box volume in a steady, vertically density stratified ocean with negligible horizontal diffusion.

The integral on the lhs of (2.2) can be simplified for a box volume enclosed by density layers. For layer i, between density interface $\rho_{i-1,i}$ and $\rho_{i,i+1}$, with vertical transport $T_{i-1,i}$ at the bottom interface and $T_{i,i+1}$ at the top interface, horizontal transport T_i across the side walls of the layer, and transport weighted den-

sity $\overline{\rho_i}$ at the side walls, we can write the advection–diffusion balance as,

$$\overline{\rho_i} T_i + \rho_{i-1,i} T_{i-1,i} - \rho_{i,i+1} T_{i,i+1} = F_{i-1,i} - F_{i,i+1}, \tag{2.3}$$

where transport into the layer is defined to be positive, layer numbers go bottom-up with $\rho_{i-1,i} \geq \overline{\rho_i} > \rho_{i,i+1}$, and $F \equiv \overline{K \rho_z} A$ the turbulent (diffusive) mass transport across the top and bottom interface. The terms on the lhs represent advective mass divergence and the terms on the rhs diffusive mass divergence, where the horizontal diffusion is assumed to be negligible. We assume a steady state where both layer volume and layer mass are conserved.

The role of the diffusive mass transport F in the advection–diffusion balance is illustrated in Fig. 2.1. The figure shows a two-layer system with density ρ_1 at the bottom and ρ_2 at the top (Fig. 2.1a). Lateral advection into the bottom layer would raise the interface between the layers in the absence of diapycnal mixing (Fig. 2.1b). Diapycnal diffusion erodes density gradients (Fig. 2.1c), and effectively restores the system into its initial state (Fig. 2.1d). Equations 2.1–2.3 prescribe a continuous balance between these two effects.

The advection–diffusion balance given by (2.3) can be solved for F, given the velocity or transport and the density at the lateral sides of the box, and an appropriate boundary condition at the bottom of the box. The vertical transport follows simply from continuity, $T_{i,i+1} = \sum_{j=1}^{i} T_j$. For the boundary condition we choose $F_{0,1} = T_{0,1} = 0$ at the bottom, that is zero flow or diffusion through the sea floor. Figure 2.2 gives a schematic overview of the fluxes in our Indian Ocean box-model.

The advection–diffusion balance in the form used

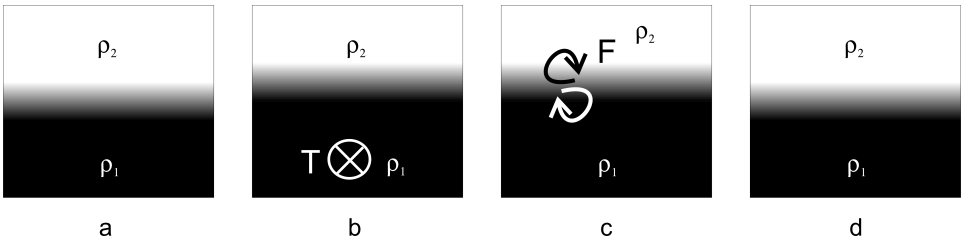

Figure 2.1: This schematic of a simple two-layer system illustrates the effect of mass advection and mass diffusion. a) initial state; b) advective transport T into the bottom layer raises the layer interface; c) diffusive mass transport F due to turbulent mixing moves the interface downward and restores the initial state.

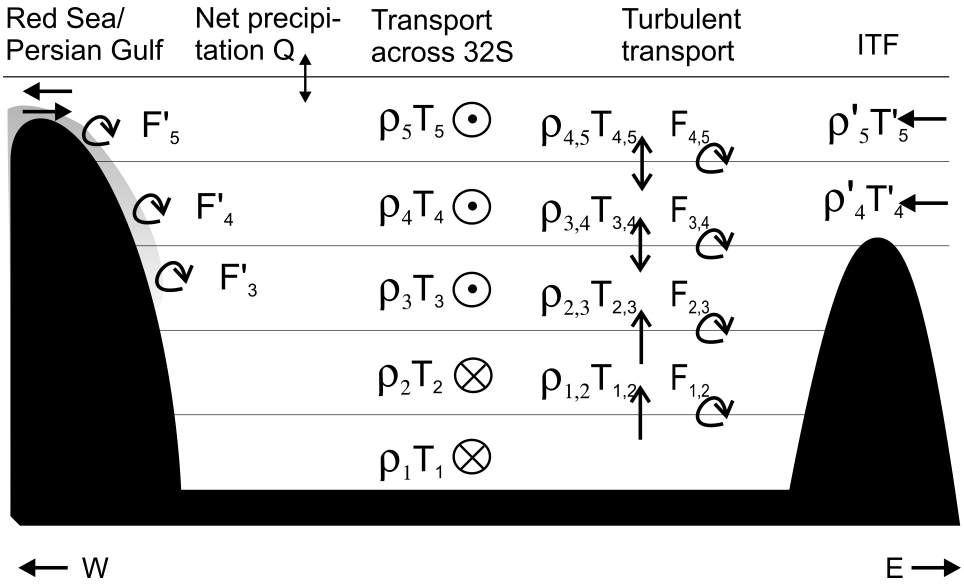

Figure 2.2: Schematic of the mass fluxes into the Indian Ocean. The transport across 32°S is given by hydrography and is volumetrically balanced by the Indonesian Troughflow (ITF). The advection of Red Sea water and Persian Gulf water is restricted to the upper density layers and effectively entrains mass into these layers, as indicated by the horizontal mass diffusion F'. The vertical mass diffusion, $F_{i,i+1}$, is solved for by assuming a balance between mass advection and diffusion. Finally, the total mass budget is closed by the exchange of mass with the atmosphere, as symbolized by the net precipitation Q.

here ignores the non-linearity of the equation of state [Munk and Wunsch, 1998]. The effect of these non-linearities on the global dissipation budget is investigated by [Klocker and McDougall, submitted 2009] and found to be significant in the Southern Ocean, mostly due to sharp temperature fronts and outcropping isopycnals. This effect however is expected to be small in the Indian Ocean.

2.2.2 Mass transport into density layers

This section discusses the binning of mass transport into density layers. The use of density, instead of pressure, as the vertical coordinate allows us to make energy estimates, as discussed in the next section.

Geostrophic flow calculated from hydrography is usually given in pressure bins, with typical dimensions of 20dbar by 10–100km, depending on the distance between the hydrographic stations. A density layer intersecting with a binned flow field will generally encompass a number of whole and fractional bins, as is schematically depicted in Fig. 2.3. The total transport into a density layer is found by integrating all whole and fractional transport bins, where the contribution from a fractional bin is assumed proportional to its area within the layer boundaries.

A layer confined by ρ_1 and ρ_2 ($\rho_2 > \rho_1$) and top pressure $p(\rho_1)$ encompasses fraction $f_n = (p(\rho_1) - p_n)/\Delta p$ of bin $n+1$ if $\rho_{n+1} < \rho_1 < \rho_n$. Suppose bin fraction at the upper layer boundary is f_n and at the lower boundary f_m, then, for some station pair $(s, s+1)$, we write the layer transport as,

$$T_{s,s+1} = f_n\, T_{n+1} + \sum_{i=n+2}^{m} T_i + f_m\, T_{m+1}, \qquad (2.4)$$

where T_i is the transport in bin i.

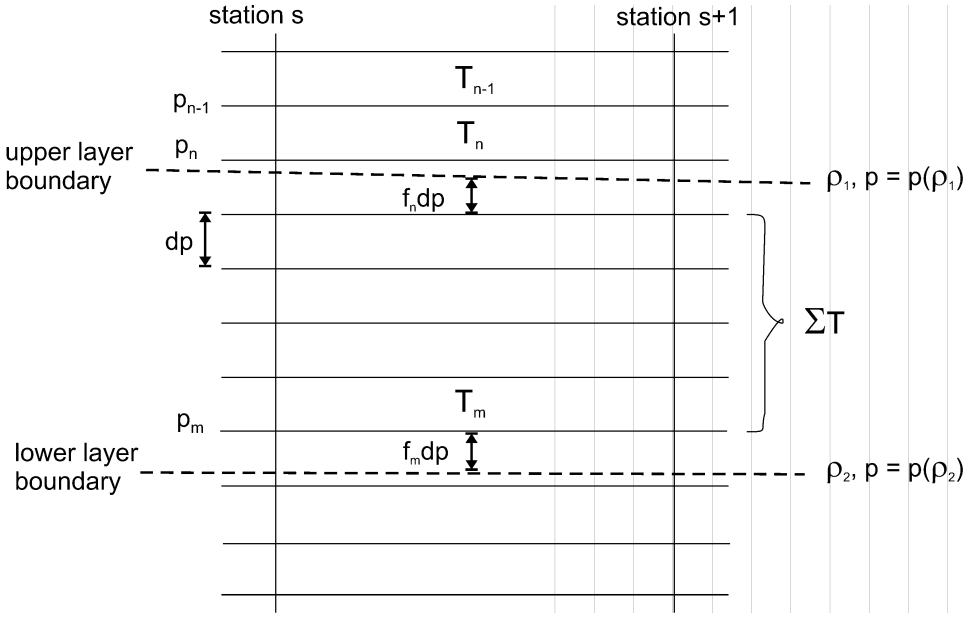

Figure 2.3: Schematic of the fractional assignment of transport to an inner ocean density layer. Note that some layers require special attention, for example at the surface or bottom and if the layer is very thin ($p(\rho_2) - p(\rho_1) < dp$).

Layers encompassing the surface or bottom require special attention as well as the case where multiple layers fit into a single transport bin. Accounting for these situations we exactly reproduce the total transport, as obtained from simple addition of all the bins. The method works for any number of arbitrarily spaced density layers under the one condition that the stratification is stable, meaning that a less dense layer *cannot* be above a more dense layer, not even locally, because the method as implemented will account twice for the transport in the unstable region. The physical reason for avoiding length scales where instabilities are resolved is that these patches of unstable water will only exist temporarily, because buoyancy driven downward mass transport will quickly restore the fluid to an energetically favourable, stably stratified state. In our analysis however, we are interested in the opposite

process: the spatial and temporal mean *upward* mass transport by mixing processes.

The stability condition is satisfied if the density layers are not too closely packed. We find instabilities in the pycnocline for 15 layers (or more) if we use a constant density spacing between layers. Choosing an exponential density spacing between layers gives a much more regular layer spacing in pressure space and allows for 200 layers or more.

The applied linear interpolation ignores the fact that density *does not* linearly depend on pressure. Consequently we slightly overestimate layer pressure, introducing an error in the layer transport. However, this error is small for small layer spacing and in regions of weak shear. A general discussion of the errors associated with methods used in this study is presented in Section 2.4.

2.2.3 Turbulent dissipation

The turbulent mass transport was defined in Section 2.2.1 as $F = \overline{K_\rho \rho_z} A$, with turbulent diffusivity K_ρ, density gradient ρ_z, surface area A, and the overline a spatial average over surface A. This relation may be written as,

$$F = \overline{K_\rho} \times \overline{\rho_z} \times A, \tag{2.5}$$

if K_ρ and ρ_z are spatially uncorrelated. Relying on the same assumption that K_ρ is random with respect to ρ_z we may write the Osborn relation [Osborn, 1980] as,

$$\overline{K_\rho} = \Gamma \frac{\overline{\epsilon}}{\overline{N^2}}, \tag{2.6}$$

with the mean buoyancy frequency defined as $\overline{N^2} = g\rho^{-1}\overline{\rho_z}$, and Γ the so-called 'mixing efficiency'. Throughout this work we will assume Γ to be constant and equal to the canonical value of 0.2, thus ignoring po-

tential variability of this parameter [Peltier and Caulfield, 2003].

Substitution of the Osborn relation (2.6) in (2.5) gives a directly proportional relation between the turbulent dissipation rate and the turbulent mass flux,

$$\frac{F}{A} = \frac{\rho}{g}\Gamma\epsilon, \tag{2.7}$$

because the mean density gradient $\overline{\rho_z}$ cancels out. The parameters density ρ and gravitational acceleration g are both quasi-constants with less than 1% variation.

The same result is obtained by equating the turbulent power available for mixing to the rate at which potential energy is generated. Potential energy is generated when heavy water is advected vertically and lifted against gravity in a density stratified fluid. For example, for a simple two-layer system, with two density layers, with ρ above ρ', $\rho < \rho'$, vertical advection w [ms^{-1}], and layer area A, the mass flux into the top layer is, $F = (\rho' - \rho)wA$ [kgs^{-1}]. The power required to lift this mass against gravity, g, over the thickness of the layer, h, is Fgh [kgm^{2}s^{-3}]. If this energy were supplied by turbulent dissipation with efficiency Γ, we would obtain, $\Gamma\epsilon\rho Ah = Fgh$, which is equivalent to (2.7).

2.3 Data

The budget method described in the previous section requires knowledge about the basin-wide mass divergence. The box model used in this study comprises the Indian Ocean north of 32°S, that is roughly north of Durban, South Africa and Fremantle, Australia (see Fig. 2.4). The rest of the basin is mostly confined by land masses, with Africa in west, the Asian continent in the north and Indonesia and Australia in the

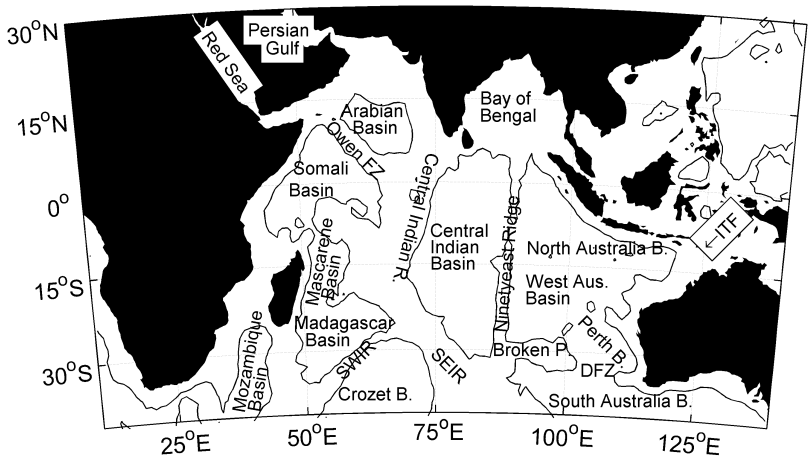

Figure 2.4: Indian Ocean map with main basins and topography. The depth contour is at 4000m and B.=Basin; DFZ=Diamantina Fracture Zone; FZ=Fracture Zone; ITF=Indonesian Throughflow; P.=Plateau; R.=Ridge; SEIR=Southeast Indian Ridge; SWIR=Southwest Indian Ridge.

east. The only other direct connection to the rest of the world ocean is the Indonesian Throughflow (ITF). In this study we account for the transport across the open southern boundary using previously published hydrographic inverse-model solutions (refer to Section 2.3.2). We assume that the volume transport across 32°S is balanced by the ITF (refer to Section 2.3.3) and that the mass budget is closed by atmospheric buoyancy exchange. We account for the production of Red Sea Water (RSW) and Persian Gulf Water (PGW) by assuming that the outflow plumes of these marginal seas effectively put mass into deeper layers up to about 1500m depth (refer to Section 2.3.4).

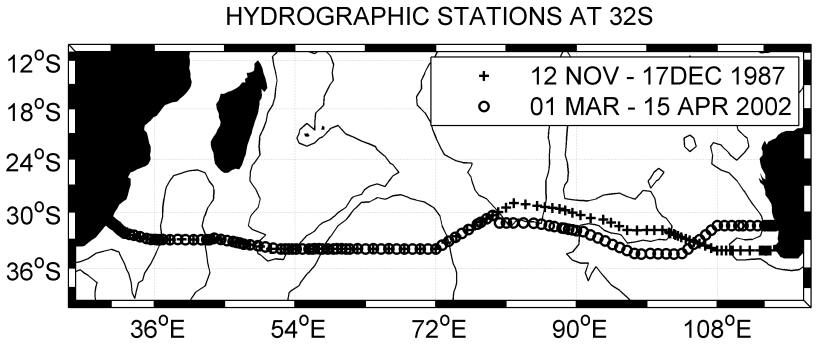

Figure 2.5: Hydrographic stations during the 1987 and 2002 occupation of the 32°S section. The depth contour is at 4000m.

2.3.1 Hydrography at 32°S

The 32°S zonal section has been sampled by hydrographic cruises in 1936, 1965[1], 1987 and 2002. The first high quality CTD[2] measurements were collected in 1987 [Toole and Warren, 1993] and most inverse solutions for the Indian Ocean MOC used in this study are based on this data set. Only the newest MCD solution [McDonagh et al., 2008] is based on the latest occupation in 2002 [Bryden, 2003].

The hydrographic cruises in 1987 and 2002 occupied approximately the same stations in the western half of the section, as shown in Fig. 2.5. The 2002 cruise avoids Broken Plateau by choosing more southern station positions and Naturaliste Plateau at the south-western tip of the Australian shelf is avoided by going more north.

The 1987 and 2002 deep temperature fields (below

[1]The occupations by the British RRS Discovery in 1936 and 1965 are both documented in the "Oceanographic Atlas of the International Indian Ocean Expedition", K. Wyrtki, 1971; The German SMS Gazelle sampled hydrographic data along 34°S during the 1874–76 expedition.

[2]CTD: conductivity, temperature and depth.

1500m) are shown in Fig. 2.6. The measurements in 2002 are taken at the end of spring and early summer, that is November and December in the southern hemisphere. The 1987 are taken in early autumn (March and April). Both temperature fields look very similar, both in magnitude and structure. However, the temperature anomaly, and especially the zonally integrated temperature anomaly, show that temperatures in 2002 are slightly higher, in particular towards the surface. This could be a seasonal effect.

2.3.2 Transport across 32°S

This study considers five published solutions for the transport across 32°S (Table 2.1). Four solutions are based on the 1987 data set and only one solution, the MCD solution, is based on the 2002 data. We selected these solutions because the other solutions have some known issues, for example: [Fu, 1986] is based on older, lower quality data, [Toole and Warren, 1993] does not conserve silica, [Robbins and Toole, 1997], and [Macdonald, 1998] do not account for the Agulhas undercurrent. Below we briefly discuss all five transport fields.

McDonagh et al. (2008)

RRS Charles Darwin (CD139) occupied 146 hydrographic stations along the 32°S section in 2002 [Bryden, 2003]. The cruise track is roughly the same as in 1987 (CD29) (see Section 2.3.1). [McDonagh et al., 2008] use data from this cruise and additional measurements in the Agulhas Current [Bryden et al., 2005], in the Leeuwin Current [Feng et al., 2003], and in the Perth Basin [Sloyan, 2006] to calculate the meridional velocity field at 32°S. The initial state is obtained by referencing the geostrophic station pair velocities us-

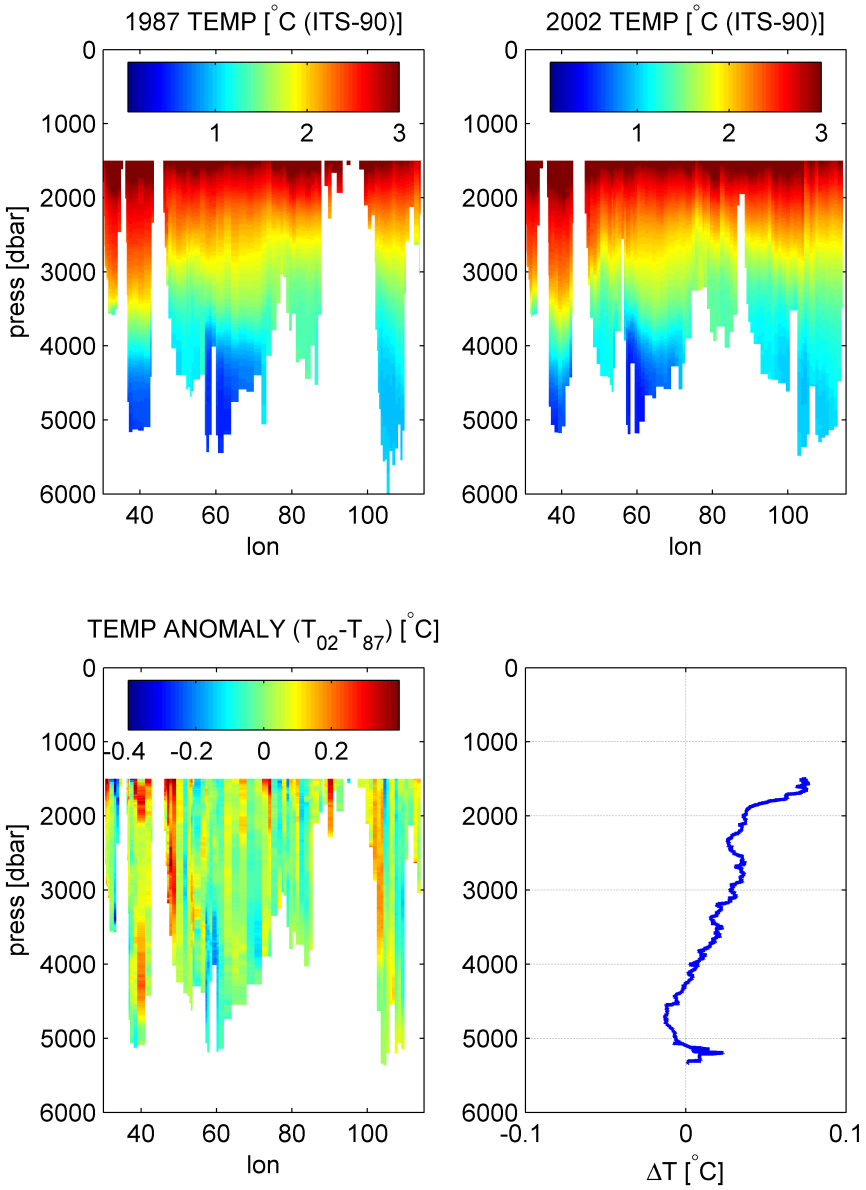

Figure 2.6: Temperature at 32S as measured in 1987 and 2002. The temperature anomaly is the temperature at 2002 stations minus the temperature at the nearest 1987 stations. Note that the measurements were taken in different seasons: 12 NOV – 17 DEC 1987 and 1 MAR – 15 APR 2002.

Hydrography		Strength (Sv)	Depth (m)
	[Toole and Warren, 1993]	27	2600
SLO	[Sloyan and Rintoul, 2001]	23 ± 3	2600
	[Macdonald, 1998]	17 ± 5	2000
	[Robbins and Toole, 1997]	12 ± 3	2600
GAN	[Ganachaud and Wunsch, 2000]	11 ± 4	2500
BRY	[Bryden and Beal, 2001]	10.1	2000
MCD	[McDonagh et al., 2008]	9.0–10.3	3310–3570
	[Fu, 1986]	3	2000
Modelling			
	[Wacongne and Pacanowski, 1996]	< 0[a]	NA
	[Lee and Marotzke, 1997]	2	2200
	[Zhang, 1999]	2	2000
	[Garternicht and Schott, 1997]	3	3700
FER	[Ferron and Marotzke, 2003]	17	3200

Table 2.1: Estimated overturning strength (i.e. maximum bottom-up integrated transport) and overturning depth (i.e. the depth of the maximum) from various studies. The three letter abbreviations indicate the solutions used in this study.

[a] no deep northward flow at 32°S.

ing ship-mounted Acoustic Doppler Current Profiler (ADCP) measurements and lowered ADCP (LADCP) measurements. Final adjustments of reference levels are based on silica conservation.

The overturning solution obtained from the new dataset is comparable in strength with previous estimates (refer to Table 2.1), but the return flow is about a kilometer deeper (refer to Section 2.5.1 for a discussion about the overturning strength and depth).

Bryden and Beal (2001)

A LADCP survey of the Agulhas current[3] in 1995 revealed a 6Sv retropropagating (i.e. northward) undercurrent [Beal and Bryden, 1997]. [Bryden and Beal,

[3]The Agulhas Current [...] is the Western Boundary Current of the South-West Indian Ocean. It flows down the east coast of Africa from 27°S to 40°S. It is narrow, swift and strong. (source:wikipedia)

2001] used this finding in combination with the 1987 hydrographic data [Toole and Warren, 1993] to obtain new reference levels for the geostrophic flow field.

In this study the Bryden and Beal transport field is reproduced using their reference levels. Transport in the 'bottom triangles' is estimated by assuming a constant flow velocity from the deepest bin pair to the bottom and a linearly increasing cross section between the deepest station and its paired neighbour. This transport field gives an overturning of 10.1 Sv at 2000m (Table 2.1).

Ganachaud and Wunsch (2000)

Ganachaud and Wunsch estimated the global oceanic mass transport based on hydrographic data from the World Ocean Circulation Experiment (WOCE) [Ganachaud and Wunsch, 2002; Ganachaud, 2003]. The estimate is based on an inverse model that consistently combines all global sections [Wunsch, 1996; Ganachaud and Wunsch, 2002]. The solution for the mass transport across 32°S [Ganachaud, 2003] uses 1987 hydrographic data [Toole and Warren, 1993].

We have reproduced the reference velocities used in [Ganachaud, 2003] based on the mass transport in density layers as it is provided on Ganachaud's website[4]. Per station pair we require that the integrated transport for the surface referenced geostrophic velocity V plus some correction c equals the transport given in density layers integrated over the water column,

$$\sum (V_i + c) A\rho = \sum T_j, \tag{2.8}$$

where i runs over bins and j over density layers and A is the bin area including bottom triangles. Solving for c we obtain a reference velocity for each station pair.

[4]http://www.pmel.noaa.gov/people/ganachaud/glbwocemodel.html

This transport field gives an overturning of about 11 Sv at 2500m (Table 2.1).

Sloyan and Rintoul (2001)

The Sloyan and Rintoul solution for the transport across 32°S uses 1987 hydrographic data [Toole and Warren, 1993]. Inverse box model methods are applied to 15 layers defined by neutral density surfaces, ranging from 24 to 28.3 kg m^{-3} with a decreasing layer spacing towards the bottom. Mass, heat and salt are conserved for each layer and silica is conserved in the box. Further details can be found in [Sloyan and Rintoul, 2001].

We have reproduced the reference velocities in a fashion similar to (2.8). Instead of total mass transport per station pair we have used total volume transport per station pair, because the Sloyan and Rintoul solution was provided in this format.

The Sloyan and Rintoul transport field gives an overturning of about 23 Sv at 2600m (Table 2.1).

Ferron and Marotzke (2003) OGCM solution

The Indian Ocean overturning strength calculated with an ocean general circulation model (OGCM) tends to be weaker than the results from hydrographic inversions, as Table 2.1 shows. The model study by [Ferron and Marotzke, 2003] is an exception in the sense that it produces a relatively strong overturning, much stronger than other model results. Ferron and Marotzke use the MIT[5] ocean general circulation model.

At first the model is spun-up for 10 years using a climatology-based initial state. This produces a weak 6 Sv overturning, comparable to previously published model studies (refer to Table 2.1). The strong overturning develops only if hydrographic data are assim-

[5]Massachusetts Institute of Technology (USA)

Study	Method	T (Sv)
[Fieux et al., 1994]	JADE[a] August 1989	18 ± 7
[Fieux et al., 1996]	JADE February 1992	-2.6 ± 9[b]
[Macdonald, 1998]	Hydrography	10 ± 10[c]
[Zhang, 1999]	General circulation model	2.7
[Ganachaud and Wunsch, 2000]	Based on JADE	15 ± 3
[Hautala et al., 2001]	Pressure gauges / ADCP	8.4 ± 3.4
[Koch-Larrouy et al., 2006]	regional OGCM	16.4

Table 2.2: Indonesian Throughflow from various studies. The transport is westward, from the Pacific to the Indian Ocean.

[a] Java-Australia Dynamic Experiment.
[b] Minus sign denotes eastward transport (from Indian Ocean to Pacific).
[c] Actually given in kg per second and converted to Sverdrups using 1kg= 10^{-9}Sv.

ilated. The assimilation is an iterative process, where the model is rerun for a number of times and compared to WOCE sections and sea surface observations. Each iterative one-year run has a slightly modified initial state. The iteration is stopped at some optimal point, where the end state is close to the observations and the initial state is still realistic. [Palmer et al., 2007] however have shown that the MIT ocean GCM cannot produce a quasi-steady overturning state for any of the hydrographic flow fields when run with a realistic, observation-based diffusivity parameter.

The Ferron and Marotzke (2003) transport field gives an overturning of about 17 Sv at 3200m (Table 2.1).

2.3.3 Indonesian Throughflow (ITF)

Published estimates of the Indonesian Throughflow vary widely, with annual mean values ranging from -2.6 Sv (Indian-to-Pacific) [Fieux et al., 1996] to 18 Sv (Pacific-to-Indian) [Fieux et al., 1994]. Most studies however find an annual mean transport from the Pacific to the Indian Ocean (Table 2.2).

density [kg m^{-3} - 1000]	ITF [Sv]	RSW+PGW [10^5 kg s^{-1}]
$\rho \leq 26.50$	12.44	2.5
$26.50 < \rho \leq 26.90$	0.83	2.5
$26.90 < \rho \leq 27.36$	1.80	2.5
$27.36 < \rho \leq 27.78$	1.43	2.5
$27.78 < \rho \leq 27.96$	0.01	2.5
$27.96 < \rho \leq 28.11$	0.00	2.5
$28.11 < \rho \leq 28.23$	0.00	0.0
$\rho > 28.23$	0.00	0.0

Table 2.3: The Indonesian Throughflow (ITF) in density classes from [Koch-Larrouy et al., 2006]. Mass input from Red Sea (RS) and Persian Gulf (PG) is uniformly distributed over layers lighter than 28.11 kg m^{-3}. Note that in our calculations we normalise the ITF to the transport across 32°S.

We use a model study by [Koch-Larrouy et al., 2006] to obtain the Indonesian Throughflow transport into our density layers (Table 2.3). The total transport reported by [Koch-Larrouy et al., 2006] is 16.52 Sv, but we have scaled this value to match the discussed transport fields at 32°S, so that volume is conserved. The balance between the ITF and the transport across the southern boundary neglects the relatively small (less than 1Sv) fresh water flux.

2.3.4 Red Sea (RS) and Persian Gulf (PG)

The Red Sea (RS) and the Persian Gulf (PG) are strongly evaporative basins. The influence on the Indian Ocean is that of a 'salination machine', taking in relatively fresh surface water and producing an underlying outflow of very saline water. Table 2.4 gives some relevant properties of the RS and PG exit plumes. The plumes enter the Indian Ocean at less than 200m, because both marginal basins have a shallow sill at the strait connecting them to the Indian Ocean. The saline and dense plumes plunge down into the Indian Ocean as frictional density currents modified by rotation, rather than geostrophic currents modified by

intake	Red Sea	Persian Gulf	unit
depth	<200	<200	m
density	26.7[b]	25.4[b]	kg m^{-3}
salinity	36.0[b]	36.5[b]	psu
outflow plume			
annual mean outflow	0.37[a], 0.06–0.29[c]	0.2–0.25[b]	Sv
density	27.7[b]	28.2[b]	kg m^{-3}
salinity	40.5[a], 39.5[b]	40.3[b]	psu
equilibrium			
dilution factor	2.5[b]	4.0[b]	
depth	800–1300[c], 600[b]	250[b]	m
density	27.0–27.6[c], 27.2[b]	26.5[b]	kg m^{-3}

Table 2.4: Red Sea and Persian Gulf data. The dilution factor is based on the 1D streamtube entrainment model by [Price and Baringer, 1994] and calculated by [Bower et al., 2000].

[a] [Murray and Johns, 1997]
[b] [Bower et al., 2000]
[c] [Beal et al., 2000]
[d] [Matt and Johns, 2006]

friction. Entrainment dilutes the plumes until they reach buoyancy equilibrium. A model study by [Bower et al., 2000] shows that equilibrium is reached within 30km. Signatures of the RS plume however have been observed thousands of kilometers south of the RS [Beal et al., 2000]. Both studies report a comparable equilibrium depth, the model gives a depth of less than 800m for the RS water and about 250m for the PG water, and [Beal et al., 2000] found RS water at depths between 800 and 1300m in the Agulhas Current .

The annual mean total mass input from the RS and PG is about 1.5×10^6 kg s^{-1} and the equilibrium density is about 1027.2 kg m^{-3} [Murray and Johns, 1997; Bower et al., 2000; Beal et al., 2000]. The dense water plunging down into the Indian Ocean entrains ambient water until it reaches equilibrium. This process effectively transports mass away from the surface layer and puts it in deeper layers. It is assumed

that the 'mass leakage' from the plume is constant at all depths between the injection and the equilibrium depth. This distribution is chosen for its simplicity and loosely based on the observation that the acceleration and the surface area of the plume scale oppositely with respect to the density difference between the plume and surrounding water. This simplification will have little or no effect on the calculated energetics of the deep overturning because the RSW hardly penetrates below 1000m.

2.3.5 Climatology

The Hydrobase[6] climatology gives worldwide temperature and salinity values at 85 depth levels. We choose to use Hydrobase, because it averages seawater properties on potential density surfaces, instead of depth surfaces as in the Levitus Atlas. Averaging on density surfaces prevents artificial mixing of water mass properties and is therefore more suitable for our application. We use the Hydrobase 1×1 degree annual mean climatology for the Indian Ocean to estimate density surface areas and spacing between density surfaces.

The methods for obtaining these layer properties are as follows. (i) Calculate neutral densities for all data points using the CSIRO routine [Jackett and McDougall, 1997]. (ii) Check for latitudes north of 32°S whether there are densities equal to or larger than the given layer density. If so account for one surface area element of $4\pi^2 R^2 \cos(\phi)\, 360^{-2}$, with R the radius off the Earth and ϕ latitude. Adding up these area elements gives an estimate of the total area of the density surface.

[6] http://www.whoi.edu/science/PO/hydrobase/HB2_home.htm

2.4 Errors

The turbulent dissipation scales as $\epsilon\Gamma \propto F/A$ (2.7). The uncertainty in the layer area A is only 1-2% and will be neglected in this study. The 'mixing efficiency', $\Gamma \equiv R_f/(1-R_f)$, with R_f the flux Richardson number [Osborn, 1980], has a canonical value of 0.2 and will be treated as a constant. Thus, we ignore observational evidence suggesting that Γ, in fact, may be significantly variable [Peltier and Caulfield, 2003]. The uncertainties in the turbulent mass transport F depend on uncertainties in the transport and neutral density estimates.

2.4.1 Inverse model errors

The transport field is calculated from the velocity field, $T(x,z) = v(x,z)\Delta x\Delta z$. The velocity field is derived from an underdetermined inverse model with noisy constraints. Inverse model uncertainty is discussed in the next section. The error associated with the interpolation from depth-space to density-space, $T(z) \rightarrow T(\rho)$, and the uncertainty in neutral density will also be discussed.

The ocean circulation inverse problem

Deriving the flow field from salinity, temperature and pressure measurements is one of the fundamental problems in oceanography, involving basic concepts such as the equation of state and the geostrophic balance. Vertically integrating the thermal wind equation gives the velocity profile plus an unknown integration constant. Finding these constants is often referred to as the 'reference level problem', where a reference level is defined as the depth where the real ocean flow is zero or has some other known value.

Reference levels can be found by constraining the velocity, in principle requiring an independent constraint for each pair of hydrographic stations. Ocean circulation experiments are usually designed as a box model, so that tracer divergences (temperature, salinity, silica, etc.) can be measured and used as constraints. In the absence of sources and sinks in the box we may write,

$$\sum_{j=1}^{N} \Delta x_j \int \phi_i [v_j + b_j] dz \simeq 0, \tag{2.9}$$

with ϕ_i the concentration of tracer $i \in [1, 2, \ldots, M]$, and Δx the distance between a pair of hydrographic stations [Wunsch and Grant, 1982]. Separating the v and b terms and writing, $A_{ij} = \Delta x_j \int \phi_i dz$, and $c_i = -\sum_j \Delta x_j \int \phi_i v_j dz$, we can write this set of M equations with N unknowns as a matrix multiplication,

$$\mathbf{A}\mathbf{b} \simeq \mathbf{c}, \tag{2.10}$$

with $\mathbf{A} = (M \times N)$. Typically, there are more unknowns than independent constraints, that is the row rank R of $\mathbf{A}$ is smaller or equal to M and smaller than N. So $\mathbf{A}$ is usually rectangular with $R \leq M < N$, and strictly speaking not invertible. Solving such an underdetermined set of equations, with $(M - R)$ free variables, is what we refer to as the *inverse problem*.

Inverse methods deal with finding the *optimal* solution to an underdetermined problem. The optimal solution in the oceanographic context will be the velocity field that is closest to our current understanding of the ocean circulation. Details on inverse methods and their application in oceanography can be found in [Wunsch, 1996].

Noise and nullspace

It is a little miracle and at least remarkable that our understanding of ocean dynamics allows us to calculate a flow field from salinity, temperature and depth measurements (plus some knowledge of the wind field). But of course we are only really impressed if the calculated flow field is close to real ocean velocity field. In other words, suppose we write the 'real velocity' as,

$$v = v_R(S,T,P) + v_E(\tau) + b + e, \tag{2.11}$$

where e is the error,v_E the Ekman velocity calculated from wind stress τ, v_R the geostrophic velocity with a 'best guess' for the reference levels, and b the correction to the reference level velocities, we would like to see $e << v$.

One source of error is our limited knowledge of the observables, S,T,P, and τ, which we will refer to as 'noise'. Another error comes into play when $\mathbf{A}$ (refer to (2.10)) does not have an inverse. The row space of matrix $\mathbf{A}$ is usually rank deficient (more station pairs than constraint equation), which means that the nullspace contains $(M - R)$ independent vectors $\mathbf{q}$: $\mathbf{Aq} = \mathbf{0}$. The nullspace vectors can be freely added to any particular $\mathbf{b}$ satisfying $\mathbf{Ab} = \mathbf{c}$, giving indefinitely many solutions for b.

Singular Value Decomposition (SVD) is a method to find a pseudo-inverse for $\mathbf{A}$, that minimizes both $||\mathbf{b}||$ *and* $||\mathbf{Ab} - \mathbf{c}||$. In physical terms this means that SVD will find *one particular* solution with reference levels and property divergences as close as possible to the a priori 'guesses'. Inherently, SVD is sensitive to the a priori choices made by the investigator. Two investigators, given identical datasets (CTD, wind stress, and tracer concentrations), may construct different physical models and obtain *different* velocity

fields.

The so called nullspace– or omission error comes from incompleteness of the model, when some of the physics determining **b** are missing. This model specific error will contribute to the uncertainty in the velocity field, together with the noise in the data. A formal way of quantifying these uncertainties is described in [Wunsch et al., 1983].

2.4.2 Interpolation errors

An interpolation method to find the transport into density layers is presented in Section 2.2.2. This method assumes constant transport in the neighbourhood of the density surfaces that define the layer. The error associated with this assumption is estimated by quantifying the deviation from a velocity profile with a linear vertical gradient, $v(z) = v_0 + (z - z_0)v_z$, with z_0 the mid-depth of the bin, and v_0 the mean flow velocity. We may translate the origin to the bottom of the bin by transforming the vertical coordinate, $z' = z - (z_0 - \Delta z/2)$, with Δz the vertical bin size. The fractional bin transport for a linear velocity profile is, $T = \Delta x \int_0^L v(z')\, dz'$, with $L < \Delta z$, and Δx the horizontal bin size. The transport difference, when compared with a constant velocity profile, is $v_0 \Delta x L - \Delta x \int_0^L v(z')\, dz' = \frac{1}{2}\Delta x\, v_z[\Delta z\, z' - z'^2]$, which is maximum at $z' = \frac{1}{2}\Delta z$, giving a maximum difference of $\Delta T = \frac{1}{8} v_z \Delta x \Delta z^2$.

The vertical shear v_z below 1000m is typically of order $1 \times 10^{-6}\mathrm{s}^{-1}$ and usually everywhere less than $5 \times 10^{-4}\mathrm{s}^{-1}$. Calculating ΔT for the Sloyan and Rintoul velocity field [Sloyan and Rintoul, 2001] gives a maximum relative error of less than 5% for the transport into a layer with at least 8 bins in the vertical direction. Note that the relative interpolation error is larger for thinner layers with fewer bins in the vertical

direction.

2.4.3 Neutral density errors

The neutral density is calculated as a function of salinity, temperature, pressure, longitude and latitude using the CSIRO[7] routine [Jackett and McDougall, 1997]. The routine provides an error estimate $\Delta\gamma$. Multiplying this error with $\frac{dp}{d\gamma}$ gives the uncertainty in pressure Δp and we find that large uncertainties are associated with weakly stratified deep waters, easily exceeding the vertical bin size of 20dbar.

The uncertainty in the depth of isopycnals also makes the estimates of the transport into density layers uncertain. The relative error in the layer transport is larger for thinner layers and blows up in dense, weakly stratified water. Based on the density error estimates given by the CSIRO routine we estimate that the relative transport error can be kept smaller than 6% when avoiding layers with $\gamma > 28.15$ and maintaining a minimum layer thickness of about 200m.

2.4.4 Error propagation

The quantity of interest in the study is the dissipation rate, $\epsilon \propto F/A$ (refer to (2.7)), where the turbulent mass flux, F, is a superposition of mass flux terms, $T\rho$, with error contributions from three sources, (i) inverse model, (ii) interpolation, and (iii) neutral density. These errors are not fully independent, and inverse model errors tend to diminish when integrated spatially [Wunsch, 1996]. The error in F is therefore assumed to be equal to the transport error in the top density layer, without contributions from deeper layers.

[7] Commonwealth Scientific and Industrial Research Organisation (Australia)

Assuming a relative error of 5% error due to interpolation, a 5% error due to the uncertainty in the density, a standard transport error in the top layer of σ_T, and regarding these errors as independent, gives a dissipation error of,

$$\sigma_\epsilon = \sqrt{\left(\frac{\sigma_T}{T}\epsilon\right)^2 + 2(0.05\epsilon)^2}, \tag{2.12}$$

with T the transport in the top layer and $\epsilon = \frac{F}{A}\frac{g}{\rho\Gamma}$ (refer to (2.7)) the dissipation rate.

2.5 Results

2.5.1 Transport into density layers

Using the methods described in Section 2.2.2 we calculated the transport into 26 density layers (Fig. 2.7) defined by 25 density interfaces, ranging from 22.42 to 28.15 kg m^{-3} (refer e.g. to Table 4.1). When calculating the turbulent mass transport (Section 2.2.1) we find that the exact choice of density layers does not matter, as one would expect (refer to Appendix A). To avoid significant errors in the estimated depth of isopycnals in weakly stratified waters (refer to Section 2.4.3) we do not resolve density layers below 25.15 kg m^{-3}. This means that the bottom layer is several times thicker than the other layers, up to a thickness of about 1200m, whereas other layer are typically 200m thick, as Fig. 2.7 shows. The low density resolution near the bottom means that we lack knowledge about the turbulent mass transport below 25.15 kg m^{-3}. This may lead to under-/overestimation of the mixing in the bottom layer of there is less/more water mass transformation within the layer than at the 25.15 kg m^{-3} density level.

The overturning streamfunction (OSF) is often used

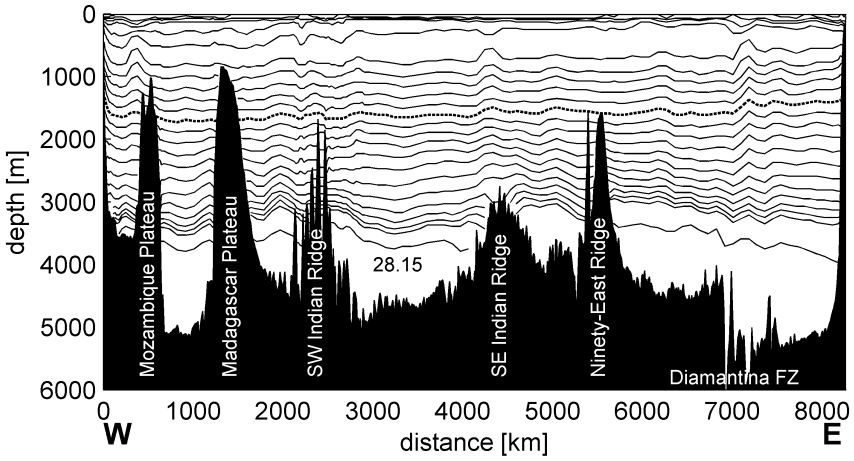

Figure 2.7: Vertical cross-section at 32°S with Sandwell and Smith bathymetry (v8.2) and the neutral density layers used in our advection–diffusion model.

to characterize the overturning circulation. Traditionally the OSF is the zonally-integrated meridional flow along surfaces of constant depth, $\psi(z) = \int_{z_{max}}^{z} \int V(y, z')\, dy\, dz'$. The left panel of Fig. 2.8 shows the traditional OSF for the five solutions for the flow across 32°S considered in this study. The main features of the OSF are (i) the *overturning strength* or maximum, (ii) the *overturning depth*, that is the depth of the maximum, where the direction of the flow reverses (refer to Table 2.1), and (iii) the *closing depth* or zero-crossing, where the inflow is balanced by the return flow.

Alternatively, the OSF can be calculated in density space, by integrating along isopycnals instead of isobaths. Figure 2.7 shows the density layers used in this study. Using the 'density streamfunction' is advantageous in mixing problems, because it respects water masses and is explicit about diapycnal transports. The right panel of Fig. 2.8 shows the density OSF, $\psi(\gamma)$, plotted against depth by labelling the isopycnals with a typical mean depth[8]. Comparing the traditional

[8]The mean isopycnal depth is calculated using the Hydrobase climatology in a central

OSF, in the left panel, with the density OSF, we see that they have most features in common. For example, the strength and depth are similar. The most apparent differences between the OSFs are: (i) the depth range (the traditional OSFs extent to larger depth), (ii) $\psi_{McD}(z)$ is negative at bottom and $\psi_{McD}(\gamma)$ positive, (iii) the maximum of $\psi_{McD}(\gamma)$ is deeper than the maximum of $\psi_{McD}(z)$, and (iv) $\psi_{Fer}(z)$ is deeper than $\psi_{Fer}(\gamma)$.

The difference in depth range is simply explained by the choice of the densest density layer. Figure 2.7 shows that the deepest isopycnal (28.15) indeed lingers around 4000m. The other differences can be explained by zonal asymmetries in density and bathymetry. The densest waters with $\gamma \geq 28.15$ only exist west of the South-east (SE) Indian Ridge, whereas the deepest waters below 5000m are found in the east. The effect of this asymmetry is most profound for the McDonagh et al. overturning solution, because $\psi_{McD}(z) < 0$ for $z > 5000$m, that is the deepest water in the east flows *southward*.

This suggests that the inflow of bottom water, with a density larger than 28.15, is restricted to the western half of the basin, where deep trenches in the Southwest Indian Ridge (SWIR) offer passageways. Some of the inflowing water appears to make it past the Central Indian Ridge (CIR) and the Ninety-east Ridge, thus constituting the deep return flow through the Diamantina Fracture Zone (DFZ) (refer to Fig. 2.4 for an overview of the main topography in the Indian Ocean). The bottom retro-flow in the east appears unaffected by the ITF as ITF water is not expected to penetrate below the 27.78 isopycnal (Table 2.3).

Figure 2.9 shows how the OSF changes when we add the ITF. The ITF total transport is chosen to

Indian Ocean area with $\mathbf{lat} = [-41 : 1 : -21]^\circ$ and $\mathbf{lon} = [60 : 1 : 80]^\circ$.

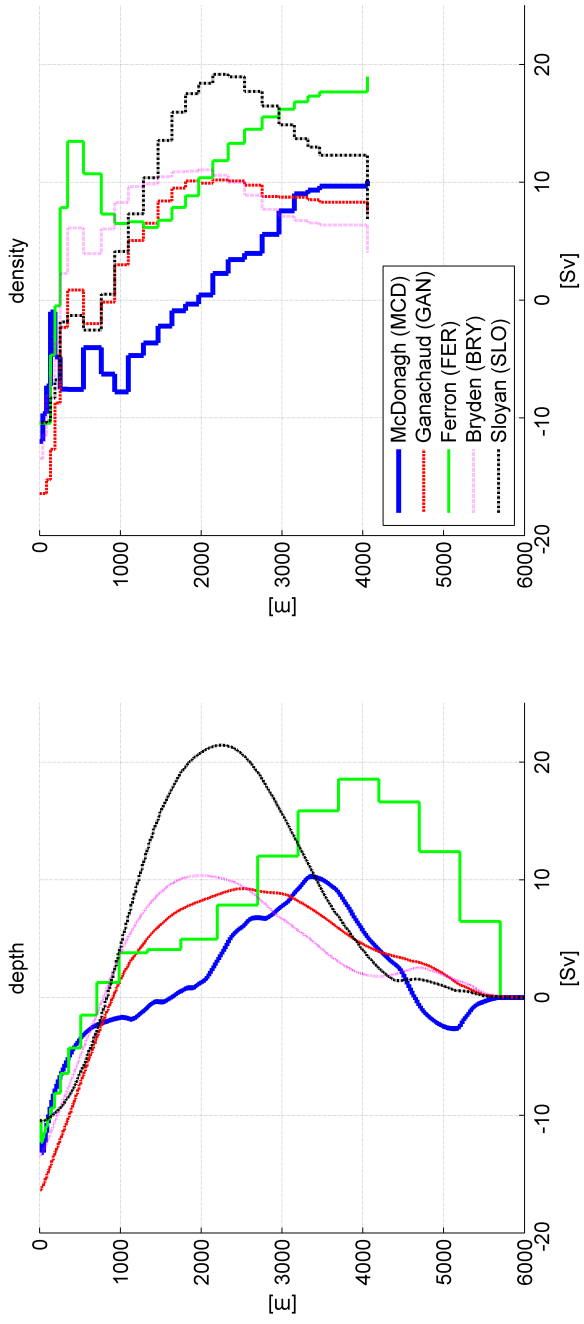

Figure 2.8: The overturning streamfunction (OSF) for various solutions for the transport across 32°S (Table 2.1). Left: the OSF calculated in depth coordinates. Right: the OSF calculated in density coordinates. The density coordinates in the right panel are transformed to depth by calculating the mean isopycnal depth using the Hydrobase climatology in a central Indian Ocean area with **lat** = $[-41:1:-21]^\circ$ and **lon** = $[60:1:80]^\circ$.

match the total transport across 32°S, so that the bottom integrated transport adds up to zero. The figure also shows that ITF water does not penetrate below 1200m in our model.

2.5.2 Turbulent mass transport

The turbulent mass transport is calculated from layer transport using the advective–diffusive balance (2.3). Figure 2.10 shows the turbulent mass transport, F, for the five overturning solutions considered in this study. The figure also shows the 'ingredients' that go into (2.3), that is the density profile and the layer transport. Also shown is the overturning streamfunction, ψ, which is the bottom-up integrated layer transport, $\psi_i = \sum_{j=1}^{i} T_j$. Below we discuss how F is related to the overturning streamfunction, and in particular how F can become negative, as is the case for the [McDonagh et al., 2008] solution.

Generally the global overturning circulation is thought of as a flow circuit with downwelling at a number of high latitude sites[9], and upwelling elsewhere. The Indian Ocean appears to accommodate an important deep upwelling branch of the global MOC [Schmitz, 1995]. Upwelling needs upward turbulent mass transport, i.e. positive F, to maintain the density stratification of the ocean, and this is what we find for all the Indian Ocean overturning solutions below 1000m (Fig. 2.10).

At shallower depth we obtain *negative* mass transport for the [McDonagh et al., 2008] solution. The negative, shallow F is unique to the [McDonagh et al., 2008] solution and suggests a different overturning structure. Advective mass divergence is needed for F to become negative. This means that, when F becomes

[9]Deep water is formed due to cooling and brine exclusion when seawater freezes.

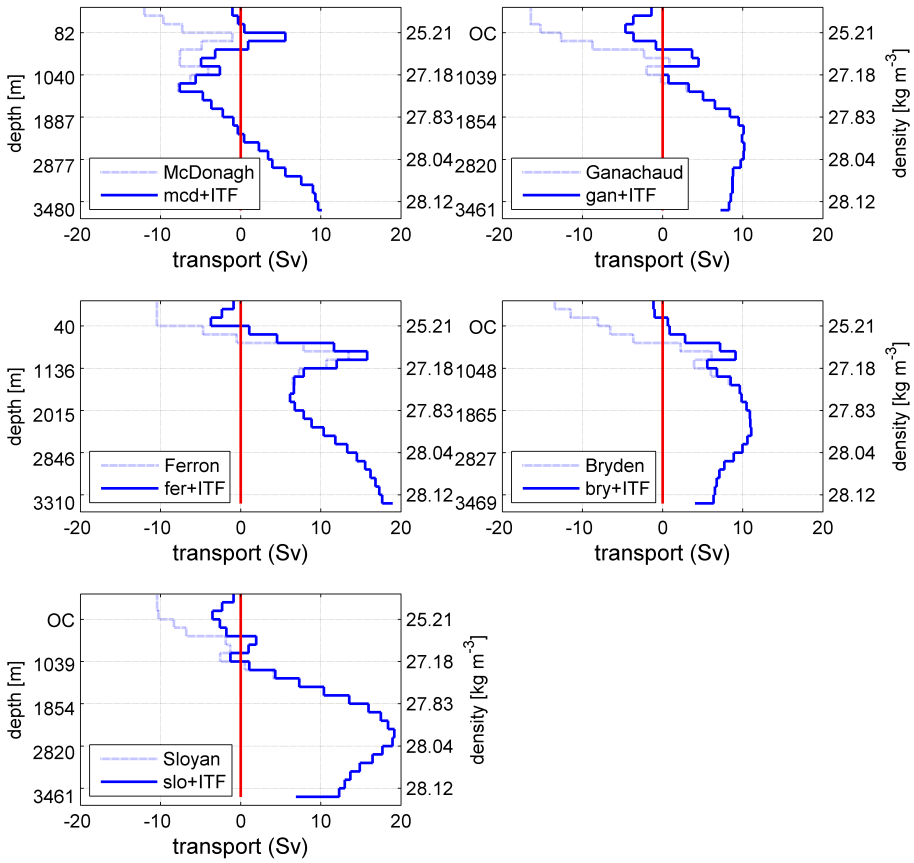

Figure 2.9: Comparison of overturning streamfunctions (OSFs) based on transport across 32°S without ITF (dashed line) and with ITF (solid line). The OSF is calculated in density space and the ITF strength is chosen to balance the transport across 32°S (refer to Section 2.3.3). The depth labels are based on the interpolated depth of the density layers at the deepest station of the section. Positive transport is northward and the label 'OC' means 'outcropping' and indicates that isopycnals come to the ocean surface.

negative, there is more mass flowing out of the layer than flowing in, which can only happen when there is *downwelling* through the top layer interface. In that case, the input of lower density water at the top will be volumetrically balanced by the outflow of higher density at the lateral boundary. This leads to net mass divergence if the mass input at the bottom is zero or small and requires a negative mass flux F at top interface to close the mass budget.

When F becomes negative we cannot think of it as being driven by diapycnal diffusion only, $F \neq F_{diff} = \overline{K_\rho \rho_z} A$, because F_{diff} is positive definite for a stably stratified ocean (refer to Section 2.2.1). Another physical process must be taken into account, so that $F = F_{diff} - F' < 0$. A possible explanation for the downward mass transport near the surface is deep convection due to buoyancy exchange at the surface. For example, the strong net evaporation in the Red Sea and the Persian Gulf leads to the production of saline water that penetrates into the Indian Ocean to a maximum depth of 1300m [Beal et al., 2000]. The production of Red Sea Water and Persian Gulf Water might explain the double-cell overturning circulation found by [McDonagh et al., 2008], with an upwelling cell in the deep ocean below 1000m and a downwelling cell above this depth.

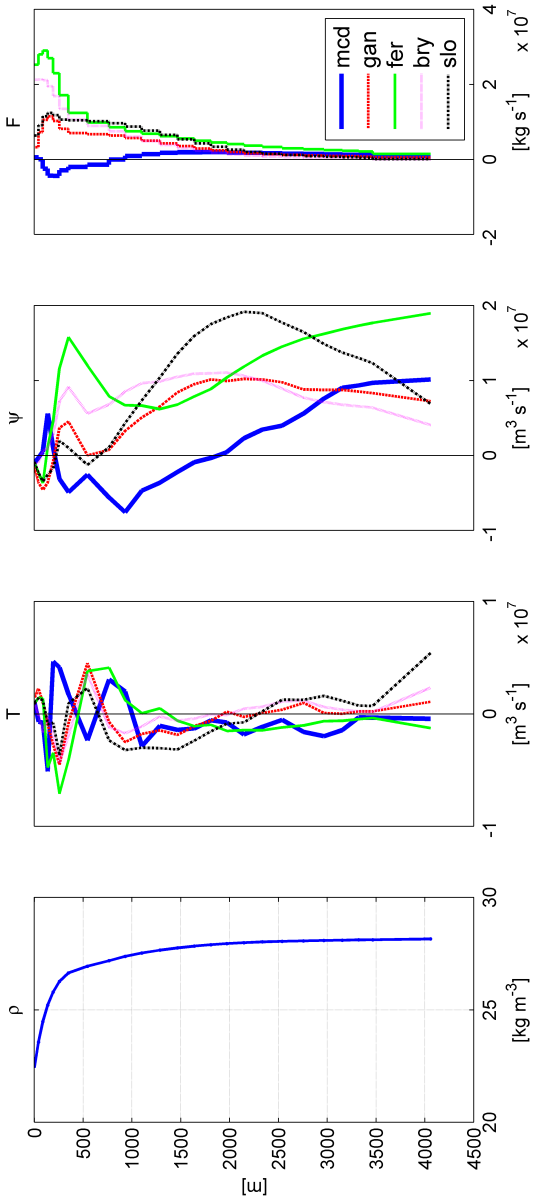

Figure 2.10: Turbulent mass transport, F, obtained from the density distribution, ρ, and the layer transport T. The overturning streamfunction ψ is the bottom-up integrated layer transport.

2.5.3 Turbulent dissipation and diffusivity

The main results of this chapter are shown in Fig. 2.11. The top panel shows the basin-wide mean dissipation rate (2.7), the bottom-left panel shows the isoneutral mean buoyancy frequency, N^2, and the bottom-right panel shows the diffusivity, K_ρ. The buoyancy frequency is calculated from the WHOI Hydrobase climatology, using the `sw_bfrq` MATLAB routine from the CSIRO seawater package, and linearly interpolated onto neutral density levels using the CSIRO neutral density routine [Jackett and McDougall, 1997]. The turbulent eddy diffusivity calculated from the dissipation estimates using the Osborn relation (2.6).

The figure shows that the dissipation profiles obtained from the older 1987 data increase towards the surface, whereas the [McDonagh et al., 2008] dissipation profile, based on the new data from 2002, decreases above 1500m. This new dissipation profile has a maximum around 2000m and becomes negative around 900m. In the context of this work we interpret negative ϵ as a loss rate of potential energy.

The total power to sustain the overturning circulation is calculated by bottom-up integration of the dissipation rate [W kg^{-1}] multiplied by mass,

$$P_{tot} = \rho_0 \sum_{i=1}^{i_{max}} \epsilon_i \, A_i \, \Delta z_i, \tag{2.13}$$

with $i = 1$ the bottom layer and i_{max} the layer corresponding to the 'closing density' of the overturning streamfunction. The closing density is the density level where the overturning streamfunction is zero, which is the point where the deep inflow is balanced by the shallower retro-flow. Table 2.5 lists the closing densities for the various overturning solutions considered in this study.

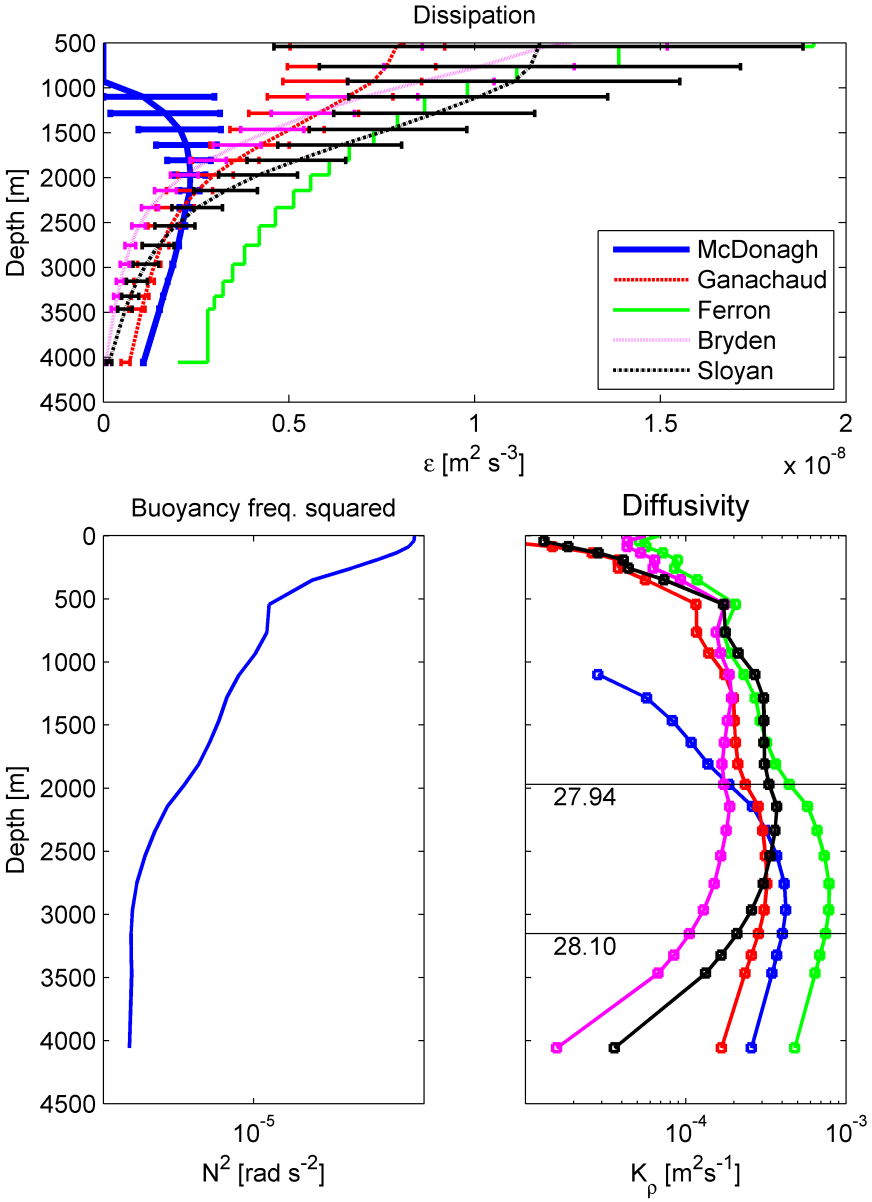

Figure 2.11: Mixing estimates inferred from a basin-wide mass balance in density layers for five different overturning solutions. Top: dissipation estimates [Wkg^{-1}] with error estimates (based on the uncertainties discussed in Section 2.4). Bottom left: Isoneutral mean buoyancy frequency based on the Hydrobase climatology. Bottom right: diffusivity estimates as calculated using the Osborn relation Osborn [1980], $K_\rho = 0.2\epsilon/N^2$. The horizontal black lines indicate neutral density levels that we use to distinguish between bottom water and deep water.

ID	Ψ_{max} [Sv]	z_{max} [m]	γ_0 [kg m^{-3}]	z_0 [m]	P [TW]
mcd	10.1	4058	27.92	1877	0.17
fer	19.0	4058	25.04	124	1.19
slo	19.2	2146	27.07	667	0.94
gan	10.2	2146	26.93	539	0.68
bry	11.1	1971	24.12	65	0.78

Table 2.5: Estimates of the total dissipated power, P, needed to sustain the deep Indian Ocean MOC. Also shown are, the overturning maximum Ψ_{max}, the depth of the overturning maximum z_{max}, the closing density γ_0, and the approximate depth of the closing density, z_0. The power is calculated by integrating the dissipation rate from the bottom up to the closing density. The closing density corresponds to the zero-crossing of the overturning streamfunction and represents the density level where the the inflow of dense bottom and deep water is balanced by the more shallow and less dense retro-flow. We attribute the difference between the overturning maxima, Ψ_{max}, and the published maxima in Table 2.1 to the fact that we calculated the overturning maximum in density space as opposed to depth space.

The layer spacing Δz used in (2.13) to calculate the layer volume between layer interface $(i-1)$ and i is found by: (i) labelling the Hydrobase grid points with neutral density, (ii) interpolating the layer depths, and (iii) calculating the mean vertical distance between the layers.

The energy requirements of the various overturning solutions are listed in Table 2.5. The next section puts these numbers into a global context. When interpreting these numbers it is useful to realize that we have used a variable closing density, dependent on the particular shape of the overturning solution. This means that the total required power represents different ocean volumes for the different solutions. Integrating all solutions up to the same density level is therefore likely to change the relative magnitude of the power estimates.

For example, we may integrate all dissipation profiles up to a density of 27.78, well below the expected

influence of the ITF, RSW, or PGW, to find the numbers labelled P_{deep} in the last column of Table 2.5. Unsurprisingly, we find that most solutions require less energy when integrated over a smaller density range, except for the [McDonagh et al., 2008] solution. This can be explained by the fact that the [McDonagh et al., 2008] dissipation profile becomes negative at some density just below the chosen closing density.

2.6 Discussion

The turbulent diffusivity estimates, as displayed in Fig. 2.11, are in reasonable agreement with previously published estimates. To our knowledge, the only other basin-wide diffusivity estimates, based on Indian Ocean WOCE data, were published by [Ganachaud and Wunsch, 2000; Ganachaud, 2003]. They estimated $K_\rho = 4 \pm 2 \times 10^{-4}$ m^{2}s^{-1} in the deep Indian Ocean ($27.96 < \gamma < 28.10$ kg m^{-3}), and $K_\rho = 12 \pm 7 \times 10^{-4}$ m^{2}s^{-1} for the bottom layer ($\gamma > 28.10$ kg m^{-3}). Our diffusivity estimates for the Ganachaud et al. overturning solution agree with their estimates for the deep layer, but are smaller for the bottom layer. This maybe due to the limited density resolution near the bottom in our model (refer to Section 2.5.1). Other studies, focussing on particular areas of the Indian Ocean, have produced diffusivity estimates in the range from 3.5 to 35 cm^{2}s^{-1}, as listed in Table 2.6.

The estimates of the power needed to sustain the deep Indian Ocean MOC become more meaningful when compared to the available energy. The dynamically important energy sources for the large scale ocean circulation are winds and tides [Wunsch and Ferrari, 2004]. In an attempt to close the energy budget of the deep Indian Ocean we consider abyssal energy sources only, that is (i) wind power input to the geostrophic flow,

Study	K [$cm^2 s^{-1}$]	Remarks
[Ganachaud and Wunsch, 2000]	4 ± 2	Indian Ocean, $27.96 < \gamma \leq 28.10$
	12 ± 7	Indian Ocean, $\gamma > 28.10$
[Barton and Hill, 1989]	10.6 ± 2.7	Amirante Passage[a], 1.12°C
[Johnson et al., 1998]	3.5	Amirante Passage[a], 1.1°C
[Sloyan, 2006]	$13 - 15$	Perth Basin, 0.64°C $\sim$ 28.2 kg m^{-3}
	~ 10	Perth Basin, inferred from strain in abyss
[McCarthy et al., 1997]	35 ± 14	Ninetyeast Ridge, σ_4 = 45.92 kg m^{-3}

[a] between Mascarene Basin and Somali Basin.

Table 2.6: Diffusivity estimates in the Indian Ocean.

(ii) wind power input to downward propagating near-inertial motions, and (iii) tidal energy input to baroclinic internal waves.

All published energy inputs have considerable uncertainties and we therefore choose to work with a minimum and a maximum estimate (Table 2.6). The minimum wind-to-inertial flux is based on a factor 0.5 correction to the [Alford, 2003] estimate, as suggested by [Plueddemann and Farrar, 2006], integrated over the Indian Ocean north of 32°S. The maximum estimate is based on the full [Alford, 2003] estimate of energy input to near-inertial motions, integrated over higher southern latitudes, up to 50°S, to account for the fact that near-inertial waves travel to regions with lower planetary vorticity, that is equatorward.

The lower and upper estimate for the energy transfer between the wind field and the surface geostrophic currents are based on the uncertainty in the global value in [Scott and Xu, 2009]. The low and high value for the energy input in baroclinic tides is based on

energy source	reference	P_{lo} [TW]	P_{hi} [TW]
wind inertial	[Alford, 2003]	0.02[a]	0.09[b]
wind geostrophic	[Scott and Xu, 2009]	0.05	0.06
baroclinic tide	[Egbert and Ray, 2000]	0.11	0.18[c]
total		0.18	0.31

Table 2.7: Energy input to the deep Indian Ocean north of 32°S.
[a] factor 0.5 correction to [Alford, 2003] based on [Plueddemann and Farrar, 2006].
[b] [Alford, 2003] extended to 50°S.
[c] same as [Nycander, 2005] estimate.

error estimates by [Egbert and Ray, 2000]. We also calculated the tidal energy based on the [Nycander, 2005] global map and found it to be indistinguishable from the [Egbert and Ray, 2000] upper estimate.

The estimates of the energy going into the Indian Ocean should be enough to balance the implied dissipation needed to sustain the deep Indian Ocean MOC if the energy input is near-locally dissipated. Assuming that the energy flux into or out of the Indian Ocean is small compared to the local sources we may compare the energy inputs in Table 2.6 with the estimates of dissipated power in Table 2.5. This comparison tells something about the energetic feasibility of the various MOC solutions. For example, the power, when integrated up to the closing density, varies between 0.24 and 1.57 TW. We note that only the 0.24 TW MCD solution dissipates less than the 0.31 TW estimated maximum energy input. This results suggests that energy budgets may be useful as an additional constraint in inverse models.

The energy needed to sustain a particular MOC configuration depends on the amount of diapycnal transport, that is the MOC strength, and the density gradient below the closing density. The most distinct feature of the MCD solution is that it closes at a much

higher density, that is deeper, than the other MOC configurations. Deeper closure means that 'fewer' isopycnals are crossed, and that less diapycnal mass transport is needed to balance the advective inflow.

In this section we have estimated the levels of turbulent dissipation needed to sustain various published solutions for the Indian Ocean MOC. In the next chapter we will estimate the energy in the internal wave field and Chapter 4 assesses whether the Indian Ocean MOC can be driven by breaking internal waves.

2.7 Summary and conclusion

This chapter compares the energetics of various solutions for the Indian Ocean MOC. The energetics are evaluated by assuming mass conservation in density layers and an one-dimensional balance between advection and diapycnal diffusion. The energy needed to sustain a given MOC is defined as the total amount of work required to lift mass against gravity in order to preserve the vertical density stratification. Similar methods are discussed and applied to the global ocean by for example [Munk and Wunsch, 1998] and [Klocker and McDougall, submitted 2009].

This work focusses on the energetics of the deep MOC (roughly below 1000m) in the Indian Ocean north of 32°S. The advective mass budget in this part of the ocean is dominated by transport across the open southern boundary. For completeness we also incorporated the Indonesian Throughflow and water mass exchanges with the Red Sea and the Persian Gulf in our model, although this hardly affects the deep MOC.

Our model shows that various MOC solutions, based on hydrographic measurements along 32°S, require different levels of turbulent dissipation, varying between 0.24 and 1.57 TW. These numbers are large in com-

parison to the estimated global dissipation of 2.1 TW [Wunsch and Ferrari, 2004], especially considering the relatively small size of the subtropical Indian Ocean (about 12% of the world ocean[10]). Based on global maps of the generation of internal tides [Egbert and Ray, 2000] and near-inertial waves [Alford, 2003] we estimate that at most 18% of the global total, that is 0.36 TW, is dissipated in the Indian Ocean.

The value of 2.1 TW for abyssal dissipation is rather weakly constrained due to considerable uncertainties with regard to the conversion efficiency of wind energy into near-inertial motions. However, following [Wunsch and Ferrari, 2004], and accepting this number as an upper bound, leads us to conclude that the inverse model solutions for the Indian Ocean MOC are energetically infeasible when integrated up to the 'closing density', except for the less energy hungry [McDonagh et al., 2008] solution. This result suggests that energy budgets may be useful as an additional constraint in inverse models.

Avoiding the influence of the ITF on our power estimates, by limiting the MOC integration range to the highest ITF density class, gives numbers lower than 0.36 TW for all overturning solutions, except for the [Ferron and Marotzke, 2003] model result. We emphasize however that this is likely an underestimate, because it does not fully include the returning limb of the deep overturning cell for most solutions. Despite our doubts about the optimal integration range, and other uncertainties inherent to hydrographic inverses, we conclude that our estimate of the energetics of the Indian Ocean MOC has produced large numbers, as compared to estimates of the global dissipation. This result is consistent with the view that the

[10]The subtropical Indian Ocean is defined as the Indian Ocean north of 32°S. The surface area is calculated at a depth of 500m.

Indian Ocean MOC is an important deep upwelling cell in the global MOC, but also raises questions about the supply of the required high levels turbulent kinetic energy (TKE). Internal waves are generally regarded as the main agents of TKE in the deep ocean and we will discuss internal wave energy levels and dissipation mechanisms in the remainder of the work.

Chapter 3

Turbulent dissipation inferred from fine scale shear and strain

3.1 Introduction

Turbulence in the open ocean interior, away from the surface boundary layer, the bottom boundary layer and sites of deep convection, is generally thought to originate from internal wave breaking. Internal waves fill the ocean with motions at a large range of spatial scales and are important for energy transport throughout the ocean, both in physical space and in wave number space.

Numerical simulations have shown that nonlinear interactions among internal waves cause a net transfer of energy to smaller scales [McComas and Müller, 1981; Henyey et al., 1986]. The energy flux towards smaller scales is often referred to as the 'energy cascade' and is a key process in the oceanic energy balance. The cascade transfers energy from large scale sources, mainly wind forcing at the surface, and tidal

flows, to fine scale (order 10m) waves that will eventually break into small scale (order 1cm) turbulent motions when the shear overcomes the stratification. The rate at which breaking waves dissipate energy is approximately equal to the downscale transfer rate of energy, which allows the dissipation rate to be expressed in terms of internal wave parameters.

In this chapter we discuss the fine scale parameterization of turbulent dissipation. Section 3.2 describes the model configuration, Section 3.3 the data we used for our analysis, and Sections 3.4 and 3.5 discuss the model output.

The main purpose of this chapter, in the context of the rest of the thesis, is a 'description of methods'. We use the fine scale parameterization as a tool to 'produce' dissipation rates with the aim to make a comparison between fine scale and large scale dissipation estimates. However, when using the tool we encountered some inconsistencies in comparison to previously published estimates.

3.2 Methods

3.2.1 Finescale parameterization of turbulent dissipation

The promise that internal waves hold information about turbulence has motivated the construction of several models that relate the turbulent dissipation rate to internal wave parameters (see [Polzin, 1995] for an overview). Such a parameterization is useful, because more direct observations of turbulence require special equipment and more expensive operations, whereas fine scale internal waves are picked up in conventional hydrographic measurements.

Validation experiments by [Gregg, 1989] and [Polzin, 1995] compare finescale parameterizations of dissipa-

tion with microstructure measurements and conclude that the Henyey, Wright and Flatté (HWF) model [Henyey et al., 1986] behaves favourably. HWF use ray tracing to estimate the energy transfer between a test wave and a background wave field and formulate a model to extrapolate their numerical findings in parameter space. The model is based on a Richardson number hypothesis and predicts that the dissipated rate [W/kg] scales as,

$$\epsilon \propto E^2 N^2 f \cosh^{-1}(N/f), \tag{3.1}$$

with E the internal wave energy density. Note that the dissipation rate scales with depth through the buoyancy frequency $N(z)$ and with latitude through the inertial frequency f.

The usefulness of the above scaling for the inference of turbulence from measurements was first demonstrated by Gregg in 1989 [Gregg, 1989], referred to as 'G89' hereafter. Gregg uses the energy density of the Garrett-Munk (GM) internal wave model [Garrett and Munk, 1972] [Garrett and Munk, 1975; Cairns and Williams, 1976] for E and introduces an additional factor to account for deviations from GM conditions. This factor is the square of the measured vertical shear variance normalized by shear variance in the GM model, both integrated over the same wavenumber band, $\left\langle S^2/S^2_{GM} \right\rangle = \int_{k_1}^{k_2} S^2(k)/S^2_{GM}(k)\, dk$, with $S(k) = A\mathcal{F}^2[V_z]$, where V_z is vertical shear, $\mathcal{F}$ the Fourier transform, and A an appropriate normalization factor so that variance is conserved (refer to Section 3.2.2). The shear ratio $\langle S/S_{GM} \rangle$ represents the energy in the internal wave field in units of the GM energy level.

Comparing the finescale model with dissipation rates inferred from microstructure measurements Gregg concludes that $\epsilon = \epsilon_0 \left\langle S^4 \right\rangle N^2$ to within a factor of 2 for

an appropriate scaling factor ϵ_0. Comparison with additional measurements in a subsequent study [Gregg et al., 2003] verified the latitudinal dependency factor $f \cosh^{-1}(N/f)$ in the HWF model. This factor accounts for the slower rate at which wave energy is transferred to dissipation scales at low f (i.e. low latitude) [Gregg et al., 2003].

Another modification of the original G89 parameterization is the inclusion of the shear-to-strain ratio R to account for the dominant frequency in the observed wave field [Polzin, 1995]. This factor appears in a simplified form in [Gregg et al., 2003], refer to (3.4) and (3.7), and is also included in the parameterization used in this study.

The parameterization is usually applied to (semi overlapping) vertical segments of measurements from a hydrographic cast. The segment length and the bin size of the data within the segment determine the possible integration range of both shear and strain spectra. Shear is the vertical gradient of the horizontal flow velocity and is usually measured using a lowered acoustic Doppler current profiler (LADCP) with a typical bin size of 20m. Strain is the vertical gradient of the displacement of isopycnals by internal waves and is calculated using the local relative change in buoyancy frequency,

$$\xi_z = \frac{N^2 - \langle N^2 \rangle}{\langle N^2 \rangle}, \tag{3.2}$$

where the brackets $\langle . \rangle$ indicate spatial averaging. The buoyancy frequency is calculated from CTD measurements with a typical bin size of 2m (see Section 3.2.4 for details).

Putting everything together gives the relation between fine scale internal wave parameters and turbulent dissipation used by [Kunze et al., 2006] and in this

study,

$$\epsilon = \epsilon_0 \frac{N^2}{N_0^2} \frac{\langle S \rangle^2}{\langle S_{GM} \rangle^2} h_1(R)\, L(f, N), \quad \text{with} \tag{3.3}$$

$$h_1(R) = \frac{3}{4}\left(1 + \frac{1}{R}\right)\left(\frac{R}{R-1}\right)^{\frac{1}{2}}, \quad \text{and} \tag{3.4}$$

$$L(f, N) = \frac{f \cosh^{-1}(N/f)}{f_{30} \cosh^{-1}(N_0/f_{30})}, \tag{3.5}$$

with $\epsilon_0 = 6.73 \times 10^{-10}$ m^{2}s^{-3} the canonical GM dissipation rate, S the shear variance spectrum normalized by the buoyancy frequency or the strain variance spectrum, R the shear-to-strain ratio (3.7), $N_0 = 5.24 \times 10^{-3}$ rad s^{-1} the canonical Garrett-Munk buoyancy frequency, and f_{30} the inertial frequency at 30° latitude [Gregg et al., 2003; Kunze et al., 2006].

The buoyancy-frequency-normalized shear spectrum $S[V_z/\overline{N}]$ is calculated directly from the velocity variance using $S[V_z] = k_z^2 S[V]$, with k_z the vertical wavenumber (refer to Section 3.2.2 and 3.2.3 for more details on the spectrum). The brackets $\langle . \rangle$ in (3.3) indicate integration of the shear spectrum over a given wave number band. The Garrett-Munk shear spectrum S_{GM} is integrated over the same wave number band. The GM76 expression for the shear spectrum is,

$$S_{GM}[V_z/N] = \frac{3}{2}\pi E_0\, b\, j^* \frac{k_z^2}{(k_z + k_z*)^2}, \tag{3.6}$$

with energy level $E_0 = 6.3 \times 10^{-5}$, thermocline scaling factor $b = 1300$m, modal scale number $j^* = 3$, $k_z* = \pi j^* \overline{N}/b/N_0$, and $N_0 = 5.2 \times 10^{-3}$ rad s^{-1}.

The strain variance, as used in the shear-to-strain ratio (3.7), is integrated over a variable wave number range to avoid noise contamination at high wave numbers. The shear spectrum on the contrary is integrated over a fixed wave number range. Since the integration ranges will in general differ we cannot simply use, $R =$

$\langle S[V_z/N] \rangle \,/\, \langle S[\xi_z] \rangle$, to calculate the shear-to-strain ratio. However, assuming that both the shear and the strain spectrum have Garrett-Munk-like shapes over their respective integration bands, we can calculate R by normalization with the GM variance,

$$R = 3 \frac{\left\langle S[\frac{V_z}{N}] / S_{GM}[\frac{V_z}{N}] \right\rangle}{\langle S[\xi_z] / S_{GM}[\xi_z] \rangle}, \tag{3.7}$$

where the factor 3 corrects for $\left\langle S_{GM}[\xi_z] / S_{GM}[\frac{V_z}{N}] \right\rangle \equiv 1/3$ when integrated over the same wave number band.

An alternative form of the above parameterization is based on strain only [Polzin, 1995; Mauritzen et al., 2002]. The global study of internal wave mixing by [Kunze et al., 2006] uses strain only in the deep ocean, where the quality of LADCP data usually deteriorates due to scarcity of acoustical scatterers. The strain only parameterization is similar in form to 3.3, but uses $S[\xi_z]$, instead of $S[V_z/N]$. Refraining from the use of shear variance means that the shear-to-strain ratio cannot be calculated. In the deep ocean [Kunze et al., 2006] use a fixed value of $R = 7$ and a modified scaling factor,

$$h_2 = \frac{1}{6\sqrt{2}} \frac{R(R+1)}{\sqrt{R-1}} = 2.7. \tag{3.8}$$

In section 3.4.2 we compare the shear-and-strain and strain only parameterization to show the effect of different model configurations.

3.2.2 Normalization of variance spectra

This section discusses how we calculate and normalize the shear and strain spectra. The Fourier transform is normalized to preserve variance when transforming from the spatial to the spectral domain.

The velocity signal and the strain signal are assumed to be given in equally spaced depth bins, $f(n)$,

with $n = 1, 2, 3, \ldots, N$ and spacing Δz. The data is segmented and detrended before Fourier transformation, $g(n) = w(n)f(n) - y(n)$, with $y(n)$ a linear fit to $w(n)f(n)$ and $w(n)$ a 10% $\sin^2$ 'window function'. The fast Fourier transform (FFT) algorithm works optimally for N a power of 2, and zeros are padded to the signal if necessary. The variance spectrum (S) is equal to the sum of the squared Fourier components and an appropriate normalization factor,

$$F_r(j) + F_i(j) = \sum_{n=1}^{N} g(n) e^{-ik_z(n-1)\Delta z}, \quad \text{with}$$
$$k_z = \frac{2\pi(j-1)}{N\Delta z}, \quad \text{and} \quad j = [1, 2, \ldots, N], \quad \text{and}$$
$$S[g](j) = 2\frac{\Delta z}{2\pi N}[F_r^2(j) + F_i^2(j)], \tag{3.9}$$

with $j = [2, 3, \ldots, N/2]$. The overall factor 2 comes from restricting the spectrum to the Nyquist range, $j = 1, \ldots, N/2 + 1$. The constant component with $j = 1$ and the Nyquist component with $j = N/2 + 1$ are unique and therefore *not* multiplied by 2.

The normalization is chosen so that the variance of the signal is equal to the integrated variance in the spectral domain. For a discrete signal we require $\mathrm{var}(g(n)) = 1/N \sum_{n=1}^{N} |g(n) - \overline{g(n)}|^2 = A \sum_{j=1}^{N} F(j)F^*(j)\Delta k_z$. Using that the mean of a detrended signal is zero, $\overline{g(n)} = 0$, and the Parseval theorem, $\sum_{n=1}^{N} |g(n)|^2 = 1/N \sum_{j=1}^{N} |F(j)|^2$, and writing $\Delta k_z = 2\pi/(\Delta z N)$, we obtain $A = \Delta z/(2\pi N)$.

3.2.3 Spectral corrections

Spectral corrections account for the loss of variance due to non-continuous data and instrument limitations. The strain spectrum $S[\xi_z]$ is only corrected for bin-to-bin first differencing and the correction factor

is $\mathrm{sinc}^2(\Delta z k_z/2\pi)$ for bin-size Δz. The shear variance spectrum is corrected for loss of variance due to, (i) range averaging, (ii) finite differencing, (iii) interpolation, and (iv) instrument tilting, by the following spectral functions:

$$S_1 = \mathrm{sinc}(k_z \Delta z_t/(2\pi))^2 \times \mathrm{sinc}(k_z \Delta z_r/(2\pi))^2, \quad (3.10)$$

$$S_2 = \mathrm{sinc}(k_z \Delta z/(2\pi))^2, \quad (3.11)$$

$$S_3 = \mathrm{sinc}(k_z \Delta z_r/(2\pi))^4 \times \mathrm{sinc}(k_z \Delta z/(2\pi))^2 \quad (3.12)$$

$$S_4 = \mathrm{sinc}(k_z \overline{d}/(2\pi))^2, \quad (3.13)$$

with Δz_t the LADCP transmitter vertical pulse length (typically 16m), Δz_r the LADCP receiver processing bin length (typically 16m), Δz data bin size (typically 20m), and $\overline{d} = 9$m determined empirically [Polzin et al., 2002].

3.2.4 Buoyancy frequency and strain

The buoyancy frequency, N, is an important ingredient of the fine scale parameterization. In this section we show how we calculate N and we discuss some of the potential issues we encountered when the deep ocean becomes weakly density stratified.

The mean buoyancy frequency can be calculated in different ways. We chose to calculate the mean buoyancy frequency $\langle N^2 \rangle$ in the strain expression using a second order least-square fit to N^2 over the length of each segment (320m), instead of the physically more elegant method of adiabatic levelling [Bray and Fofonoff, 1981]. The motivation for this simplification is the significantly lower computational cost (O(100) times faster) and the fact that we observe a low impact on the dissipation estimates.

The dissipation parameterization depends on strain through the integrated strain variance in the shear/strain

ratio. Figure 3.1 compares strain variance obtained from a simple quadratic fit to N^2 and adiabatic levelling. The agreement of both estimates is reasonable throughout the water column, which we observe similarly for other hydrographic stations. Moreover it should be noted that the shear/strain parameterization depends only weakly on strain variance.

There is however one point of concern when using a simple fit to estimate the mean buoyancy frequency. It works fine for estimating the deviation from the mean state in the numerator of the strain expression, but cannot be used for the denominator, as $\langle N^2 \rangle$ may be zero. Negative $\langle N^2 \rangle$ (and therefore zero-crossings) occur because there are negative N^2 values, mostly due to noise in temperature and salinity measurements and perhaps also due to real density overturns. The simplest way to suppress noise is averaging and we chose to use the segment mean $\overline{N^2}$, so that $\xi_z = (N^2(z) - < N^2(z) >)/\overline{N^2}$.

One more point of caution is the risk of $\overline{N^2}$ becoming prohibitively small, that is indistinguishable from zero. Monte Carlo simulations with WOCE standard errors of 0.001°C for temperature and 0.003 for salinity gives a standard error of 2×10^{-10} rad s^{-1} for the segment mean buoyancy frequency $\overline{N^2}$. We use this value as a lower bound for $\overline{N^2}$ and discard segments with a smaller mean buoyancy frequency.

3.2.5 Shear-to-strain ratio

The shear-to-strain ratio is related to the dominant frequency of a broadband internal wave field, because,

$$R = \frac{(\omega^2 + f^2)(N^2 - \omega^2)}{N^2(\omega^2 - f^2)}, \tag{3.14}$$

for a single, linear wave [Polzin, 1995]. Linear wave theory also predicts that the interaction rate of single

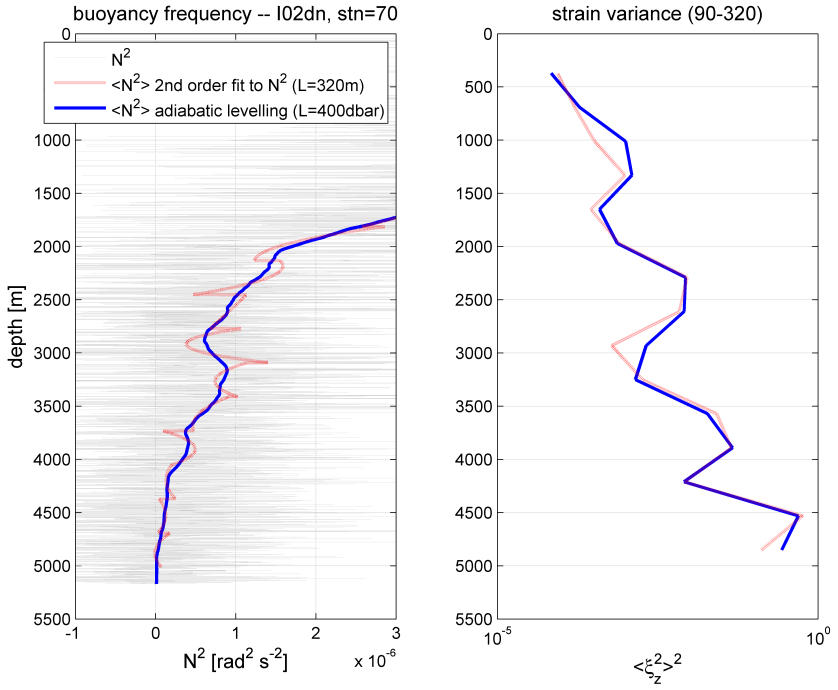

Figure 3.1: Buoyancy frequency and strain. Left: Comparison of the mean buoyancy frequency from a 2nd order fit $\langle N^2 \rangle_{simple}$ and from adiabatic levelling $\langle N^2 \rangle_{adia}$. The buoyancy frequency is calculated by first differencing of 2m density bins. Right: Comparison of strain variance calculated using $\langle N^2 \rangle_{simple}$ and $\langle N^2 \rangle_{adia}$.

model feature	configuration
data segments	bottom-up and 320m long
Fourier window	10% $\sin^2$
buoyancy frequency	$\overline{N^2} > f$ and $\overline{N^2} > 8 \times 10^{-8}$ rad s^{-1}
shear integration limits	150–320m
strain integration limits	λ_0–150m, where λ_0 = 10m or the shortest wavelength for which $\int_{\lambda_0}^{150m} S[\xi_z](\lambda)\, d\lambda \leq 0.1$.
shear-to-strain ratio	minimum value set to $R = 1.01$ as in [Kunze et al., 2002]; and we use $R = 7$ if only strain is available or when strain is too noisy.

Table 3.1: Model configuration

wave with a background wave field is proportional to,

$$\left[\frac{(\omega^2 - f^2)}{(N^2 - \omega^2)}\right]^{1/2}. \tag{3.15}$$

Combining these relations gives an estimate of the expected interaction rate in terms of R, which can be used to improve the HWF-scaling in non-GM conditions [Polzin, 1995]. We use the $\omega \ll N$ approximation of the shear-to-strain scaling factor $h_1(R)$, refer to (3.4), as in [Kunze et al., 2006]. Note that this factor is 1 for a GM wave field, because $R_{GM} = 3$.

3.2.6 Summary of model configuration

The main features of our model configuration are summarized in Table 3.1. The criterion for the integration range of strain variance, as well as the choice of the shear integration bandwidth is taken from [Kunze et al., 2006]. The use of different integration ranges aims to avoid small scales where LADCP data become noisy and large scales where strain variance is less likely to originate from internal waves.

With regard to the buoyancy frequency and the calculation of strain we choose a relatively straightforward approach (refer to Section 3.2.4). The buoyancy

frequency $N(z)$ is calculated using `sw_bfrq`, a routine in CSIRO SEAWATER library for MATLAB[1]. The 'background' mean buoyancy frequency is calculated by a simple quadratic fit to $N(z)$ within a segment, instead of using the more elaborate method of adiabatic levelling [Bray and Fofonoff, 1981] as was preferred by [Polzin, 1995], [Naveira-Garabato et al., 2004b], and [Naveira-Garabato et al., 2004a].

Another omitted configuration option is averaging shear and strain variance over several segments at the same depth from neighbouring hydrographic stations. Averaging of spectra reduces the statistical uncertainty. Instead of spectral averaging over segments at the same depth we choose to average over segments at the same density.

3.3 Data

The fine scale parameterization for turbulent dissipation or diffusivity requires information about the density gradient and the vertical variance of the horizontal flow velocity. This information can be collected through simultaneous CTD and LADCP profiling. The required CTD quality standard and the need for LADCP measurements limits the available data sets to the WOCE and post-WOCE era. Table 3.2 gives an overview of the data sets used in this study and Fig. 3.2 shows the locations of the measurements.

A reformulation of the G89 parameterization in terms of strain variance instead of shear variance makes it possible to infer mixing from CTD data only. The validity of this method is less established, and appears to underestimate the dissipation rate below 3000m (refer to Section 3.4.2). Nevertheless we added a number of CTD only hydrographic casts to our analysis (again

[1] http://www.cmar.csiro.au/datacentre/ext_docs/seawater.htm

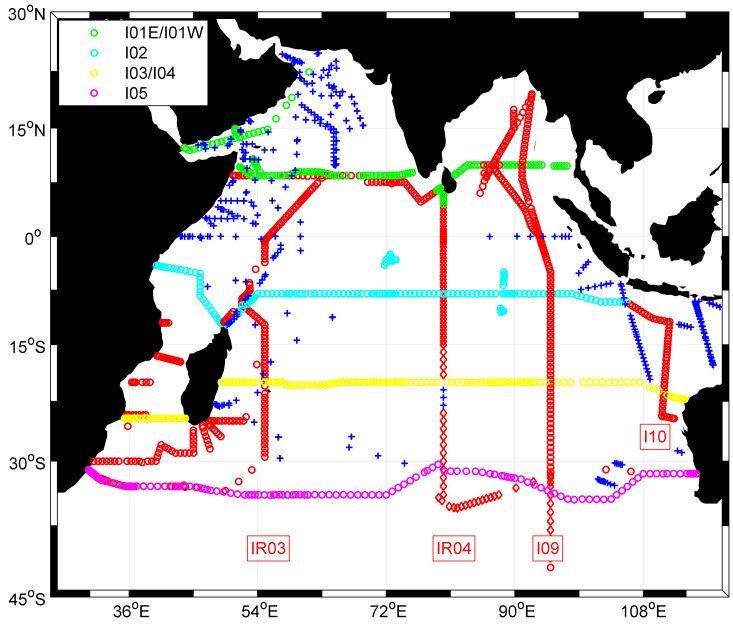

Figure 3.2: Locations of hydrographic stations used for the estimation of turbulent dissipation. Open circles/diamonds indicate depth profiles with CTD and LADCP data and the plus signs mark the locations of CTD only measurements.

refer to Table 3.2) to improve the spatial coverage. The total number of CTD and LADCP casts used in this study is 1545 plus 453 CTD only casts. For some hydrographic sections we have access to both down-cast LADCP data and the mean of the up– and the down-cast. These sections are marked with an asterisk in Table 3.2.

3.4 Results

3.4.1 Shear and strain spectra

The methods discussed in this chapter rely critically on our ability to estimate the energy density of the internal wave field. Estimation of the energy content

no.	dataset	chief scientist	year/month	Δz	# casts
1	I09N*	A.L. Gordon	1995/1	20.0	129
2	ISS01/10*	H.L. Bryden	1995/2	20.0	15
3	IR03	A. Ffield	1995/3	10.0	114
4	IR01W	R. Molinari	1995/5	10.0	93
5	I4-I5W-I7C*	J. Toole	1995/6	20.0	134
6	I01W	J.M. Morrison	1995/8	20.0	105
7	I01E	H.L. Bryden	1995/9	20.0	53
8	IR04	R. Molinari	1995/9	10.0	92
9	I10	N. Bray	1995/11	20.0	61
10	I02*	B. Warren	1995/12	20.0	168
11	ACSEX1	H. Ridderinkhof	2000/3	19.5	55
12	ACSEX2	H.M. van Aken	2001/3	19.4	63
13	ACSEX3	H. Ridderinkhof	2001/3	19.6	79
14	I05	H.L. Bryden	2002/3	19.5	133
15	I03/I04	M. Fukasawa	2003/12	20.0	141
16	I09N_2007	J. Sprintall	2007/3	8.4	110
I	nioz	–	–	–	80
II	sismer	–	–	–	196
III	nodc	–	–	–	177

Table 3.2: Hydrographic sections used for estimation of turbulent dissipation. The LADCP bin size is given in the Δz column and the asterisk means that both up– and mean cast data are available. All sections prior to 1998 are part of the World Ocean Circulation Experiment (WOCE) and later sections fall under the Climate Variability and Predictability (CLIVAR) program, except for the ACSEX series, which was organised and funded by the Netherlands Institute for Sea Research (NIOZ). The data sets I, II and III contain additional CTD-only profiles from NIOZ, Systèmes d'Informations Scientifiques pour la Mer (SISMER), and the United States National Oceanographic Data Center (NODC).

is commonly done in spectral space, using spectral filtering to discriminate between internal wave motions and other motions, where the latter are referred to as 'noise'. Noise characteristics of shear and strain differ because of differences in the spatial sampling frequency (typically 20m for shear and 2m for strain) and instrument differences (LADCP for shear and CTD for strain measurement) [Polzin et al., 2002].

The spectra shown in Fig. 3.3 represent the median spectral level in the proximity of a given density level. Both the spectral variance of vertical shear normalized by buoyancy frequency and the spectral variance of strain are shown. These spectra are calculated as discussed in Section 3.2.2 and corrected for finite differencing and smoothing (refer to Section 3.2.3).

It is obvious from Fig. 3.3 that the observed spectra are not strikingly GM-like. Similarity to the GM-spectrum generally deteriorates towards the lowest density levels and is generally not convincing for the shear spectra. Strain spectra are often GM-like, that is flat, within the integration limits, but the shear spectra have steeper slopes. The 'blueness' of the shear spectra gives us the impression that the loss of variance is over-compensated when we apply spectral corrections (3.10)–(3.13).

3.4.2 Comparison of shear and strain variance

Both shear variance and strain variance have been used in various studies to infer the energy density of the internal wave field, see [Gregg, 1989] and [Kunze et al., 1990] for some pioneering studies. In this section we explore the relation between shear and strain in our observations.

Figure 3.4 shows the quantile–quantile plots of the logarithm of the shear spectral level versus the loga-

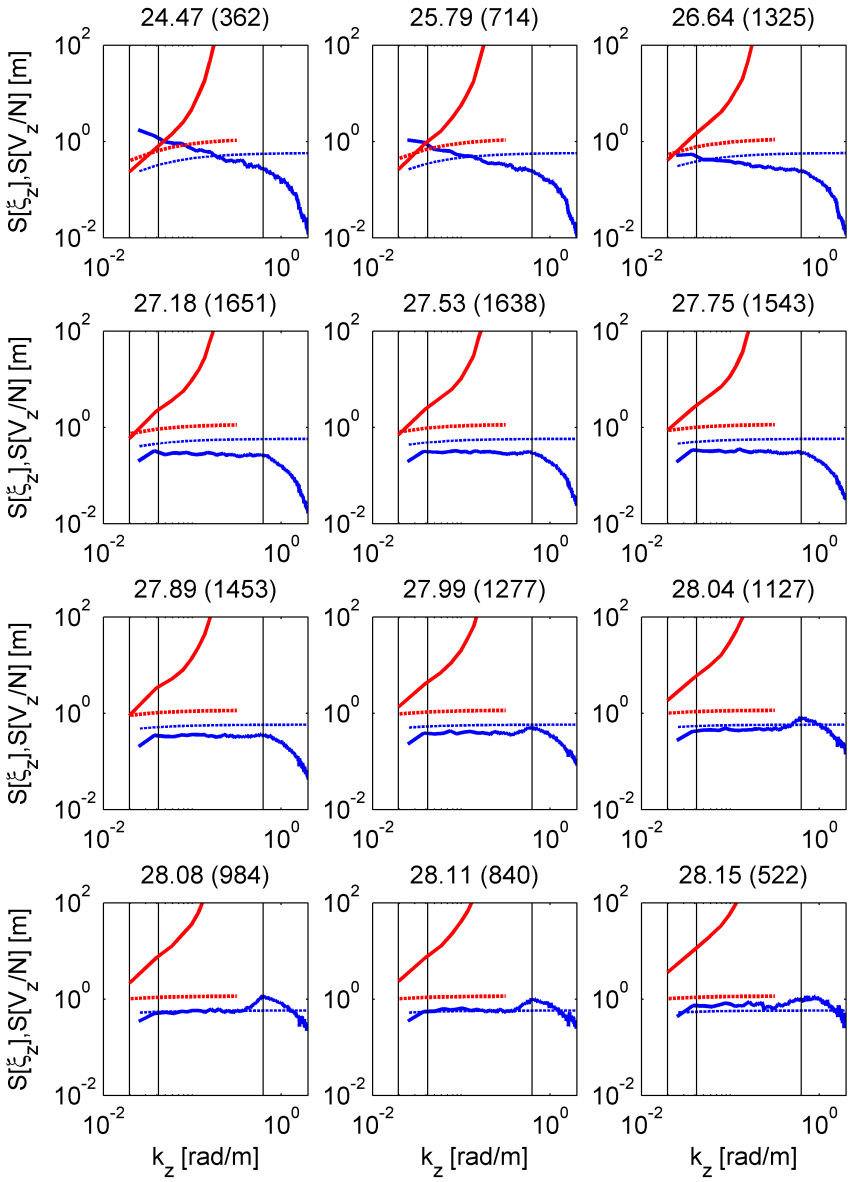

Figure 3.3: Median level of shear (red) and strain (blue) variance at given density. Dotted spectra indicate the GM spectral levels. Vertical lines correspond to wavelengths of 320, 150 and 10m (from left to right). The number between brackets is the number of spectral estimates at the given density level.

rithm of the strain spectral level for all such estimates available at a given density. The spectral level is the spectrum integrated over a given wave band normalized by the GM-spectrum integrated over the same wave band. The integration wavelengths are typically 150–320m for shear and 10–150m for strain (refer to Table 3.1 for details). The integrated quantity expresses the energy density of the internal wave field in units of GM energy density.

The quantile–quantile plots give us information on how the distributions differ. Focussing on density levels denser than 26.64 we can make a few general observations: (i) There is a shift in location, and strain generally becomes smaller at higher densities; (ii) The plots are somewhat S-shaped, which means that the shear distribution has heavier tails and/or strain is truncated; (iii) The quantiles are quasi-linear within the interquartile range, indicating similar distributional shapes within this range; (iv) The slope of the line connecting the first and the third quartile is generally slightly less than 45°, indicating a different scaling, with shear being more dispersed than strain.

A comparison of shear-and-strain dissipation estimates and strain-only dissipation estimates is shown in Figures 3.5 and 3.14. Figure 3.5 is a scatter plot of strain only versus shear-and-strain at different density levels. Figure 3.14 displays the depth-mean dissipation profile for section I02 and shows that, below 3000m, strain-only estimates are up to 2 orders of magnitude smaller than shear-and-strain estimates.

The shear-to-strain ratio is used to estimate the dominant frequency of the internal wave field (refer to Section 3.2.5). Figure 3.6 displays the shear-to-strain ratio versus the GM-normalized shear variance at different density levels. Noisy strain estimates are avoided by omitting $R \leq 1.01$, the 'hard-coded' lower

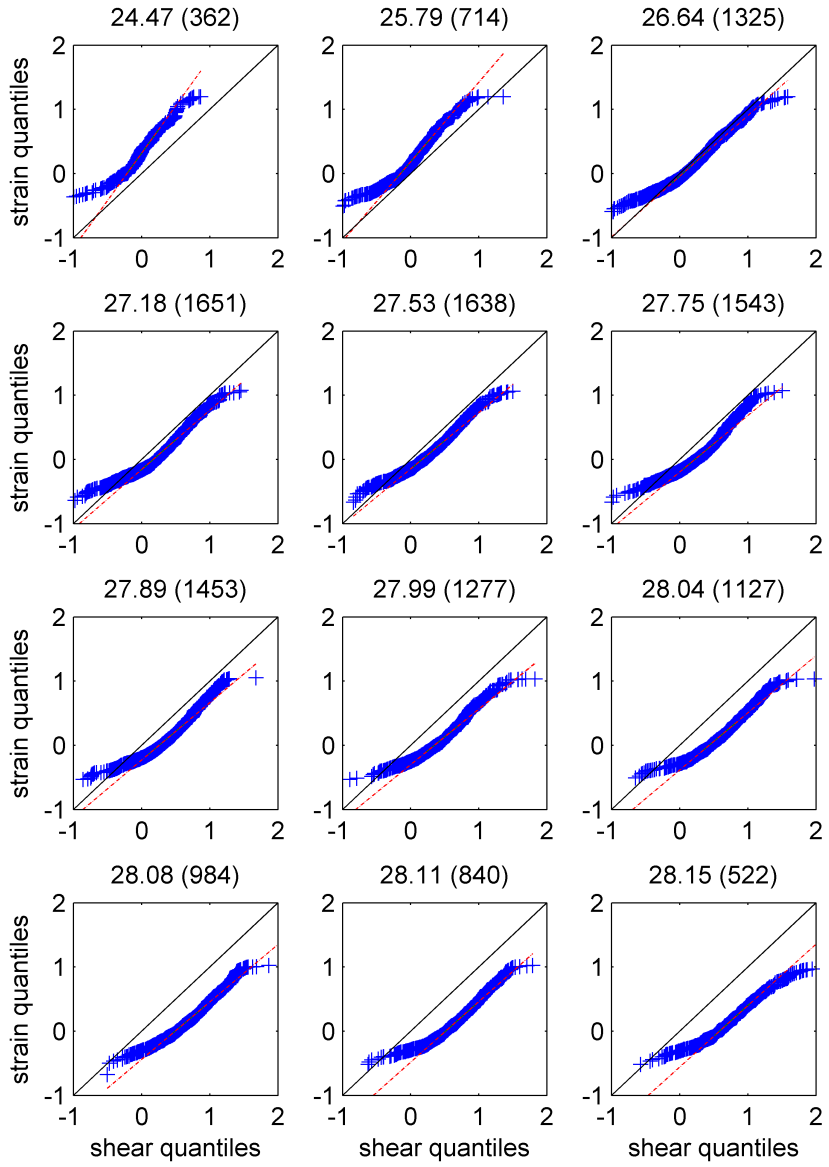

Figure 3.4: Quantile–quantile plots of the logarithm of the shear spectral level versus the logarithm of the strain spectral level at different density levels. Both the shear and the strain spectra are normalized by their respective GM spectral values. The red dashed line joins the first and third quartiles of each distribution.

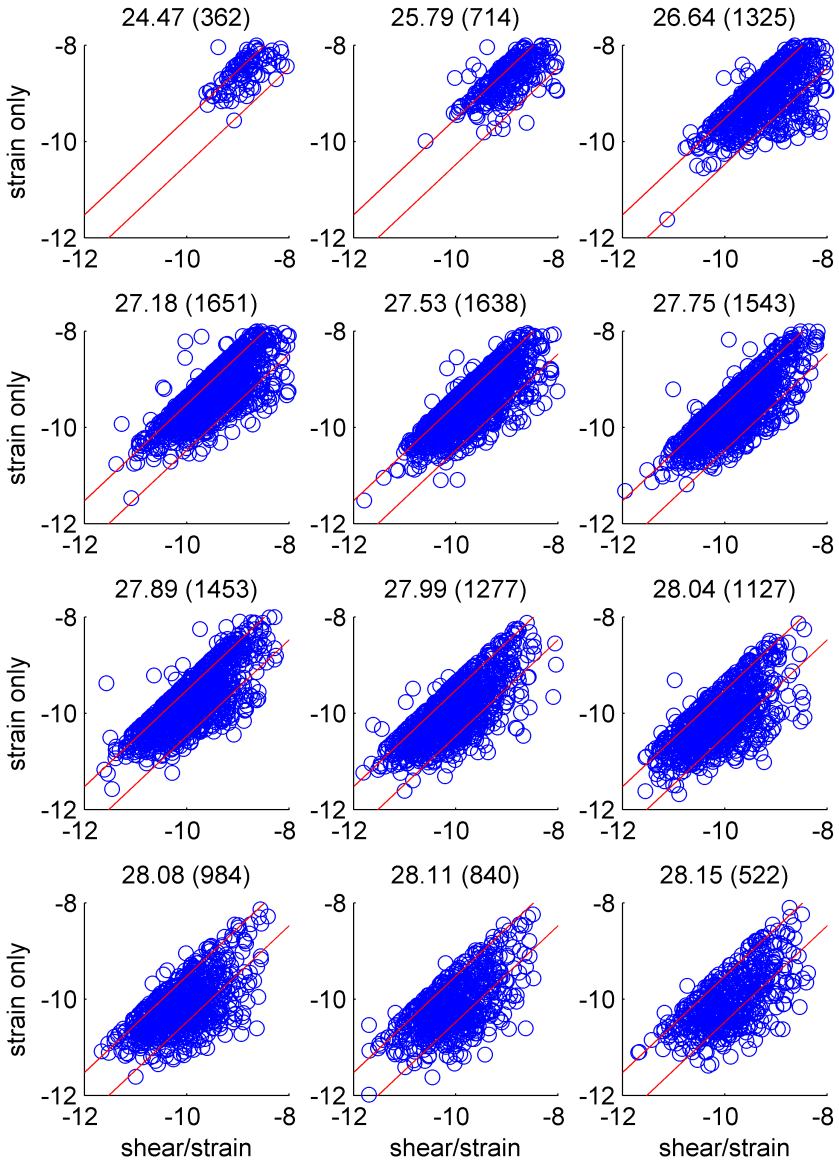

Figure 3.5: Scatter plots of the logarithm of shear-and-strain dissipation estimates (horizontal axis) versus the logarithm of strain only dissipation estimates (vertical axis). The red lines indicate the range of factor three difference.

limit, and $R = 7$, the value we use when the integrated strain exceeds 0.1 when integrated over the lowest two wave numbers. The plots show a positive correlation, that is larger shear-to-strain ratios for higher shear levels, which implies that strain does not scale proportionally to shear. The shift towards larger R also implies a shift towards lower, more inertial frequencies.

In Fig. 3.6 we also address the question whether $R = 7$ is a good choice for the deep ocean, when shear is not available. Each plot gives the median shear-to-strain ratio, $< R >$, and we see that $< R >$ increases towards higher density levels, from $< R >= 2.5$ at $\gamma = 24.47$, to $< R >= 8.4$ at $\gamma = 28.15$.

We find that shear-to-strain ratios are even higher for $N > N_{err} = 4.5 \times 10^{-4}$ rad s^{-1} and have a median value of 19. This suggests that the canonical value of $R = 7$ for $N < N_{err}$, as used by [Kunze et al., 2006], is on the low side. Choosing $R = 19$, instead of $R = 7$, would increase the [Kunze et al., 2006] strain-only dissipation estimates, for $N < N_{err}$, by a factor of 3.9 (refer to Fig. 3.7).

3.4.3 ADCP noise

This section discusses ADCP noise in relation to concerns raised by [Kunze et al., 2006] about the quality of shear estimates in the deep ocean. The typical accuracy of a single-ping ADCP velocity estimate is, $\Delta v = 3.2 \times 10^{-2}$ ms^{-1}. Averaging will reduce the standard deviation of the velocity error by the square root of the number of pings if the ping-to-ping error is uncorrelated. The noise spectrum for $u^2 + v^2$ is 'white' and given by,

$$S[V] = \frac{2\,\Delta v^2\,\Delta z_t}{\pi N_p}, \tag{3.16}$$

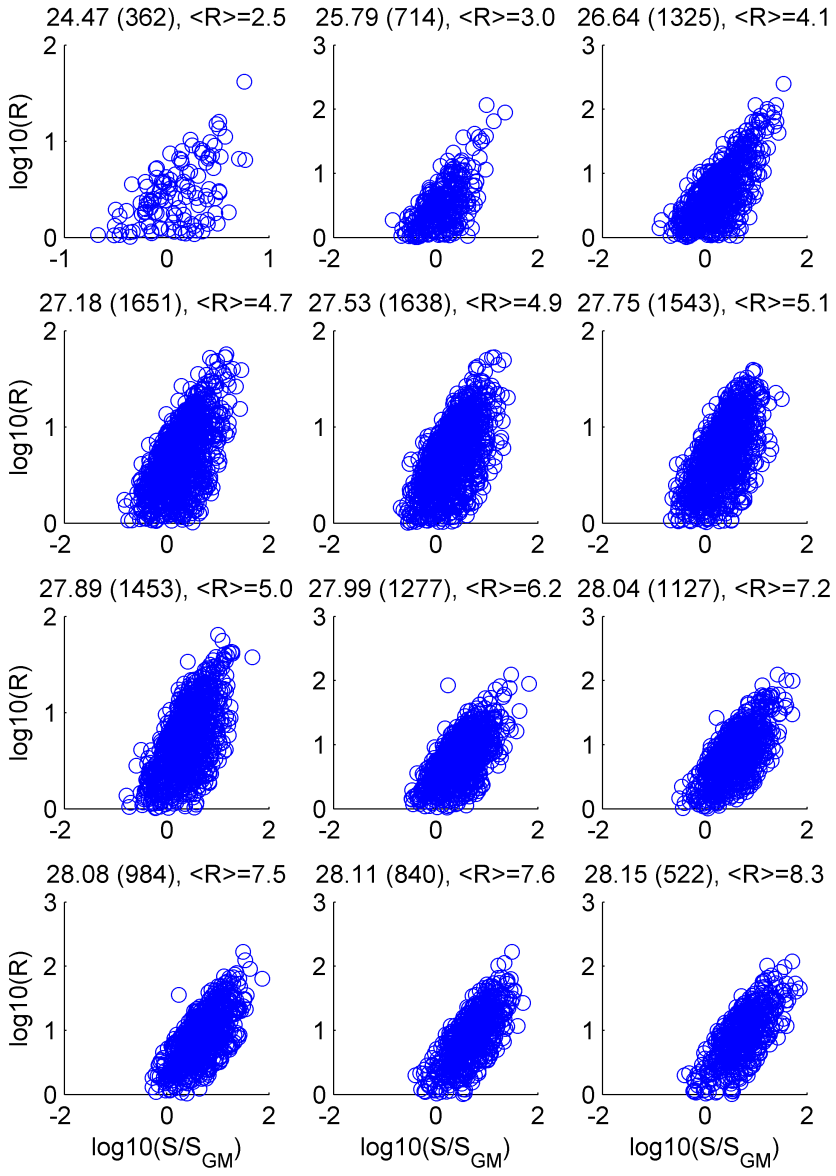

Figure 3.6: Shear-to-strain ratio versus GM-normalized shear variance. Note that we have excluded $R \leq 1.01$ and $R = 7$ from the ensemble and that $< R >$ denotes the median value.

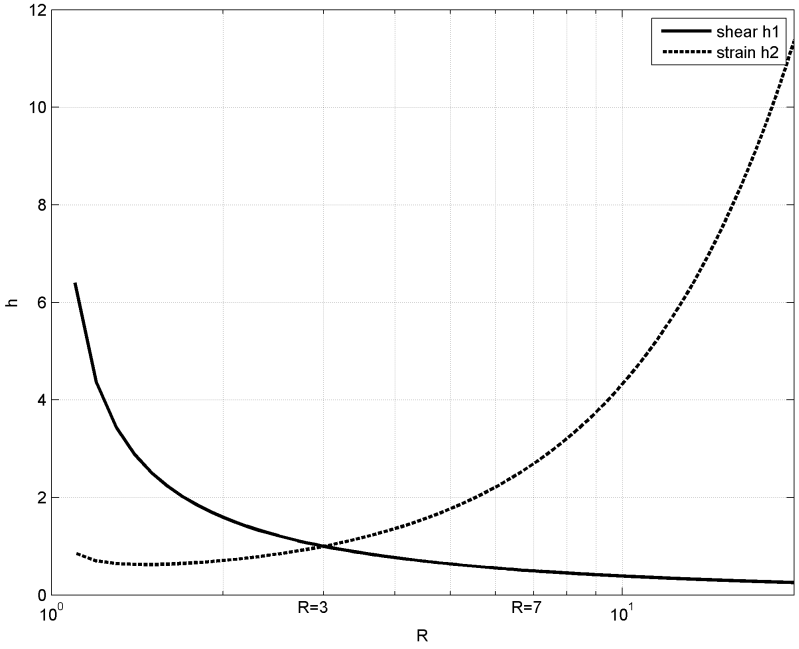

Figure 3.7: Shear-to-strain dependence, $h_1(R)$ (3.4) in the shear-based parameterization (3.3), and $h_2(R)$ (3.8) in strain-only parameterization.

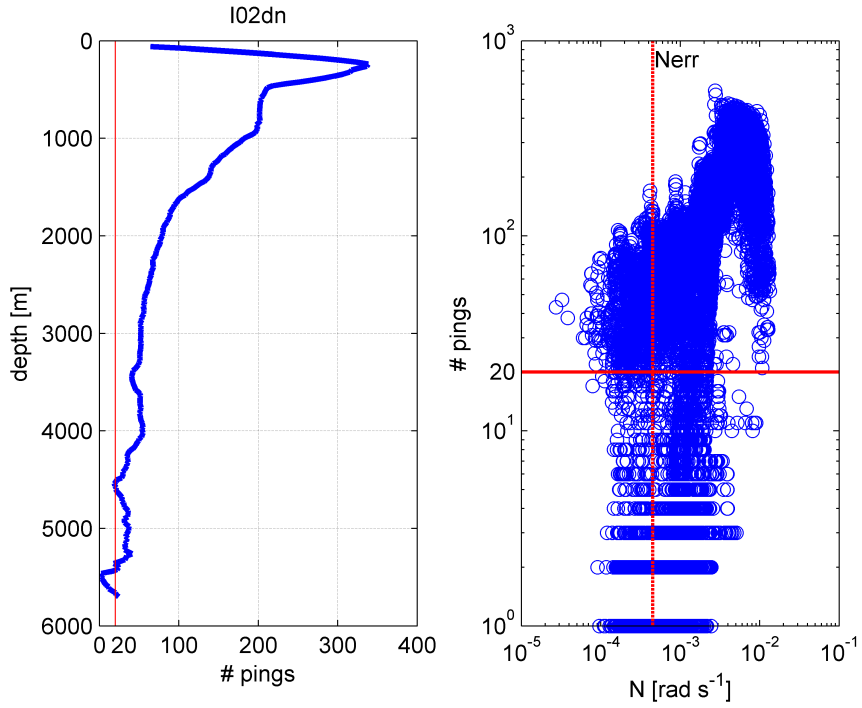

Figure 3.8: Number of acoustical pings going into a LADCP bin-average for the I02 section. Left: average number of pings for each depth level. Right: number of pings (vertical axis) versus bin-averaged buoyancy frequency (horizontal axis).

with N_p the number of pings, and Δz_t the transmitted sound pulse length projected on the vertical. The vertical shear spectrum is obtained by multiplying (3.16) by the vertical wave number k_z, that is,

$$S[V_z] = k_z S[V]. \tag{3.17}$$

The number of pings going into an ensemble average depends on the presence of small scale suspended matter, capable of refracting the sound signal. The abundance of acoustical scatterers in the ocean typically decreases towards the bottom, as the left panel of Fig. 3.8 shows.

The choice to discard shear estimates at low stratification, as preferred by [Kunze et al., 2006], is based

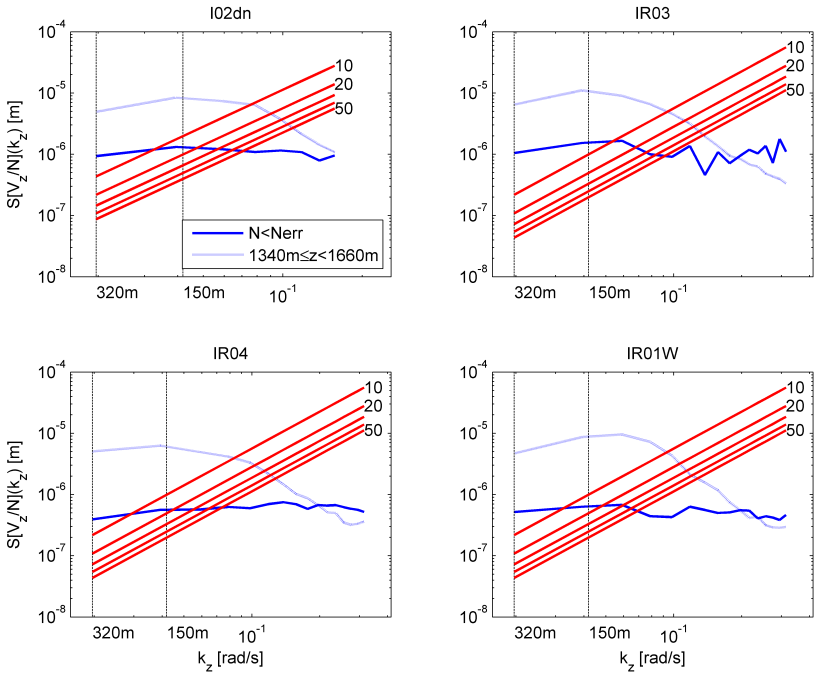

Figure 3.9: Observed vertical shear variance at section I02 and estimated ADCP noise spectra. The blue solid line is the mean spectrum for data segments at low stratification, with $N < N_{err}$, and the blue dotted line is based on data in the depth range from 1340m to 1660m. The red lines are estimated ADCP noise levels for different number of pings. The number of pings going into a velocity estimate determines its accuracy and depends on the local abundance of acoustical scatterers.

on concerns about scatterers. In Fig. 3.9 we compare the observed shear variance at section I02 with the estimated ADCP noise spectrum (3.17). The figure shows that the expected noise spectrum may indeed exceed the observed spectrum in the deep ocean where $N < N_{err}$, if less than 20 pings are available for averaging.

The right panel of Fig. 3.8 however shows that there is no clear correlation between the number of pings and the stratification. For section I02 we find LADCP bins with less than 20 pings for a large range of buoyancy frequencies, between 7×10^{-5} and 1×10^{-2}

rad s^{-1}. We note that the vast majority of the 'low ping' bins has a mean buoyancy frequency larger than $N_{err} = 4.5 \times 10^{-4}$ rad s^{-1} and that most LADCP bins with $N < N_{err}$ are averaged over more than 20 bins. This leads us to conclude that the [Kunze et al., 2006] criterion to select 'bad' LADCP bins with insufficient pings is unfit. For this reason, and because we do not have information on the number of pings for most hydrographic sections, we choose to use shear throughout the water column.

3.4.4 Inferred dissipation patterns

Internal waves are omnipresent in the ocean, but not uniformly distributed as for example the Garrett-Munk model assumes. Although the internal wave field indeed tends to relax to a steady state that is adequately described by the GM model, there is still plenty of reason to expect spatial and temporal variability, because both forcing (mostly tides and wind) and sinks (mean flow and topography) are non-uniform and non-stationary. For example over the past 15 years it has been demonstrated that steep topographic features lead to intensified internal wave breaking and turbulent dissipation [Ferron et al., 1998; Ledwell et al., 2000; Mauritzen et al., 2002].

Figure 3.10 shows the dissipation profile inferred from the main zonal hydrographic sections in the Indian Ocean. The main topographic features of interest in the Indian Ocean are the Southwest Indian Ridge (SWIR), the Central Indian Ridge (CIR) and the Ninetyeast Ridge (NER). These features are labelled in the figure and all sections show elevated dissipation rates above the SWIR and the CIR, but not above the NER. Other locations of elevated dissipation are the Andaman-Nicobar Ridge (refer to hydrographic section I01E), off the continental shelf, and near islands

and seamounts. In particular Madagascar (I02) and Mauritius (I03/I04) appear to radiate internal wave beams. Similar features are visible off the west flank of Mozambique Plateau and Madagascar Ridge. There is also elevated dissipation between the plateau and the ridge, which perhaps could be explained by wave trapping [Maas et al., 1997].

The meridional sections displayed in Figure 3.11 show fewer dissipation features and also less obvious correlation to the bottom topography. The Seychelles in section I07 is perhaps an exception to this general observation. The most clear pattern in the meridional sections is the east–west divide, with generally higher dissipation rates in the west. Again, one could argue that this is correlated to the more abundant and steeper topography in the western part of the basin. Indeed, the Ganges sediment cone supports the general notion that weak mixing is to be expected above smooth topography.

3.4.5 Comparison with previously published estimates

This section discusses a discrepancy between dissipation estimates by Kunze et al. at the University of Victoria (UVic) and Naveira-Garabato at al. the National Oceanography Centre, Southampton (NOCS). Andreas Thurnherr (personal communication) compared the depth mean dissipation rate for section I02 as estimated by [Kunze et al., 2006] with estimates by [Palmer et al., 2007] (refer to their Fig. 2) and noticed a difference of about one order of magnitude in the upper 4000m and several orders of magnitude below that depth. This difference is disconcertingly large because both authors used an incarnation of the G03 parameterization [Gregg et al., 2003]. Hereafter we will refer to the [Kunze et al., 2006] dissipation

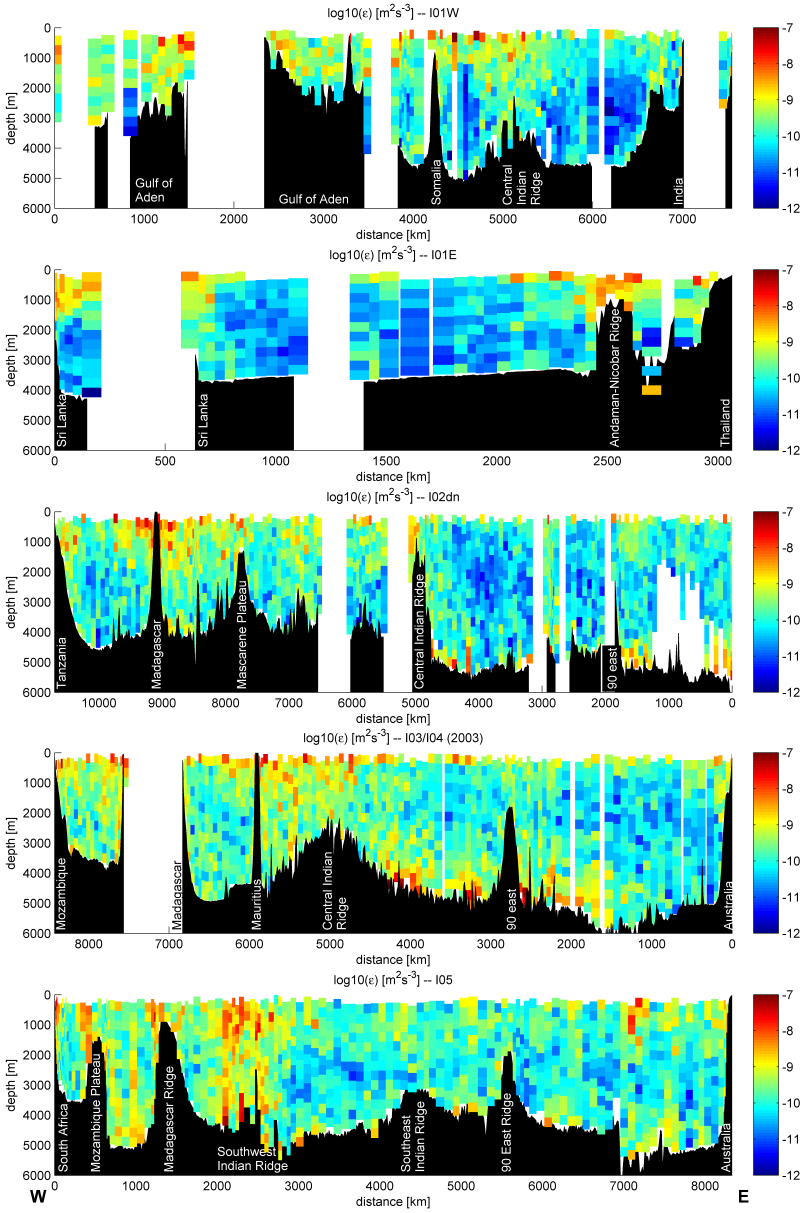

Figure 3.10: Dissipation estimates for zonal sections. The color scale is logarithmic. White spaces indicate missing data or noisy data.

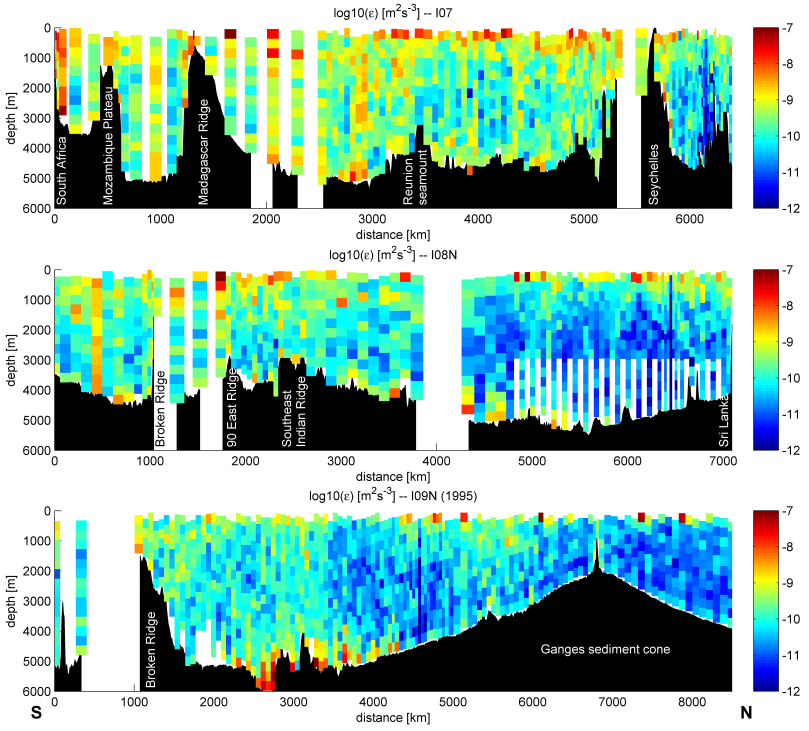

Figure 3.11: Dissipation estimates for meridional sections. The color scale is logarithmic. White spaces indicate missing or noisy data.

estimates as 'UVic' and to the [Palmer et al., 2007] estimates as 'NOCSvI'.

The diffusivity estimates by UVic and NOCS for section I02dn are shown in Fig. 3.12, where 'dn' stands for downcast. We use the downcast because strain from upcasts is often contaminated by the CTD wake. The color coding in the figure is the same used by [Kunze et al., 2006] for easy comparison with their Fig. 6. The reproduced NOCSvI estimates are almost identical to the results published by [Palmer et al., 2007] and the NOCSvII parameterization is based on [Kunze et al., 2006], and has the form of (3.3). The colored diffusivity patterns clearly show the discrepancy between NOCSvI and UVic as pointed out by A. Thurnherr.

To allow for comparison with the large scale dissipation estimates obtained in Chapter 2 we have converted the previously published diffusivity estimates to dissipation rates using the Osborn relation [Osborn, 1980]. NOCSvI and UVic dissipation rates and buoyancy frequencies are plotted against each other in Fig. 3.13. The comparison of buoyancy frequencies is reassuring in the sense that it gives a tight one-to-one relation. The dissipation rates however scatter over multiple orders of magnitude. The NOCSvI estimates are biased high compared to the UVic estimates, especially towards the bottom. The different scaling with depth becomes very pronounced below 3000 m, where NOCSvI estimates increase over 2 orders of magnitude, whereas the UVic dissipation rates remain more or less constant.

The NOCSvII parameterization is the result of an attempt to reproduce the UVic results by rebuilding the model from scratch following [Kunze et al., 2006] and guidelines personally communicated by E. Kunze. The most distinct feature of the UVic parameteriza-

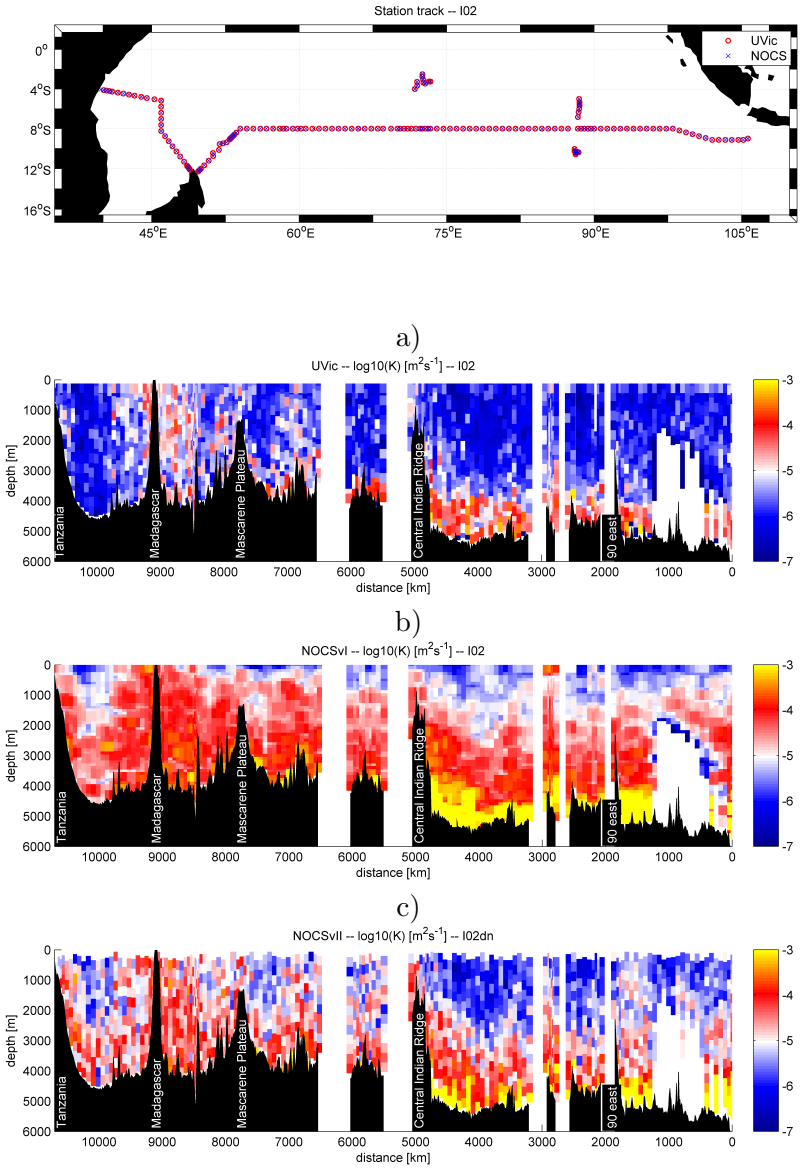

Figure 3.12: Comparison of UVic and NOCS diffusivity estimates based on the Dec 1995 to Jan 1996 WOCE occupation of the I02 hydrographic section. Top: station positions. (a) UVic estimates [Kunze et al., 2006]. (b) NOCSvI estimates [Palmer et al., 2007]. (c) New NOCSvII estimates.

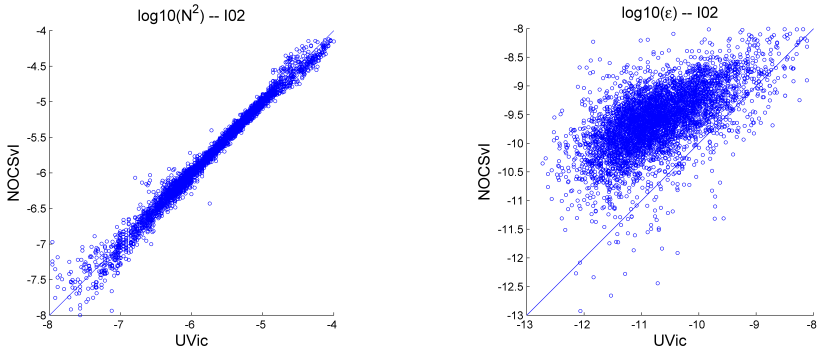

Figure 3.13: Comparison of UVic and NOCSvI. Left: comparison of 320m segment mean buoyancy frequency. Right: comparison of dissipation estimates for the same segments. Both scatter plots compare data with a difference in position of less than one second and segments depths differ by at most 80m (the segment overlap will not be perfect as UVic segments go bottom-up and NOCSvI goes top-down).

tion, that is the use of only strain at low stratification, is not incorporated in NOCSvII, but has been evaluated in model test runs. Other features, that have been incorporated, and differ from NOCSvI include different integration bandwidths for shear and strain, and the use of the shear-to-strain ratio. The configuration of the NOCSvII model is summarized in Table 3.1.

The new result is presented in Fig. 3.14, where the NOCSvII depth mean dissipation rate is compared to UVic and NOCSvI. We see that the new NOCSvII estimates agree with the NOCSvI estimates to within a factor of 3, except in the bottom bin where the old NOCSvI estimates are about an order of magnitude larger. This result means that the discrepancy with the UVic estimates remains unresolved. In test runs we found that the new estimates converge towards the UVic values if we use strain-only when $N > N_{err}$, but we have not been able to reproduce the shear based estimates.

Both NOCSvI and NOCSvII give dissipation esti-

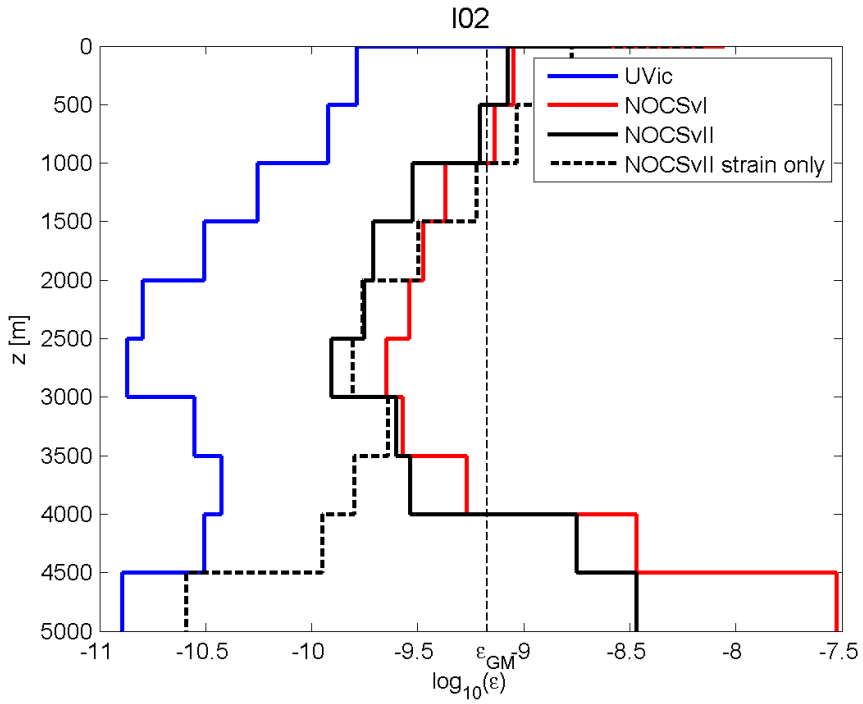

Figure 3.14: Depth mean dissipation rates in 500m bins.

mates that are about one order of magnitude larger than the UVic estimates. The fact that both NOCS models were independently developed, and the fact that the NOCS estimates are of the same order of magnitude as the dissipation rate predicted by the GM model, give us reasons to believe that UVic systematically underestimates the dissipation.

3.5 Discussion

Two decades of fine scale parameterization of ocean turbulence have resulted in a recipe that still appears to require substantial 'cooking skills'. In this section we discuss some of the applicability limitations discussed in the literature and the issues we encountered ourselves.

Extensions to the original G89 parameterization

have improved its performance in non-GM conditions [Polzin, 1995; Gregg et al., 2003], but have not resulted in a foolproof recipe that works anywhere, anytime, because the physics incorporated in the model remains limited. Several studies have explored the break-down point, for example, (i) [Kunze et al., 2002] report factor 30 underestimation of dissipation in Monterrey Canyon, (ii) [Finnigan et al., 2002] find that strain variance underestimates mixing in regions of weak stratification compared to mixing estimates based on Thorpe scale analysis and budget methods, and (iii) [MacKinnon and Gregg, 2003] conclude that the Gregg–Henyey scaling fails on the continental shelf.

However, at many other sites the method has proven to be accurate to within a factor 2–3 compared to micro-structure measurements, e.g. [Polzin, 1995]. This makes the method a powerful tool to reveal mixing patterns, as demonstrated by [Naveira-Garabato et al., 2004a,b; Kunze et al., 2006].

The main issue discussed in this chapter is the discrepancy between published diffusivity estimates for the I02 section in the Indian Ocean by [Kunze et al., 2006] and [Palmer et al., 2007]. It is a case of: same method, same data, different answer. And the difference is much larger than the widely reported accuracy of factor 2–3.

This disconcerting discrepancy has motivated our attempt to reproduce the [Kunze et al., 2006] result, first by iterative modification of our existing routine, and later by totally rebuilding of the code from scratch. This effort has increased our appreciation of some flavour differences, such as different ways of dealing with noise at low stratification. Every flavour has its own bias and we conclude that the different scaling behaviour in the deep ocean appears to be attributable to the use of strain variance instead of shear variance as preferred

by [Kunze et al., 2006]. We found that using strain variance, limited to an integrated value of 0.1, produces much lower mean dissipation rates below 3500m, compared to estimates based on shear variance.

We do not share concerns expressed by [Kunze et al., 2006] about excessive noise contamination of the LADCP data at low N and therefore chose to use shear variance throughout the water column. On the contrary, we find that the buoyancy frequency, and thus also strain, may be seriously affected by noise at low stratification. To us, it appears that strain in weakly stratified waters may be more affected by noise than shear.

The NOCSvII model configuration, as used in this study, is preferred over the NOCSvI model, as used by [Palmer et al., 2007], for the following reasons:

1. NOCSvI does not use the shear-to-strain ratio,
2. NOCSvI segments the data starting at the surface, whereas NOCSvII segments start at the bottom, which ensures optimal use of the bottom data,
3. NOCSvI uses variable shear integration limits based on the number of ADCP pings going into a data bin, this information however is often not available and therefore not used in NOCSvII.

3.6 Summary and conclusion

In this chapter we discussed the details of the parameterization we used to infer dissipation from fine scale vertical shear and strain.

A comparison with previously published estimates by [Kunze et al., 2006] and [Palmer et al., 2007] shows that we reproduce the latter to within the uncertainty of the method, except in the bottom 500m, where our estimates are about one order of magnitude smaller, due to segmenting from bottom and the use of the shear-to-strain ratio. The [Kunze et al., 2006] esti-

mates are smaller than our estimates, by about one order of magnitude in the upper 4000m, and up to almost three orders of magnitude below this depth. Based on our inability to reproduce the [Kunze et al., 2006] results we conclude that their dissipation estimates are suspiciously small.

Another indication that the [Kunze et al., 2006] dissipation estimates may be biased low is the fact that they are systematically smaller than the canonical Garrett-Munk dissipation value (refer to Fig. 3.14). Moreover, [Nikurashin and Ferrari, 2009] find that their simulations of internal wave radiation and dissipation in Drake Passage and the Scotia Sea (Southern Ocean) are larger than dissipation estimates inferred from observations by [Kunze et al., 2006] and agree with [Naveira-Garabato et al., 2004a].

The dissipation estimates discussed in this chapter will be compared to the box-model estimates from Chapter 2 in Chapter 4.

Chapter 4

Comparison of large scale and fine scale dissipation estimates

4.1 Introduction

In this chapter we test the hypothesis that the Indian Ocean MOC can be sustained by internal wave breaking. We test this hypothesis by comparing the MOC energy budget we discussed in Chapter 2 with the in-situ estimates of internal wave dissipation as presented in Chapter 3.

The fine scale method to estimate in-situ dissipation rates (refer to Chapter 3) is designed to parameterize turbulent dissipation due to internal wave breaking and is based on the assumption that elevated internal wave energy density leads to elevated dissipation. Away from internal wave energy sources or sinks we expect GM-like energy levels (we discuss the GM model in Section 5.4.3). Under non-GM conditions, for example at generation sites and at places of increased nonlinear interaction we expect higher energy levels. Such sites are often related to bottom topography, because internal tides may be generated at super critical

slopes and waves are scattered by rugged topography (see for example [Nycander, 2005] and [Polzin et al., 1997]).

Non-linear interactions among internal waves cause a net transfer of energy to smaller scales which will eventually lead to wave breaking and turbulent dissipation. Internal wave–wave interaction depends on latitude through the inertial frequency (f). Independent of topography we expect internal wave dissipation to drop close to the equator, because the rate at which waves are Doppler shifted is smaller for smaller f [Gregg et al., 2003] and we expect elevated wave–wave interaction close to 28.9°, because of increased parametric subharmonic instability at this latitude [MacKinnon and Winters, 2005].

The dissipation rate is highly variable, both in time and space. In this study we focus on the spatial variability associated with topography, but we will touch on temporal variability in Section 4.3.4. Section 4.3.3 discusses sites of extremely elevated dissipation rates, the so called 'mixing hotspots'. The dissipation rate at these sites is typically a factor 100 to 1000 higher than the background value. To obtain any useful statistic it is therefore essential that hotspots are well represented in the data set, that is the magnitude of the dissipation rate should be approximately right and the number of sampled hotspots should be representative for the basin wide distribution. If these conditions are not met we might end up comparing 'applesauce and oranges' as [Munk and Wunsch, 1998] have warned against.

Whether our set of measurements is adequate to estimate the mean dissipation rate depends on our ability to model the statistical nature of ocean turbulence. In this chapter we investigate a number of potential biases with regard to the spatial distribution

of the measurements.

4.2 Null hypothesis

In chapter 2 we use a one dimensional box-model in density space to estimate the basin-wide mean dissipation rate. In chapter 3 we use a parameterization to infer dissipation rate from fine structure measurements. The resulting in-situ dissipation estimates are interpolated onto density levels using linear interpolation. Section 4.5 discusses the way we calculate the Indian Ocean mean dissipation rate and its uncertainty.

In this chapter we assess whether there is enough energy in the internal wave field to support the Indian Ocean MOC. More specifically we will compare the fine scale dissipation estimates with five hydrography based estimates of the Indian Ocean MOC. This means that we test the null hypothesis,

$$H_0 : \mu \geq L \quad \text{against} \quad H_1 : \mu < L, \tag{4.1}$$

with μ the mean fine scale dissipation rate and L the large scale dissipation rate. We reject the null hypothesis H_0 when the upper confidence level of μ is smaller than L.

4.3 Exploratory statistics

4.3.1 Ensemble statistics

This section discusses the basic statistics of the ensemble of all fine scale dissipation estimates. The ensemble of observations includes only single occupations. Only data from LADCP down casts is used if up– and down cast data are separately available. In case of multiple occupation of the same section we use the data col-

lected closest to 1995[1] to minimize temporal spread in the ensemble. In order to achieve better spatial coverage we also include CTD-only estimates in the ensemble.

The probability density distribution of the dissipation rates is shown in Fig 4.1. The range of dissipation rates is between 3.1×10^{-14} and 1.5×10^{-6} m^2s^{-3} with most measurements close to the median, i.e. 1.6×10^{-10} m^2s^{-3}. Negative dissipation rates have no physical meaning and the probability distribution is therefore strongly skewed to the right, with a skewness of 37. Another difference in comparison to the Gaussian distribution is the fact that the observed probability density is more peaked. This property is expressed by the high kurtosis value of 1640, much larger than the 'normal' value of 3.

The asymmetry (skew) and peakiness (kurtosis) of the distribution make its mean sensitive to values in the high-end tail. This is best illustrated by a simple example. Suppose we have systematically underestimated/undersampled the mixing hotspots by factor 10, and we correct for this by multiplying the highest 1% of the data by factor 10. This correction, to only 1% of the data in the thin high-end tail, has a large impact on the mean[2] and results in a 6.9 times higher value (from 2.14×10^{-9} to $1.48 \times 10^{-8} m^2s^{-3}$).

Figure 4.1 shows the frequency histogram of the dissipation rate (left panel) and the density histogram of the logarithm of the same dissipation estimates (right panel). A maximum likelihood fit of a standard normal distribution to the pdf of $\log(\epsilon)$ shows that the data is approximately lognormally distributed. This suggests that the logmean of the dissipation estimates

[1] 1995 is a year with many Indian Ocean WOCE observations.

[2] Strictly speaking we should increase the number of elements by 1% when accounting for undersampling, but this makes a minor difference.

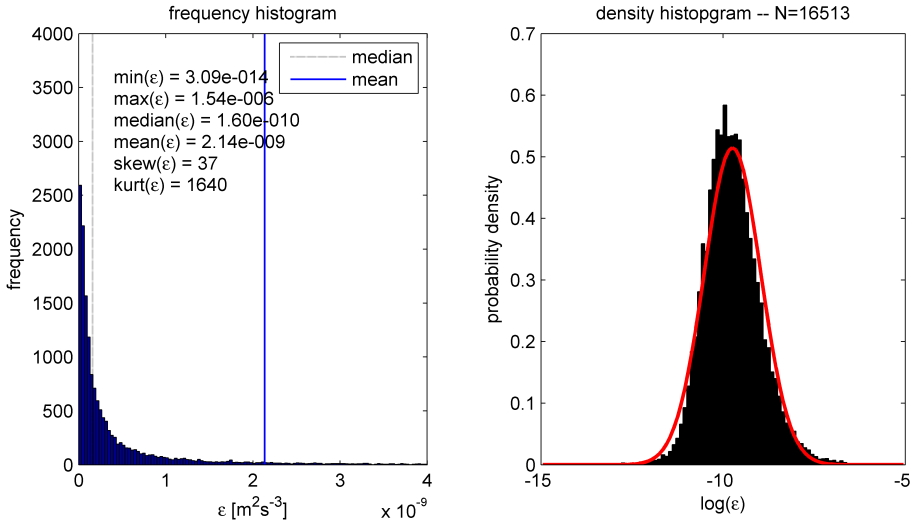

Figure 4.1: Basic statistics of all estimated values for the dissipation rate. Left: frequency histogram. Right: logarithmic density histogram. The red line is a normal distribution with fit parameters $\hat{\mu} = -9.74 \pm 0.01$ and $\hat{\sigma} = 0.77 \pm 0.01$. The range indicates 95% confidence intervals.

is less sensitive to outliers, and therefore a more robust statistic, than the arithmic mean.

4.3.2 Isopycnal statistics

We interpolate the dissipation estimates onto density surfaces to enable comparison with the large scale MOC energy budget as discussed Chapter 2. This transformation to density space is possible because there is an one-to-one relation between the vertical coordinate (parallel to gravity) and the density γ of a (stably) stratified fluid.

Table 4.1 shows some basic dissipation statistics at the large scale density levels defined in Chapter 2. The inferred fine scale dissipation rates are interpolated onto the density levels using linear interpolation. The table shows that the median value is smaller than the mean for all density levels. This is consistent with a right-skewed distribution and we indeed find a positive

skewness for each of the isopycnal ensembles, as shown in the second column from the right. The scaling of the mean and median dissipation rate with depth corresponds to the dissipation patterns shown in Fig. 3.10 and Fig. 3.11. These figures generally show high dissipation rates in the upper 1000m, smaller values of order 10^{-10} m^2s^{-3} at intermediate depth, and elevated dissipation towards the bottom. The bottom intensification in the table is not very pronounced because we do not regard densities larger than 28.15 kg m^{-3}. Figure 2.4 shows that this isopycnal lingers around 3800m at 32°S, which is still about 1km from the bottom.

4.3.3 Mixing hotspots

Mixing rates in the upper ocean interior are typically of order 1×10^{-5} m^2s^{-1} [Gregg, 1989]. That is about a factor 10 smaller than the mixing rate required to sustain the global MOC [Munk, 1966]. This observation has led to the conjecture that most mixing takes place in relatively few vigorous mixing regions. Such 'mixing hotspots', with mixing rates up to 1000 times higher than the open ocean value, have indeed been identified over the past 15 years. Sites of elevated mixing include rough topography (ridges, seamounts, continental slopes etc.) [Polzin et al., 1997; Ledwell et al., 2000] and submarine canyons [Thurnherr et al., 2005].

In this section we look for sites with high dissipation rates. We identify hotspots using the criterion that the local dissipation rate at a density level is higher than the median value of the large scale dissipation estimates from Chapter 2. Figure 4.2 shows the locations of these sites for five different density levels.

The general picture arising from Fig. 4.2 is that all hotspots are located south of the equator and that there are more hotspots in the western half of the

ID	DPTH	DENS	N	MEAN	MEDIAN	STD	SKEW	KURT
1	0	22.42	0	–	–	–	–	–
2	42	23.56	0	–	–	–	–	–
3	87	24.47	0	–	–	–	–	–
4	137	25.21	16	1.2e-007	7.8e-009	3.8e-007	4	14
5	192	25.79	60	9.1e-008	5.8e-009	2.5e-007	4	16
6	257	26.26	183	4.3e-008	4.1e-009	1.2e-007	5	30
7	349	26.64	615	2.0e-008	2.2e-009	6.6e-008	7	59
8	543	26.94	1294	6.8e-009	8.6e-010	2.8e-008	10	113
9	765	27.18	1631	1.6e-009	4.6e-010	4.2e-009	8	104
10	930	27.37	1629	1.1e-009	3.4e-010	2.4e-009	5	40
11	1100	27.53	1594	8.7e-010	2.8e-010	1.9e-009	6	45
12	1285	27.65	1546	6.6e-010	2.2e-010	1.6e-009	9	123
13	1466	27.75	1490	6.3e-010	1.9e-010	2.9e-009	27	899
14	1639	27.83	1457	4.7e-010	1.7e-010	1.1e-009	8	115
15	1808	27.89	1395	3.6e-010	1.4e-010	7.2e-010	6	54
16	1971	27.94	1286	2.9e-010	1.2e-010	5.3e-010	5	31
17	2146	27.99	1191	2.5e-010	9.5e-011	5.7e-010	8	90
18	2335	28.02	1142	2.3e-010	8.2e-011	9.7e-010	26	769
19	2537	28.04	1091	2.0e-010	7.9e-011	3.7e-010	5	38
20	2756	28.07	1016	1.8e-010	8.2e-011	3.3e-010	5	32
21	2965	28.08	932	2.0e-010	8.9e-011	3.7e-010	6	62
22	3154	28.10	848	2.1e-010	8.7e-011	3.6e-010	4	26
23	3322	28.11	774	2.2e-010	9.3e-011	4.8e-010	9	120
24	3466	28.12	703	2.4e-010	9.7e-011	6.7e-010	16	323
25	4058	28.15	448	4.3e-010	1.3e-010	1.5e-009	10	129
all	–	–	22341	2.12e-009	1.75e-010	2.46e-008	34	1551

Table 4.1: Statistics of the dissipation rate interpolated onto neutral density levels.

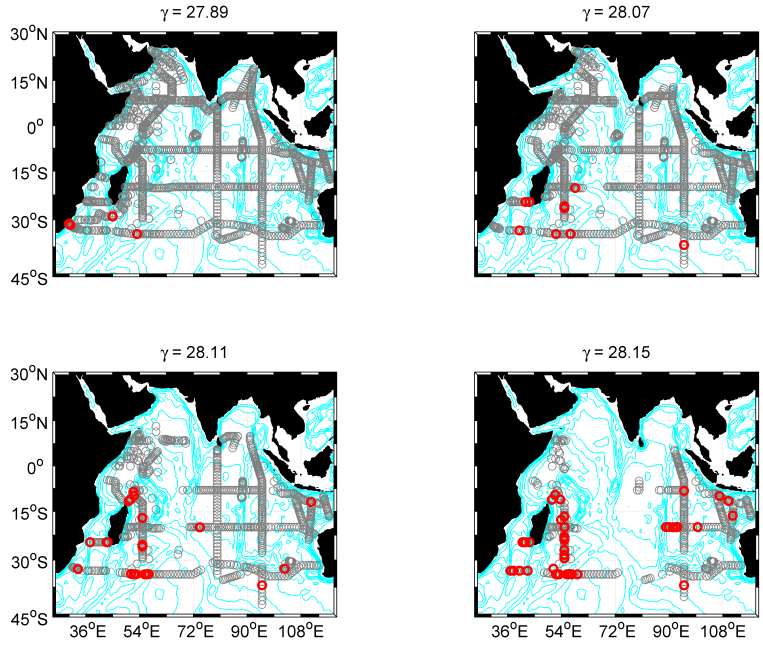

Figure 4.2: Dissipation hotspots red circles at four different density levels. The hotspots are marked with red circles and defined as locations where the fine scale dissipation rate is larger than the median of the large scale basin wide estimates. Grey circles indicate locations that do *not* satisfy this criterion. Depth contours are drawn every 750m.

basin. The density of hotspots appears particularly high in the Southwest Indian Ridge (refer to Fig. 2.4 for a map with labelled topography), close to the southwestern tip of Madagascar, around the Amirante Passage (between the Mascarene– and Somali Basin), and in the Madagascar Basin. In the eastern half of the basin, east of Ninety East Ridge (NER), we find a cluster of hotspots around 20°S and a single hotspot at about 10°S, which might be related to a saddle point in the NER at this latitude [Warren and Johnson, 2002]. We also find a few scattered hotspots at the continental shelf break south of Indonesia.

4.3.4 Temporal variability

We explore the temporal variability of the dissipation rate by comparing the January 1995 and March 2007 occupation of section I09N. The top left panel of Fig. 4.3 shows that the 2007 cruise has not occupied all the 1995 stations. In the comparison however we only use stations that are less than 600m apart.

The top right panel of Fig. 4.3 compares the depth mean dissipation rate in 500m depth bins. The means are the means of the logarithm of the dissipation rate which is close to the geometric mean (i.e. median) for a quasi-lognormal distribution. Assuming lognormality we may perform a paired T-test and find that mean values are *not* significantly different at all depth levels.

The bottom panel of Fig. 4.3 compares the geometric means per station for all stations with at least 5 dissipation estimates. We observe similar patterns for 1995 and 2007 and when applying a T-test to the logged dissipation estimates we again find that the mean has not changed significantly for most stations. The observed general similarity between the station mean and depth mean dissipation rates is consistent with a quasi-steady dissipation climate on decadal time scales. Based on this result we assume that isopycnal mean dissipation rates, based on observations in different years, may be put together in a single statistical ensemble.

4.4 Sampling biases

4.4.1 Latitude

The parameterization used to infer dissipation (3.3) depends on latitude through $L(f, N) \propto f\,\mathrm{acosh}(N/f)$, with $f \propto \sin(\mathrm{lat})$ the inertial frequency and N the buoyancy frequency. The latitudinal function $L(f, N)$

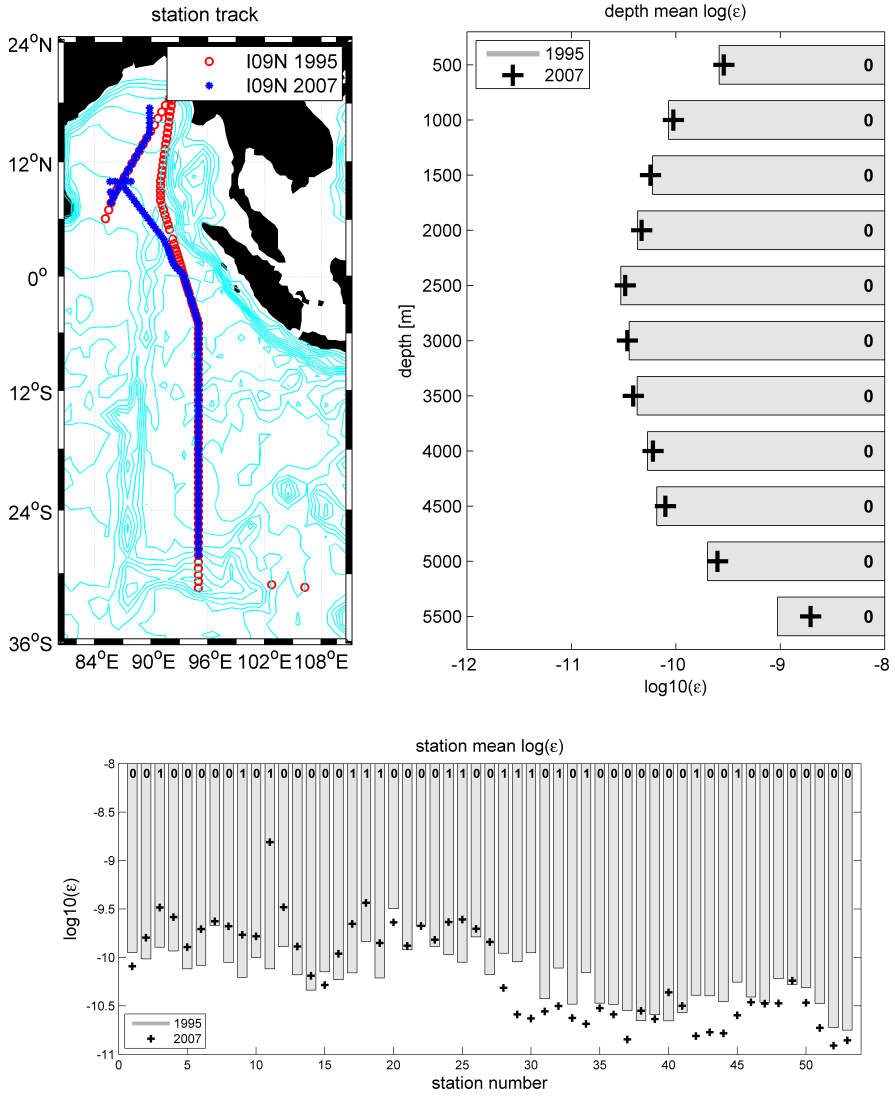

Figure 4.3: Comparison of dissipation estimates inferred from the 1995 and 2007 occupation of I09N. Top left: station track with 500m depth contours. Top right: depth mean dissipation rate. Bottom: station mean dissipation rate. The number at the top of the grey bars indicate whether the means of $\log_{10}(\epsilon)$ are different (1 means different) at 0.05 significance.

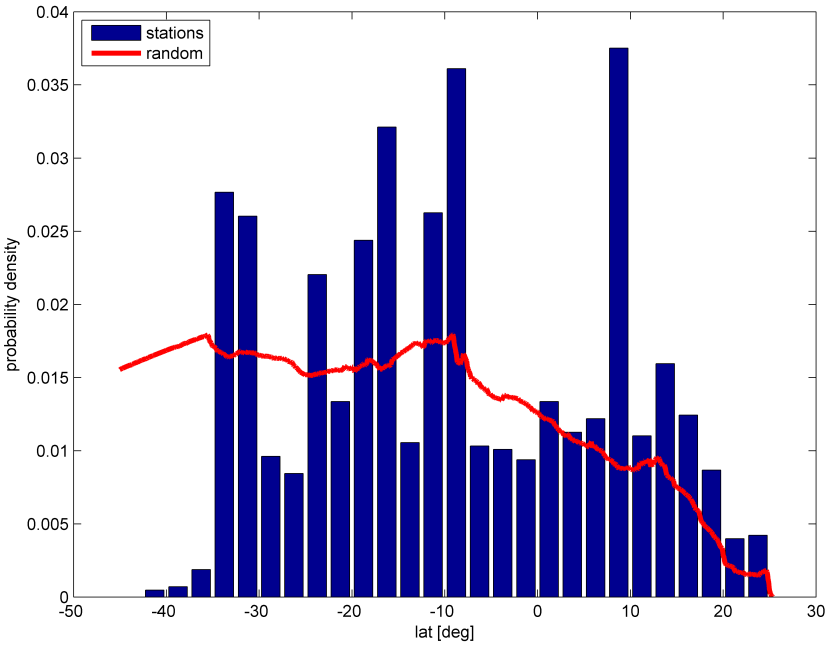

Figure 4.4: Estimated probability density P(lat) for station locations and random locations in the Indian Ocean between 45°S and 30°N.

is zero at the equator and close to one for latitudes larger than 10°. We therefore expect that the sample distribution with respect to latitude matters for the mean dissipation rate. Oversampling in equatorial waters, for example, would lead to underestimation of the mean dissipation rate.

The distribution of hydrographic stations is not likely to be random with respect to latitude, because of the WOCE sampling strategy with zonal sections. Indeed, the histogram of station probability densities, as shown in Fig. 4.4, shows higher probabilities around the latitudes of the zonal sections (nominally: 30°S, 20°S, 10°S, 0°, 10°N). The probability of a truly random sample scales with the width of the basin and is also shown in Fig. 4.4.

The latitudinal sampling bias can be corrected for

distribution		$\langle\epsilon\rangle$ $[10^{-9}$ m^{2}s$^{-3}]$
uniform	(all latitudes have same probability)	2.28
observational	(latitudes of hydrographic stations)	1.97
random	(latitudes scales with basin width)	2.45

Table 4.2: Latitudinal bias estimates. The mean dissipation rate $\langle\epsilon\rangle$ is based on (3.5).

by applying weights to the dissipation estimates. The effect of such a correction may be considerable if the dissipation rate indeed scales as $L(f, N)$. We estimate this bias by comparing three spatial distributions, (i) uniform: all latitudes have the same probability, (ii) random: latitudes are distributed according to the basin shape, and (iii) observational: latitudes of hydrographic stations.

Table 4.2 compares the mean dissipation rate within the latitude band from $-45°$S to $30°$N for these latitude distributions. The results are obtained by calculating the average of, $\epsilon = \epsilon_0 L(f, N)$ (refer to (3.5)), for the each latitude distribution. This simple example shows that the observed mean dissipation rate may be biased low by about 25%.

Figure 4.5 shows the observed dissipation rate between 500m and 1000m versus latitude and the average dissipation rate in $1°$ latitude bins. The scaling with latitude of the dissipation estimates looks flatter than $L(f, N)$, with a less pronounced dip at the equator than prescribed by $L(f, N)$. This observation is consistent with lower shear-to-strain ratios close to the equator, that is higher $h_1(R)$ values, due to the propagation of near-inertial waves to lower latitudes. The impact of non-random sampling would be less pronounced, if the dependency on latitude is indeed weaker, and the 25% bias is therefore likely an upper bound.

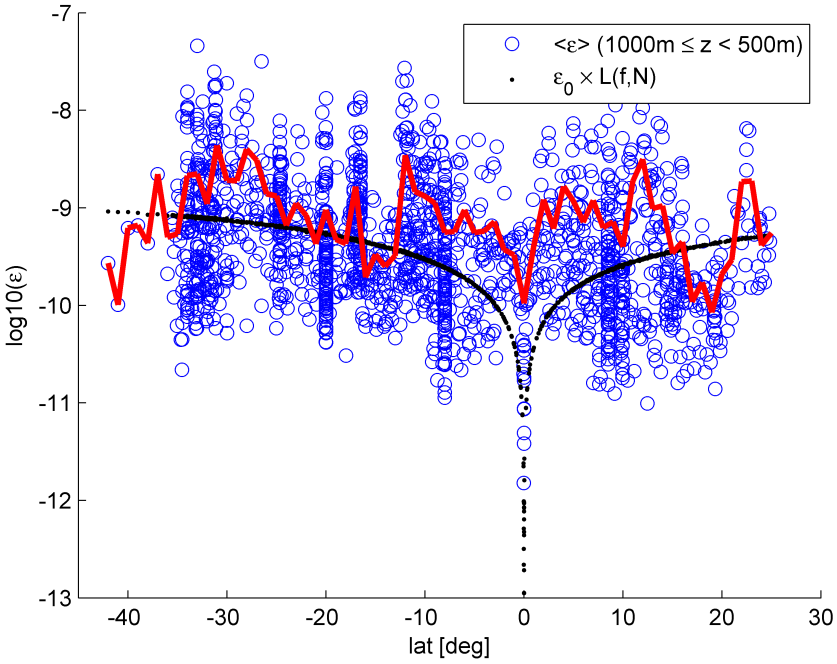

Figure 4.5: Upper ocean dissipation estimates (1000m≤z<500m) versus latitude (blue dots) and averaged over 1° latitude bins (red line). The analytical dissipation rate $\epsilon_0 \times L(f, N)$ is also shown for reference (black dots).

4.4.2 Bottom roughness

Roughness of bottom topography is a measure for the variance of the bathymetry (refer to App. B). Most variance is associated with the larger topographic structures and those are mostly found in the western half of the Indian Ocean. Many areas of high roughness are easily identifiable when we overly Fig. 4.6 and Fig. 2.4. We observe that roughness is associated with features such as the Southwest Indian Ridge, the Central Indian Ridge, the Owen Fracture Zone, the Carlsberg Ridge (i.e. the northern extension of the Central Indian Ridge), the Mascarene Plateau (northeast of the Mascarene Basin), and the Chagos-Loccadive Ridge (meridionally oriented around 72°E, just south of India). The eastern basin has generally smaller topographic features with little roughness. Most roughness in the east is associated with the Southeast Indian Ridge, Broken Plateau, the Lost Dutchmen Ridge (between Broken Plateau and Australia), and generally in the North Australia Basin, including Java Ridge. The Ninetyeast Ridge is an example of a large topographic feature with little roughness.

Scattering and generation of internal waves at rough topography explains the generally observed positive correlation between roughness and turbulent dissipation [Polzin et al., 1997; Ledwell et al., 2000]. Our dissipation estimates are also weakly correlated with roughness (refer to Fig. 4.7). Under– or over sampling of areas with high roughness may therefore bias the mean dissipation rate. Rejection of the null hypothesis, *locations of hydrographic stations are random with respect to roughness*, means that a roughness bias is to be expected.

We test the null hypothesis by comparing the empirical probability density distribution of roughness at all Indian Ocean grid points with the distribution of

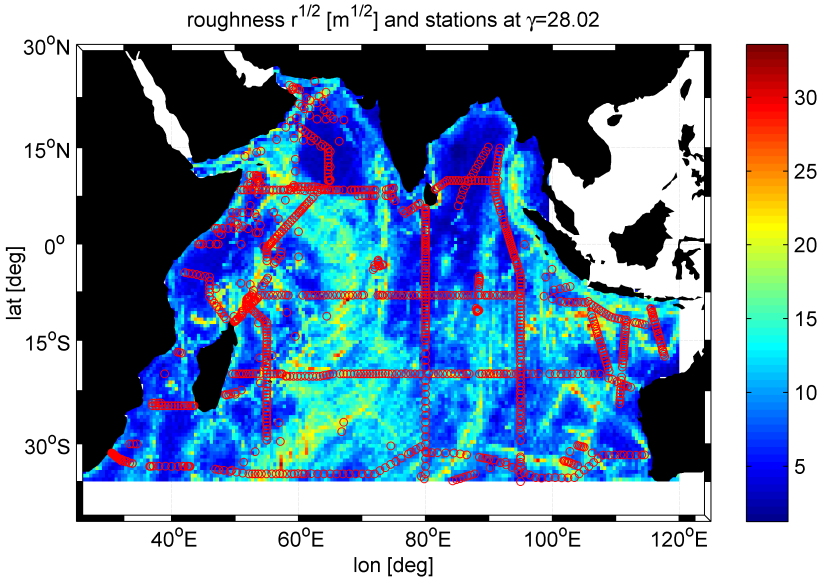

Figure 4.6: Square-root of bottom roughness and hydrographic stations in red. The roughness is calculated in 0.5×0.5 degree non-overlapping grid cells (refer to App. B).

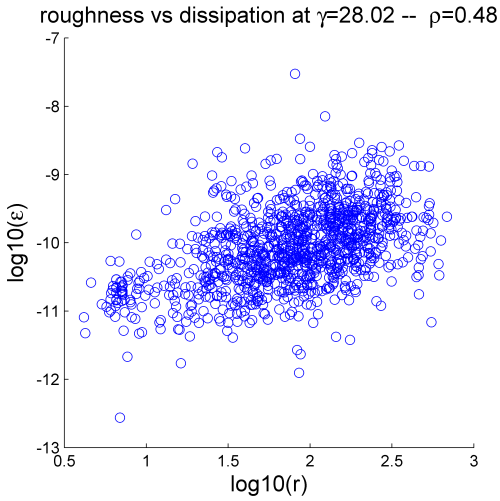

Figure 4.7: Scatter plot of the logarithm of the roughness parameter r versus the logarithm of the dissipation rate ϵ. The parameter ρ is the linear correlation coefficient.

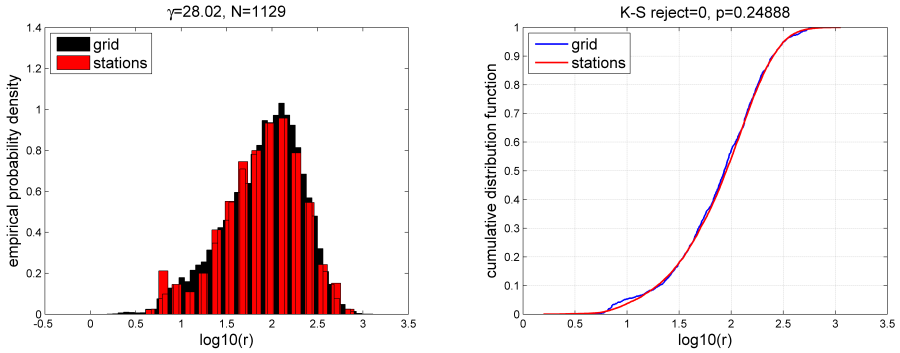

Figure 4.8: Comparison of roughness at all Indian Ocean grid points with roughness at the location of hydrographic stations. Left panel: empirical probability density histogram. Right panel: empirical cumulative density function.

roughness at the station locations. Roughness at station locations is estimated from the roughness grid cells by triangle-based linear interpolation. The left panel of Fig. 4.8 shows the probability distribution of all grid cells and the roughness at station locations. Both distributions look similar, suggesting random sampling. This notion is enforced by comparing the cumulative density functions and applying a two-sample Kolmogorov-Smirnov test. The test confirms that the samples are from the same underlying population with 95% likelihood. We therefore accept the null hypothesis and conclude that there is no significant roughness bias.

4.4.3 Internal tides

The energy flux from the M_2 tide to internal waves can be estimated as a function of the tidal velocity, the bottom roughness and the buoyancy frequency. Figure 4.9 shows the Indian Ocean segment of the global map based on linear theory [Bell, 1975], as presented by [Nycander, 2005] (refer to Fig. 5), which is based on Smith and Sandwell bathymetry, the TPXO.6 tidal

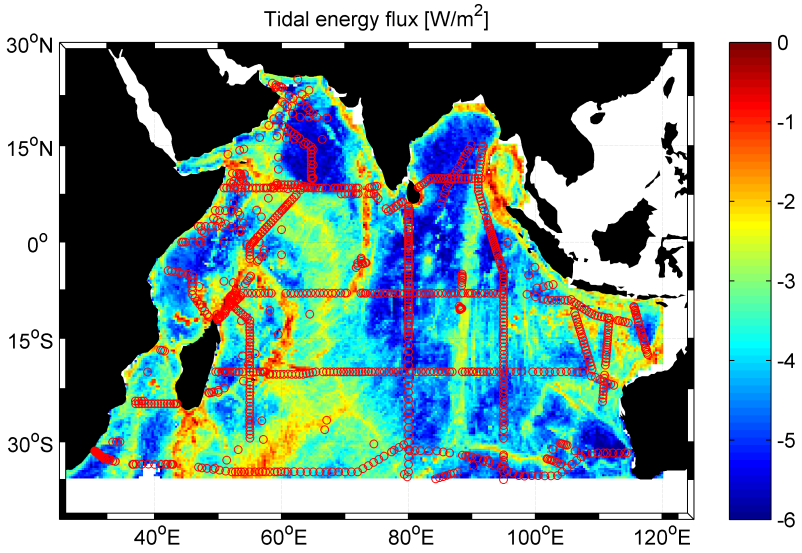

Figure 4.9: Energy conversion to internal tides [Wm^{-2}] for one third degree grid cells and with a logarithmic colour scale (courtesy J. Nycander). Red circles indicate hydrographic stations.

velocity field, and the SAC[3] hydrographic climatology.

We estimate the sampling bias with respect to the distribution of tidal energy conversion by comparing the energy flux at all grid cells with the energy flux at station locations. This is directly analogous to the estimation of the roughness bias in Section 4.4.2. Figure 4.10 shows the histogram of both distributions. As with roughness we again find that the Kolmogorov-Smirnov test accepts the hypothesis that the stations are sampled randomly with respect to internal tides. We therefore expect no significant tidal bias.

[3]World Hydrographic Program Special Analysis Centre

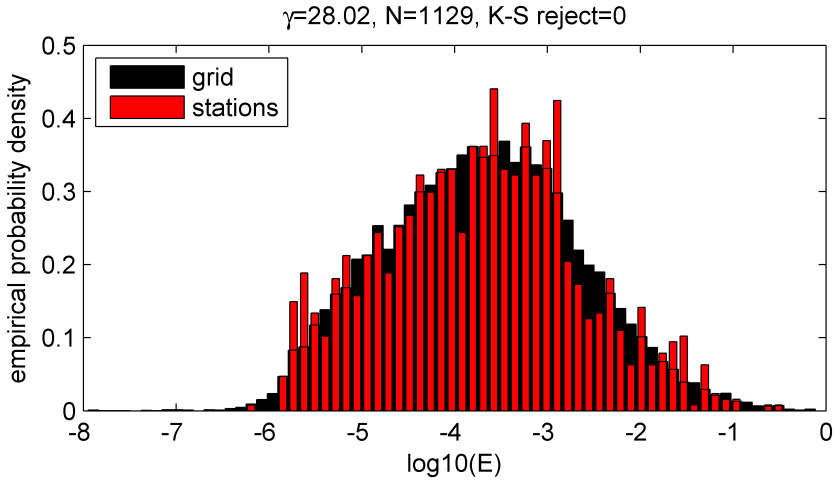

Figure 4.10: Empirical probability density histogram of the energy flux to internal tides at all Indian Ocean grid cells and at station locations (tidal conversion rates from J. Nycander).

4.5 Hypothesis testing

4.5.1 Perfect data assumption

In Section 4.3.1 we saw that the distribution of dissipation rates has a heavy right tail. This makes the mean of the distribution sensitive to outliers. However, the mean is still a robust statistic in the absence of outliers, that is when all values, including the extreme ones in the tail can be trusted to accurately represent the real dissipation rate.

We will consider the data perfect when all estimates are 100% accurate *and* randomly sampled from the real ocean dissipation field. Under these idealized conditions there is no reason to suspect the mean value for a sufficiently large sample set. In Table 4.3 we compare the simple arithmetic mean of the inferred dissipation with the large scale dissipation estimates.

In order to either accept or reject the null hypothesis (i.e. internal waves can sustain the Indian Ocean MOC) we will need an estimate of the statistical un-

certainty. Avoiding strong parametric assumptions, in particular the obviously unfit assumption of normality that is inherent to the standard deviation, we chose to use bootstrap resampling (refer to App. C) to estimate the uncertainty. Bootstrap estimates of the mean and its standard deviation are given in Table 4.3 for a resampling frequency of 1000. The null hypothesis is rejected when the mean plus three standard deviations is smaller than the large scale value.

Focussing on layers relevant to the deep MOC, which we choose to be layers denser than 27.00, we see that the fine scale inferred mean dissipation rate is sufficient to support the large scale estimates for a few layers only. The energy in the internal wave field is sufficient to support the MCD solution for $\gamma = 27.18$ kg m^{-3} and $\gamma = 27.37$ kg m^{-3}, the BRY solution for $\gamma = 28.12$ kg m^{-3} and $\gamma = 28.15$ kg m^{-3}, and the SLO solution for $\gamma = 28.15$ kg m^{-3}. Based on this comparison we conclude that the estimated internal wave dissipation falls short to support the Indian Ocean MOC at all other density levels.

4.5.2 Lognormal assumption

In Section 4.3.1 we saw that the probability density function (pdf) of the logged dissipation estimates resembles the bell-shape of the standard normal pdf. The pdf of a truly lognormal ϵ-distribution can be written as,

$$f(\epsilon|\mu,\sigma) = \frac{1}{\epsilon\sigma\sqrt{2\pi}} \exp\left(-\frac{(\log(\epsilon)-\mu)^2}{2\sigma^2}\right), \qquad (4.2)$$

with 'logmean' μ and 'logvariance' σ^2 and expected value $\exp(\mu + \frac{1}{2}\sigma^2)$. In Fig. 4.11 we compare the logarithm of the fine scale expected value, i.e. $\mu + \frac{1}{2}\sigma^2$, and the logarithm of the large scale expected value. Assuming lognormality we use $\mu = \text{mean}(\log(\epsilon))$ and

ID	DENS	MEAN	STD	MCD	GAN	FER	BRY	SLO
1	22.42	–	–	–	–	–	–	–
2	23.56	–	–	–	–	–	–	–
3	24.47	–	–	–	–	–	–	–
4	25.21	1.23e-007	8.83e-008	0	0	0	0	0
5	25.79	9.23e-008	3.11e-008	0	0	0	0	0
6	26.26	4.26e-008	9.12e-009	0	0	0	0	0
7	26.64	1.97e-008	2.78e-009	0	0	0	0	0
8	26.94	6.82e-009	8.07e-010	0	0	1	1	1
9	27.18	1.60e-009	1.01e-010	0	1	1	1	1
10	27.37	1.09e-009	5.93e-011	0	1	1	1	1
11	27.53	8.67e-010	4.88e-011	1	1	1	1	1
12	27.65	6.62e-010	4.05e-011	1	1	1	1	1
13	27.75	6.26e-010	7.48e-011	1	1	1	1	1
14	27.83	4.69e-010	2.89e-011	1	1	1	1	1
15	27.89	3.65e-010	1.82e-011	1	1	1	1	1
16	27.94	2.93e-010	1.50e-011	1	1	1	1	1
17	27.99	2.49e-010	1.55e-011	1	1	1	1	1
18	28.02	2.33e-010	2.81e-011	1	1	1	1	1
19	28.04	1.96e-010	1.04e-011	1	1	1	1	1
20	28.07	1.85e-010	1.04e-011	1	1	1	1	1
21	28.08	1.97e-010	1.19e-011	1	1	1	1	1
22	28.10	2.06e-010	1.22e-011	1	1	1	1	1
23	28.11	2.22e-010	1.71e-011	1	1	1	1	1
24	28.12	2.36e-010	2.43e-011	1	1	1	0	1
25	28.15	4.23e-010	7.13e-011	1	1	1	0	0

Table 4.3: Bootstrap estimates of the mean dissipation rate and the standard deviation with $B = 1000$ for the number of bootstrap replicates (refer to App. C). The logical in the last five columns indicates whether the null hypothesis is rejected (1 means rejection).

$\sigma^2 = \mathrm{var}(\log(\epsilon))$.

The bars in Fig. 4.11 represent the basin-wide isopycnal dissipation rates with fine scale estimates in red. Green-blue-ish bars represent the fine scale expected value under the assumption of lognormality.

Assuming lognormality we can perform a T-test to check whether the logged data are a random sample from a normal distribution with a given mean. We use the one-sample T-test to check whether the mean of the logged data is larger or equal to the large scale (LS) logmean. The large scale logmean can be calculated from the expected value when we assume that the variance is similar to the fine scale (FS) variance. Writing $E[\epsilon]$ for the large scale expected value and assuming lognormality so that $\log(E[\epsilon]) \approx \mu_{LS} + \frac{1}{2}\sigma^2_{LS}$, we find the large scale logmean by assuming $\sigma^2_{LS} \approx \sigma^2_{FS}$.

Table 4.4 shows whether the T-test has accepted the null hypothesis (4.1) for all density layers and all large scale expected values. The null hypothesis is rejected for all large scale expected values at densities between $\gamma = 26.94$ kg m^{-3} and $\gamma = 28.12$ kg m^{-3}. Disregarding surface layers we conclude that the null hypothesis is only accepted for the [Bryden and Beal, 2001] and [Sloyan and Rintoul, 2001] solution at the densest level.

This result is in qualitative agreement with the bootstrap comparison in Table 4.3. The apparent similarity of mean and logmean values seems to indicate that the fine scale mean is not significantly contaminated by outliers. We conclude that assuming lognormality does not appreciably change the findings from the previous section. In other words, the shortfall of energy in the internal wave field to support the Indian Ocean MOC persists under the assumption of lognormality.

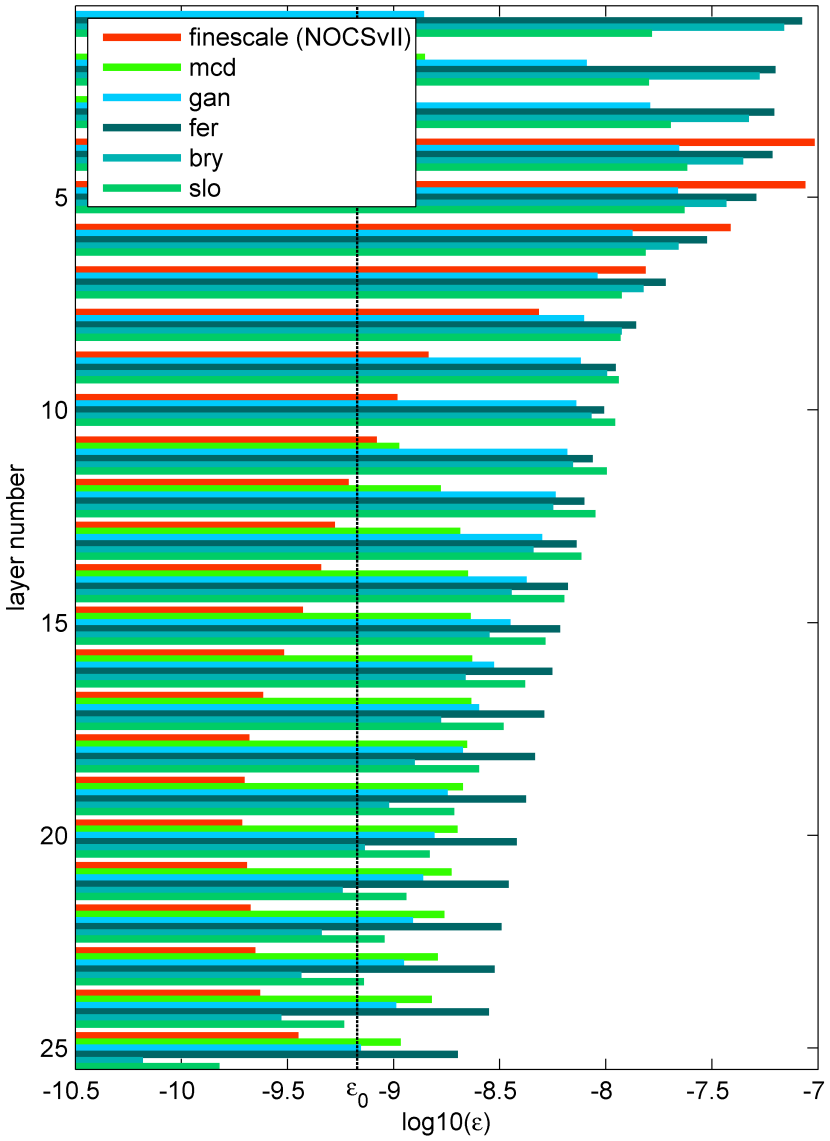

Figure 4.11: Logmean of the fine scale dissipation estimates (red) and the largescale dissipation estimates for the various overturning solutions considered in this study. The Garret-Munk background dissipation rate ϵ_0 is plotted for reference. Refer to Table 4.1 for the layer densities and to Table 2.1 for the meaning of the large scale abbreviations.

ID	DENSITY	LOGMEAN	MCD	GAN	FER	BRY	SLO
1	22.42	–	–	–	–	–	–
2	23.56	–	–	–	–	–	–
3	24.47	–	–	–	–	–	–
4	25.21	1.06e-008	–	0	0	0	0
5	25.79	8.58e-009	–	0	0	0	0
6	26.26	5.81e-009	–	0	0	0	0
7	26.64	2.85e-009	–	0	1	0	0
8	26.94	1.06e-009	–	1	1	1	1
9	27.18	4.94e-010	–	1	1	1	1
10	27.37	3.71e-010	–	1	1	1	1
11	27.53	2.99e-010	1	1	1	1	1
12	27.65	2.32e-010	1	1	1	1	1
13	27.75	1.96e-010	1	1	1	1	1
14	27.83	1.70e-010	1	1	1	1	1
15	27.89	1.41e-010	1	1	1	1	1
16	27.94	1.18e-010	1	1	1	1	1
17	27.99	9.53e-011	1	1	1	1	1
18	28.02	8.59e-011	1	1	1	1	1
19	28.04	8.19e-011	1	1	1	1	1
20	28.07	8.11e-011	1	1	1	1	1
21	28.08	8.64e-011	1	1	1	1	1
22	28.10	8.97e-011	1	1	1	1	1
23	28.11	9.29e-011	1	1	1	1	1
24	28.12	9.86e-011	1	1	1	1	1
25	28.15	1.38e-010	1	1	1	0	0

Table 4.4: T-test of the hypothesis that the logged fine scale dissipation estimates come from a distribution with a mean given by the large scale expected value minus the variance of the logged fine scale estimates. Outcome '1' means that null hypothesis (4.1) is rejected under the assumption of lognormality at a 0.05 significance level.

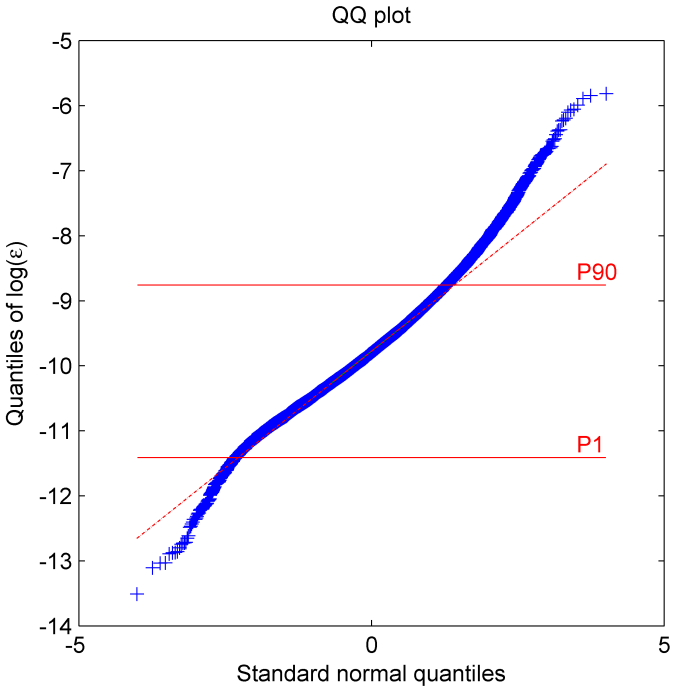

Figure 4.12: Quantile–quantile plot of the logarithm of the ensemble of all dissipation estimates versus the standard normal distribution. Q1 and Q3 are the first and third quartile value of $\log_{10}(\epsilon)$.

4.5.3 Parametric bias

The parametric assumption about the lognormality of the dissipation rate is useful to estimate confidence intervals for purposes of comparison, but may also introduce bias when the underlying distribution differs. Here we discuss differences between the data set and the lognormal distribution based on the quantile–quantile plot in Fig. 4.12.

The plot shows that dissipation estimates are close to normally distributed in the range $10^{-11} < \epsilon < 10^{-9}$ $\mathrm{m^2 s^{-3}}$. Low and high dissipation rates outside this range are biased by over an order of magnitude.

When using the T-test in Section 4.5.2 we assume lognormality and we expect the test to be reasonably robust under small departures from normality for suf-

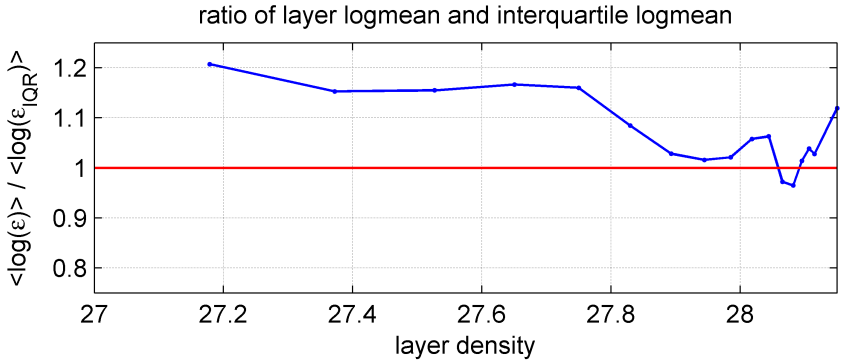

Figure 4.13: Ratio of the mean of $\log_{10}(\epsilon)$ and mean of the interquartile range at a given density layer. Note that we only display layers with a density larger than 27.00.

ficiently large sample sizes. The T-test compares the mean value of a supposedly normally distributed data set x with a given value μ_0 using the statistic,

$$t = \frac{\overline{x} - \mu_0}{s/\sqrt{n}}, \tag{4.3}$$

where $\overline{x}$ is the sample mean, s the variance and n the number of elements.

Figure 4.12 shows that the data is close to lognormal within the interquartile range. We estimate the effect of the heavy tails by comparing the mean of $x = log(\epsilon)$ with the mean in the interquartile range $\overline{x_{IQR}}$. Figure 4.13 shows that the ratio $\overline{x}/\overline{x_{IQR}}$ is within 20% difference for denser layers, with $\gamma \geq 27.18$. From this plot we conclude that the logmean is hardly biased by the heavy tails when compared to the lognormal distribution.

The variance of the observed distribution is larger than the variance of a distribution with lighter, lognormal tails. The statistic t (refer to (4.3)) could therefore overestimate the probability of x having mean value μ_0. In our case this means that the few cases where the T-test has accepted the null hypothesis (4.1) might still be rejected at the 95% level when we correct for

this bias. This enforces our conclusion that the energy in the internal wave field falls short to support the investigated Indian Ocean MOC solutions.

4.6 Discussion

The main result of this chapter is graphically displayed in Fig. 4.11. The figure shows the basin-wide fine scale and large scale dissipation estimates at 25 density levels. Disregarding the top 10 levels, corresponding to shallow depths below ∼1000m, and the lowest density, i.e. the 28.15 kg m^{-3} isopycnal, we find that the fine scale estimates are always *smaller* than all the large scale estimates. The gap between fine– and large scale estimates is considerable, more than one order of magnitude at most density levels, and much larger than the spread among the large scale estimates.

The statistical comparison of the fine scale and large scale estimates discussed in this chapter accounts for uncertainty due to undersampling, but does not explicitly discuss the uncertainty of the estimates themselves. Inverse model errors are discussed in Section 2.4.1, but error estimates are not available for all the inverse solutions discussed in this work. Alternatively, we interpret the spread among the various inverse solutions as a measure for the uncertainty about the Indian Ocean MOC.

The fine scale parameterization is shown to be accurate to within a factor 2–3 when compared to microstructure dissipation estimates. In principle we do not believe that this level of accuracy is compromised by the previously discussed discrepancy between our estimates and estimates published by [Kunze et al., 2006] (see Section 3.4.5), because we have reason to believe that this difference is due unintentional biases introduced by their implementation of the model [Polzin

et al., 2010].

Assuming that our fine scale method produces reasonably reliable estimates of internal wave dissipation leads to the question whether the MOC can be closed by other mixing processes that are not captured by the fine scale parameterization. Previous studies have identified mixing processes in canyons as potentially important, possibly even dominant, in the abyssal ocean [Bryden and Nurser, 2003; Thurnherr et al., 2005; Thorpe, 2007]. These studies explain the observed high mixing rates in canyons by hydraulically controlled mixing at sill overflows, a process that is not captured by the fine scale parameterization.

Another mixing process that is not well captured by the fine scale parameterization is critical layer interaction with a sheared mean flow. In Chapter 5 we explore this process numerically. Observations in the Atlantis II FZ suggest that this process may be relevant to water mass transformation in this canyon [MacKinnon et al., 2008]. The contribution of this process to the Indian Ocean deep mixing budget may be considerable, because most bottom and deep waters appear to enter the basin through the Atlantis II FZ and the Melville FZ in the Southwest Indian Ridge [Warren, 1978; MacKinnon et al., 2008] or as deep boundary currents east of South Africa and east of Madagascar [Donohue and Toole, 2003; Bryden and Beal, 2001].

4.7 Summary and conclusion

The statistical exploration of fine scale dissipation estimates in this section discusses temporal variability and potential spatial biases. The ultimate aim of this section is to answer the question whether the Indian Ocean MOC, as inferred from large scale inverse models, can be sustained by internal wave breaking.

When comparing the 1996 and 2007 occupation of section I09N we found little variability, which suggests a more or less steady dissipation climate on a decadal time scale. The combination of measurements from different years, and perhaps also different seasons, seems therefore permissible.

Spatial biases may be significant when measurements are scarce or *not* randomly sampled with respect to the environmental variables that influence the internal wave field. We have investigated three such variables: latitude, bottom roughness, and energy conversion into internal tides. The sample set does not appear to be biased with respect to the latter two and we have estimated that the mean dissipation rate is biased low by at most 25% due to the latitudinal distribution of measurements.

The ultimate question, that is the hypothesis that the Indian Ocean MOC is sustained by internal wave breaking, is *not* supported by our analysis. We find that the energy in the internal wave field falls short. This result suggests that the closure of the Indian Ocean MOC needs other mixing processes that are not captured by the fine scale parameterization. One such process, that we think deserves special attention, is mixing in the numerous fracture zones by internal wave mean flow interaction.

Part II

Numerical simulations

Chapter 5

Dissipation of internal waves in a sheared mean flow

5.1 Introduction

This work is motivated by the observation of a strong and persistent jet flow through the Atlantis II Fracture Zone (AFZ) in the South West Indian Ridge (Fig. 5.1) [MacKinnon et al., 2008]. The jet flows northward through a submarine canyon with a typical width of 20 km and a length of about 200 km and has a maximum flow speed of about 0.4 ms^{-1}. The transport rate is about $3 \times 10^6 \mathrm{m}^3\mathrm{s}^{-1}$ and the water masses in the jet flow are identified as North Atlantic Deep Water, Circumpolar Deep Water and Antarctic Bottom Water.

A comparison of water properties at the entrance and exit of the canyon shows that water masses are mixed during the transit. The observed water mass transformation requires a mixing rate of about $K_\rho = 1 \times 10^{-2}$ $\mathrm{m}^2\mathrm{s}^{-1}$ below 2000m [MacKinnon et al., 2008], a factor 1000 larger than the generic open ocean value. This image of vigorous mixing of deep– and bottom

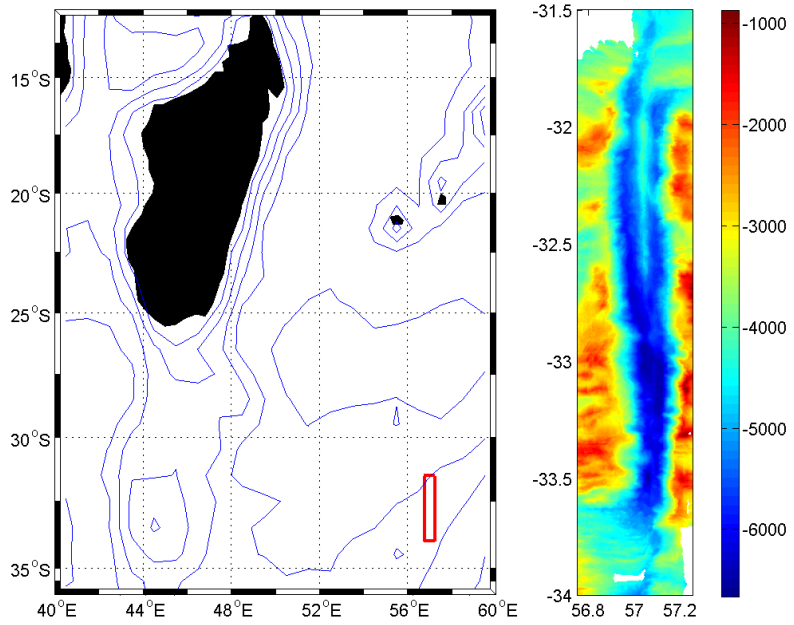

Figure 5.1: Location and bathymetry of Atlantis II Fracture Zone (AFZ). Left: map of the South-west Indian Ocean with a red square around the area of the AFZ and 1000m depth contours. Right: multi-beam bathymetry of the AFZ.

water is corroborated by the observation of large density overturns and high levels of shear variance.

The combination of large transport and vigorous mixing makes this site, and similar environments, potentially important for the Indian Ocean MOC. The estimated basin wide diapycnal transport in the Indian Ocean is about 10 Sv across an isopycnal in the range 27.5–28.0 [McDonagh et al., 2008; Bryden and Beal, 2001; Ganachaud and Wunsch, 2000]. The diapycnal transport in the AFZ is limited by the short residence time and the narrow extent of the canyon and has an estimated value of only 0.002 Sv across the 28.11 isopycnal [MacKinnon et al., 2008]. Canyons however are very numerous in the Indian Ocean. Collectively they could explain why much of the deep mixing in the global MOC appears to take place in the Indian Ocean.

Observations of turbulence and vertical diffusion in other abyssal passageways [Polzin et al., 1996; Ferron et al., 1998; St Laurent and Thurnherr, 2007] have led to speculation that much of the energy needed for deep ocean mixing is drawn from the mean flow by hydraulically controlled sill overflows [Thurnherr et al., 2005; Thorpe, 2007]. Here we explore an alternative explanation: internal wave instability due to interaction with the mean flow.

Internal wave breaking is a likely mixing mechanism in the AFZ, because the mean flow appears stable, $Ri = \langle N^2 \rangle / \langle U_z^2 \rangle \sim 10$, and not hydraulically controlled. Hydraulic jumps may occur downstream of sills if the flow has a Froude number close to one or larger. The typical Froude number for the jet in the AFZ is a factor 10 smaller than the critical value, $Fr = \langle U \rangle / \langle N \rangle / H \sim 0.1$. The geometry of the AFZ is not favourable to hydraulic jumps either, because there are only two sills, one at the entrance and one

at the exit. Hydraulic turbulence could be generated downstream of the entrance sill, but is not expected to dominate the mixing budget, because of the low Froude number [MacKinnon et al., 2008].

In this chapter we explore the dynamics of a broad band internal wave field in the presence of a mean flow by numerical integration of the fully nonlinear Navier-Stokes equations. We run a series of unforced initial value problems in 2D and 3D with simple boundary conditions, a constant density stratification, and a mean flow with a high bulk Richardson number and a low Froude number. We focus on the energy transfer rate to smaller scales and assume that the energy transferred to the smallest numerical scales is representative of the dissipation rate.

5.2 Conceptual model

In this section we review a few elementary concepts with regard to wave–mean flow interactions. The theory presented here is based on lecture notes from E. Kunze [Kunze, 2000]. It is assumed that the fast-scales and slow-scales can be treated as independent variables in the sense of the WKB ray-tracing approximation. This approximation is valid when the background mean flow has a large wavelength and a low frequency in comparison to the internal waves.

Suppose there is a steady mean flow with velocity $\mathbf{U} = (U, 0, 0)$ and a single plane wave with velocity $\mathbf{u} = \hat{\mathbf{u}} \exp[i(\mathbf{k} \cdot \mathbf{x} - \omega_i t)]$, with $\hat{\mathbf{u}}$ a vector with the velocity amplitudes in the three spatial directions, $\mathbf{k} = (k, l, m)$ the wave vector, and ω_i the intrinsic frequency. The intrinsic frequency is the frequency of the wave in a frame of reference that moves with the mean flow and does not change when the mean flow changes. On the contrary, the frequency in a fixed frame of reference,

that is the Eulerian frequency ω_E, is Doppler shifted when the wave is advected.

The Doppler relation can be derived using the total derivative of the velocity, $D_t(\mathbf{u}+\mathbf{U}) = [\partial_t + (\mathbf{u}+\mathbf{U})\cdot\nabla](\mathbf{u}+\mathbf{U})$. Ignoring self-advection of waves, $\mathbf{u}\cdot\nabla\mathbf{u} = 0$, wave advection of the mean flow, $\mathbf{u}\cdot\nabla\mathbf{U} = 0$, and using $\partial_t\mathbf{U} = \mathbf{0}$ and $\mathbf{U}\cdot\nabla\mathbf{U} = 0$, gives the Doppler relation,

$$\omega_i = \omega_E + kU(z) = constant, \tag{5.1}$$

with k the horizontal wave number.

Suppose a wave propagates into a mean flow (i.e. the vertical wave number m and the vertical gradient of the mean flow U_z have the same sign). The horizontal wavenumber of this wave is either be directed in the direction of the flow or against the flow. The sign of the horizontal wave number k matters for the 'direction' of the Doppler shift of ω_E (5.1) and below we discuss how the Doppler shift affects the vertical wave number and vertical group velocity.

Wave propagates *with* the flow ($kU > 0$) The relation between the Eulerian frequency and the wave numbers for linear internal waves is given by the dispersion relation (5.16). Substitution of the Doppler relation (5.1) into (5.16) and re-ordering terms, gives,

$$m^2 = \frac{N^2k^2 - (\omega_i - kU)^2k^2}{(\omega_i - kU)^2 - f^2}. \tag{5.2}$$

This relation for the vertical wave number is singular for $(\omega_i - kU)^2 - f^2 = 0$ or $U = U_{crit} = (\omega_i - f)/k$. In other words, the vertical wave number blows up when the wave reaches a *critical level* in the mean flow.

Using the definition of the horizontal phase speed,

$c \equiv \omega_i/k$, we find,

$$U_{crit} = c - \frac{f}{k}. \tag{5.3}$$

Because both $f > 0$ and $kU > 0$ we note that a critical level exists when the horizontal phase speed is smaller than the maximum flow speed.

The vertical wave length, $\lambda_z = 2\pi/m$, goes to zero, when $m \to \infty$. This means that the energy of a wave approaching a critical layer becomes concentrated in increasingly smaller-scale vertical motions. The high vertical shear associated with these small-scale motions would lead to strong damping by molecular *dissipation* in a viscous fluid. Conceptually, we may therefore regard a critical layer as a sink for internal waves.

It is also instructive to see what happens to the vertical group velocity, $\frac{\partial \omega_E}{\partial m}$ when $m \to \infty$. The dispersion relation (5.16) can be approximated by $\omega_E^2 \approx f^2 + N^2K^2/m^2$ when $m \gg k$, and we find,

$$\frac{\partial \omega_E}{\partial m} \approx -\frac{N^2k^2}{fm^3}, \tag{5.4}$$

for the vertical group velocity. Clearly, $\lim_{m\to\infty} \frac{\partial \omega_E}{\partial m} = 0$, that is the *wave stalls* when approaching a critical level.

Summary: There is a critical level for a wave propagating into a the mean flow, when (i) the wave propagates in the same direction as the mean flow, and (ii) the horizontal phase speed is smaller than the maximum mean flow speed. The fate of a wave approaching a critical layer is catastrophic in the sense that it stalls and dissipates its energy, and thus ceases to exist.

Wave propagates *against* the flow ($kU < 0$) The Doppler shift of ω_E is towards higher frequencies when $kU < 0$ (refer to (5.1)). The dispersion relation (5.16)

shows that high frequency internal waves have a large aspect ratio, that is $k \gg m$. In this limit we may approximate the dispersion relation by, $\omega_E^2 \approx f^2 m^2/k^2 + N^2$ or

$$m^2 \approx \frac{k^2}{f^2}((\omega_i - kU)^2 - N^2), \tag{5.5}$$

after substitution of the Doppler relation. This equation has no singularities, but becomes zero and changes sign for increasing mean flow speed, U. We find $m = 0$ for $(\omega_i - kU)^2 - N^2 = 0$ and define the *turning point* as,

$$U_{turn} = c - \frac{N}{k}, \tag{5.6}$$

In analogy to the critical layer we note that a turning point exists for a wave propagating against the flow with a horizontal phase speed smaller than the maximum flow speed.

The vertical group velocity in the $k \gg m$ limit is,

$$\frac{\partial \omega_E}{\partial m} \approx \frac{f^2}{Nk^2} m. \tag{5.7}$$

Thus, we find $\lim_{m\to 0} \frac{\partial \omega_E}{\partial m} = 0$, that is the vertical group velocity goes to zero when a wave reaches the turning point. The wave energy is conserved, because the vertical shear decreases (since $m \to 0$). Note that further propagation of the wave energy can only be directed in the opposite direction, towards lower mean flow speeds.

Summary: There is a turning point for a wave propagating into a the mean flow, when (i) the wave propagates in the opposite direction of the mean flow, and (ii) the horizontal phase speed is smaller than the maximum mean flow speed. A wave approaching a turning point reverses its vertical direction of propagation without loss of energy.

Discussion This basic theory on wave–mean flow interaction does not represent all the physics of a real fluid, but captures the essential behaviour. The predicted singularities at the critical level and turning point are obviously unphysical and emerge because the theory lacks a dissipation mechanism. The theory breaks down when scales are not separable, for example when the internal wave lengths are similar to the length scale of the mean flow. Some phenomena are not captured at all, such as partial reflection and transmission (tunneling) at a critical level.

5.3 Numerical model

5.3.1 Model equations

The numerical model used in this study is a pseudo-spectral algorithm for finding approximate solutions to the Navier–Stokes equations for an incompressible, density stratified fluid on a f-plane. Decomposing the density field into a reference value, a background field, and a fluctuating component, $\rho = \rho_0 + \bar{\rho}(z) + \rho'(x, y, z, t)$, and invoking the Boussinesq approximation[1] we obtain

[1]The Boussinesq approximation assumes that inertial density fluctuations can be neglected (and replaced with the reference value ρ_0). However, fluctuations of the gravitational density are dynamically important and remain unaffected in this approximation.

the following form for equations of motion,

$$\frac{Du}{Dt} = -\frac{1}{\rho_0}\frac{\partial p}{\partial x} + fv - \mathcal{D}u \qquad \text{(zonal momentum)} \tag{5.8}$$

$$\frac{Dv}{Dt} = -\frac{1}{\rho_0}\frac{\partial p}{\partial y} - fu - \mathcal{D}v \qquad \text{(meridional momentum)} \tag{5.9}$$

$$\frac{Dw}{Dt} = -\frac{1}{\rho_0}\frac{\partial p}{\partial z} + b - \mathcal{D}w \qquad \text{(vertical momentum)} \tag{5.10}$$

$$\frac{Db}{Dt} = -N^2 w - \mathcal{D}b \qquad \text{(buoyancy)} \tag{5.11}$$

$$\nabla \cdot \mathbf{u} = 0 \qquad \text{(continuity)} \tag{5.12}$$

where we used D/Dt as a shorthand for the 'material derivative' along the fluid parcel trajectory, for example $Du/Dt = \partial u/\partial t + \mathbf{u}\cdot\nabla\mathbf{u}$. The buoyancy frequency squared is defined as $N^2 = -g\rho_0^{-1}\bar{\rho}_z$ and the symbol $\mathcal{D}$ represents diffusion of momentum / buoyancy (refer to Section 5.3.2), where buoyancy is defined as $b = -g\rho_0^{-1}\rho'$.

The algorithm Fourier transforms the momentum equations and calculates the derivatives in spectral space. This is efficient and accurate for simple boundary conditions[2], because differentiation reduces to scalar multiplication in spectral space, $(\partial_x, \partial_y, \partial_z) \to (ik, il, im)$. More details about the model can be found in [Winters et al., 2004].

5.3.2 Numerical viscosity

Kinetic energy in the ocean cascades to smaller scales and ultimately to internal energy (i.e. heat) through

[2]Boundary conditions are either triple periodic or double periodic with a rigid lid and flat bottom.

molecular viscosity. Scales at which energy is dissipated are of the order of the Kolmogorov length scale, which is typically orders of magnitude smaller than the numerical grid spacing. This poses a numerical problem, because transfer of energy to sub grid-size length scales leads to numerical instability.

This problem is solved by damping momentum and buoyancy at high wavenumbers close to the numerical cut-off. Selective damping of high wavenumbers, without affecting the dynamics at larger scales, is achieved by a higher order viscosity operator,

$$\mathcal{D} = \left[\nu_x \frac{\partial^p}{\partial x^p} + \nu_y \frac{\partial^p}{\partial y^p} + \nu_z \frac{\partial^p}{\partial z^p} \right]. \tag{5.13}$$

This operator reduces to Newtonian viscosity for $p = 2$ (and $\nu = 10^{-6}$ m^2 s^{-1} for water), but becomes a 'hyperviscosity' with higher order derivatives, with $p > 2$. In the model we use $p = 10$.

The wavenumber range at which hyperviscosity becomes dynamically important can be tuned with the value chosen for the viscosity coefficient ν [m^p s^{-1}]. The actual tuning parameter in the model is the characteristic damping timescale at the Nyquist wavenumber, $T_{diss} = \nu_x^{-1} L_x \pi^{-1} n_x^{-1}$, with n_x the number of grid points and L_x the horizontal domain size.

Figure 5.2 shows the magnitude of the hyperviscosity term in the non-dimensionalized Fourier transformed equations of motion, $\nu U_0^{-1} L^{-p+1} k^p$. The plot shows that hyperviscosity acts on higher wavenumbers for increasing T_{diss}. Viscosity becomes dynamically important when it reaches the magnitude of the Coriolis acceleration, which in its nondimensionalized form is the inverse Rossby number, as indicated in the figure. The dynamics at smaller wavenumbers are essentially inviscid / nondiffusive, because of the strong scale dependency of the hyperviscosity operator.

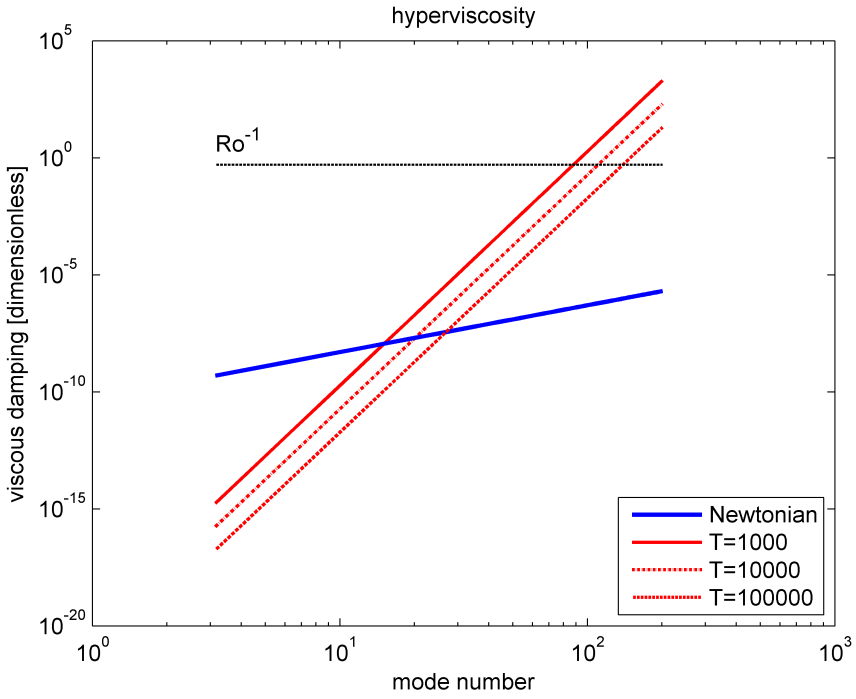

Figure 5.2: Magnitude of the hyperviscosity term in the non-dimensionalized Fourier transformed equations of motion, with characteristic units $L_z = 4000\text{m}$ and $U_0 = 0.1\text{ms}^{-1}$, and hyperviscosity order $p = 10$, and various values for T_{diss}. For reference are also plotted the Newtonian viscosity, $\nu U_0^{-1} L_z^{-1} k^2$ (with $\nu = 10^{-6}$ m^2 s^{-1}), and the inverse Rossby number, $Ro^{-1} = f L_z U_0^{-1}$.

The hyperviscosity operator has the sole purpose of taking energy out of the system at the smallest numerical scales and works indiscriminately on momentum (kinetic energy) and buoyancy (potential energy). Damping of buoyancy means that density perturbations are not allowed to develop at high wavenumber, because $b = -g\rho_0^{-1}\rho'$, but the molecular diffusion of the background density field is in fact retained in the model equations. In other words there is a term $-\kappa\partial^2\bar{\rho}/\partial z^2$ in the density equation. This term however is zero for the experiments discussed here because the stratification is constant (refer to Section 5.7 for a discussion about internal wave breaking and mixing).

The hyperviscosity is ad hoc in the sense that it does not describe actual physics. However, the representation of internal dissipation by hyperviscosity is justified under the assumption that (i) upscale transfer of energy is negligible [McComas and Müller, 1981], and (ii) internal waves break locally. The validity of the first assumption was demonstrated for vertical wavelengths of 5m by [McComas and Müller, 1981] and the second assumption relies on the observation that the product of the internal wave interaction time scales and the group velocity is small.

5.4 Initial conditions

5.4.1 Linear plane waves

The temporal and spatial oscillation of a single plane wave with wave vector $\mathbf{k} = (k, l, m)$ and frequency ω_i is prescribed by,

$$[u, v, w, p, b](x, y, z, t) = [\hat{u}, \hat{v}, \hat{w}, \hat{p}, \hat{b}]e^{i(\mathbf{k}\cdot\mathbf{x}-\omega_i t)}, \tag{5.14}$$

where (u, v, w) is the full velocity, p pressure and b buoyancy. This wave is a solution to the linearized,

rotating, density stratified, incompressible, inviscid, Boussinesq equations of motion, that is (5.8)–(5.12) with $\mathcal{D} = 0$ and $\mathbf{u} \cdot \nabla \mathbf{u} = 0$, when the polarization relations are satisfied. The polarization relations are obtained by plugging (5.14) into the equations of motions (5.8)–(5.12), giving a set of homogeneous linear equations,

$$M\mathtt{v} = \begin{bmatrix} -i\omega_E & -f & 0 & ik & 0 \\ f & -i\omega_E & 0 & il & 0 \\ 0 & 0 & -i\omega_E & im & -1 \\ 0 & 0 & N^2 & 0 & -i\omega_E \\ ik & il & im & 0 & 0 \end{bmatrix} \begin{pmatrix} \hat{u} \\ \hat{v} \\ \hat{w} \\ \hat{P} \\ \hat{b} \end{pmatrix} = 0, \tag{5.15}$$

where $\hat{P} = \rho_0 \hat{p}$.

Gaussian elimination shows that a non-trivial solution exists and that there is *one* independent variable. This means that we may eliminate all property amplitudes except for example $\hat{w}$. The existence of a non-trivial solution also implies that the determinant must be equal to zero. Solving $\det(M) = 0$ gives the internal wave dispersion relation [Kunze, 2000],

$$\omega_E^2(k, m) = \frac{f^2 m^2 + N^2(k^2 + l^2)}{k^2 + l^2 + m^2}. \tag{5.16}$$

5.4.2 Boundary conditions

The boundary conditions we used are periodic in both horizontal directions. This means that all discrete wave numbers smaller than the Nyquist wave number fit in the domain, that is, $(k, l) = (i/L_x, j/L_y)2\pi$ with $i \in [0, 1, 2, \ldots, n_x/2]$, and $j \in [0, 1, 2, \ldots, n_y/2]$. At the top and bottom of the domain we impose 'rigid lid' and 'free slip' conditions,

$$w(z = 0, L_z) = b(z = 0, L_z) = 0, \tag{5.17}$$

and from continuity follows, $u_z(z = 0, L_z) = v_z(z = 0, L_z) = 0$. The non-zero horizontal flow is assumed to slip freely (i.e. frictionless) along the boundaries.

The vertical boundary conditions are met by vertically standing modes. These modes can be constructed by subtracting identical waves that differ only by the direction of vertical propagation (so only the sign of m differs). Introducing a localization function $F(z)$, we obtain the following solution for a free slip linear wave in a frame of reference with arbitrary horizontal directions (and m parallel to z),

$$u = \hat{\xi}\omega \left(\frac{km}{k_H^2}\right) \left[\cos(kx + ly - \omega t) - \left(\frac{l}{k}\right)\left(\frac{f}{\omega}\right)\sin(kx + ly - \omega t)\right] G(z), \tag{5.18}$$

$$v = \hat{\xi}\omega \left(\frac{lm}{k_H^2}\right) \left[\cos(kx + ly - \omega t) - \left(\frac{k}{l}\right)\left(\frac{f}{\omega}\right)\sin(kx + ly - \omega t)\right] G(z), \tag{5.19}$$

$$w = \hat{\xi}\omega \sin(kx + ly - \omega t) F \sin(mz), \tag{5.20}$$

$$\xi = \hat{\xi} \cos(kx + ly - \omega t) F \sin(mz), \tag{5.21}$$

with $\hat{\xi}$ the wave displacement amplitude, $k_H = \sqrt{k^2 + l^2}$ is the horizontal wave number and $G(z) = [F\cos(mz) + \frac{F'}{m}\sin(mz)]$.

5.4.3 GM76 wave amplitudes

The GM76 spectrum

The Garret-Munk spectrum [Garrett and Munk, 1972, 1975] assumes that spectral energy dependency on frequency and vertical mode number is separable,

$$E(\omega, j)\, d\omega\, dj = E_0\, B(\omega) d\omega\, H(j) dj \quad \text{[dimensionless]}, \tag{5.22}$$

with vertical mode number j and frequency ω. The model is a power law fit to ocean observations con-

sistent with linear internal wave theory. Time and length scales are non-dimensionalized using an idealized buoyancy frequency profile, $N(z) = N_0 e^{-z/d}$, with N_0 = 3cph= $5.2\,10^{-3}$rad s^{-1} and fall-off scale $d = 1300$m. Multiplication of (5.22) by $N_0^2 d^2$ gives the dimensional spectrum in Joules per kg (i.e. m^{2}s^{-2}). Model constants, such as the energy level, $E_0 = 6.3\,10^{-5}$, and the frequency and modal scaling are obtained from a least square fit to observational data.

The frequency dependency is proportional to $1/\omega^2$ for high frequencies ($\omega \gg f$) and peaks around the inertial frequency (with a singularity at $\omega = f$) [Garrett and Munk, 1975],

$$B(\omega) = \frac{2}{\pi} \frac{f}{\omega(\omega^2 - f^2)^{1/2}} \qquad \text{[s]}. \qquad (5.23)$$

This representation of the internal wave field captures the general frequency dependency as it is observed in the ocean, but lacks more detailed features such as the spectral peaks at tidal frequencies. The normalization is chosen such that $\int_f^N B(\omega) d\omega \approx 1$.

The dependency on vertical modes also scales with the inverse square for large modes ($j \gg j*$), but is flattened for modes close to the modal scale number, $j* = 3$,

$$H(j) = \frac{(j^2 + j*^2)^{-1}}{\sum_{j=1}^{j_{max}} (j^2 + j*^2)^{-1}} \quad \text{[dimensionless]}. \quad (5.24)$$

The j^{-2} scaling for large j was proposed by [Cairns and Williams, 1976] differs from the $j^{5/2}$ scaling in [Garrett and Munk, 1975]. This form for $H(j)$ together with (5.22) is referred to as GM76.

Transformation to wave number space

The GM76 spectrum is originally formulated in frequency–mode number space, but can be transformed to wave number–mode number space using the dispersion relation. The energy in (k, j) space is related to the GM76 spectrum through $E(k, j) = E(\omega, j)\, d\omega\, dk^{-1}$, so that the total energy is the same in both spaces, $\int d\omega \sum_j E(\omega, j) = \int dk \sum_j E(k, j)$. Using the linear dispersion relation (5.16) in the $\omega \ll N$ approximation gives,

$$E(k, j)\, dk\, dj = E(\omega, j) \frac{N(\omega^2 - f^2)^{1/2}}{m\omega}\, dk\, dj, \quad \text{[dimensionless]}, \tag{5.25}$$

with $m = j\frac{\pi}{L_z}$, and L_z the vertical domain size [Flatté et al., 1979].

Wave amplitudes

The polarization relations (5.18)–(5.21) and $\hat{b} = -N^2\hat{\xi}$ allow to write the amplitudes of all wave property amplitudes in terms of the displacement amplitude. This means that the displacement amplitude for a set of wave numbers (k, l, m) can be solved for a given spectral energy level. Kinetic wave energy is contained in motion of water parcels and potential energy in the displacement of isopycnals,

$$E_k = \frac{1}{2}[\hat{u}^2 + \hat{v}^2 + \hat{w}^2] \qquad [\mathrm{m^2 s^{-2}}], \tag{5.26}$$

$$E_p = \frac{1}{2}\hat{\xi}^2 N^2 \qquad [\mathrm{m^2 s^{-2}}], \tag{5.27}$$

where the hatted quantities, $(\hat{u}, \hat{v}, \hat{w})$, are velocity amplitudes and $\hat{\xi}$ the displacement amplitude. A generic open ocean value for the spectral energy density $[\mathrm{m^2 s^{-2}}]$ is provided by (5.25) multiplied by $N_0^2 b^2$. Plugging the polarization relations into (5.26) and (5.27) and

rewriting using the dispersion relation gives,

$$\hat{\xi}(k,j) = \frac{\sqrt{E(k,j)\,dk\,dj\,N_0^2 b^2}}{\omega}\left(\frac{\omega^2 - f^2}{N^2 - f^2}\right)^{\frac{1}{2}} \quad [\mathrm{m}], \tag{5.28}$$

for the displacement amplitude in meters.

5.4.4 Ambient shear flow

The ambient shear flow flows in the x-direction, is uniform in the y-direction and has a hypertangent profile in the z-direction (parallel to gravity),

$$U(z) = \frac{U_0}{2}[\tanh(\frac{2}{d}(-z + \frac{L_z}{3})) + 1], \tag{5.29}$$

with U_0 the maximum mean flow speed, d the vertical scale length, and L_z the vertical domain size. This analytical form has a number of desirable characteristics, among which are satisfaction of the no-slip boundary condition, $U_z(0) \approx 0$ and $U_z(L_z) \approx 0$, and a single, well defined shear region.

The maximum flow velocity is U_0. All waves with horizontal group velocities smaller than U_0 will eventually meet a critical layer and either stall or reflect. These encounters take place mostly in the bottom half of the domain because the maximum vertical shear is at $L_z/3$. Waves in the upper half of the domain are hardly affected by the mean flow.

The vertical scale parameter d determines the extent of shear zone and needs to be smaller than $\sim L_z/3$ to satisfy the boundary conditions. The parameter d determines the predominant shear of the mean flow. In fact, the shear is U_0/d in the vicinity of the depth of maximum shear, i.e. $L_z/3$, as can be seen from expanding $U(z)$ around this depth, $U(z') = U_0/2 - (U_0/d)z' - O(z'^2)$.

The shear is U_0/d or less and the stratification is

constant ($N = 5.2\,10^{-3}$ rad s^{-1}), which means that the Richardson number is larger than $N^2 d^2/U_0^2$. To avoid mean flow shear instabilities we choose Ri$>$ 0.25, or equivalently $d/U_0 > \sqrt{0.25}/N > 96$. We also check the stability of the mean flow more directly by initializing the model with the mean flow only, without internal waves (refer to Section 5.6.1).

This study focusses on the effect of the mean shear flow on internal waves. In this context we prefer a steady mean flow and consider effects of rotation undesirable. Therefore we envision a non-rotating mean flow as if it were confined by the walls of a straight canyon in the x-direction. In a canyon the Coriolis force would have been balanced by a pressure gradient, but this cannot be done in 2D experiments and it is not easily set up in 3D either when using a spectral model.

Therefore we choose to disable rotation for the background flow only by disallowing temporal evolution of $k = 0$ and $m = 0$ terms in the Fourier transformed equations of motion. This means that we also prohibit changes in the mean flow due to momentum transfer from the wave field, which we again justify by our aim of studying the effect of the mean flow on internal waves. Note however that the dynamics of the internal waves are unaffected because all wave numbers larger than zero evolve according to the full momentum equations with rotation.

5.5 Diagnostics

5.5.1 Energetics

A useful bulk diagnostic is the total energy in the internal wave field,

$$E = \overline{E_k} + \overline{E_p}, \quad [\mathrm{m^2 s^{-2}}] \tag{5.30}$$

$$\overline{E_k} = \frac{1}{2}\frac{1}{V}\int (u-U)^2 + v^2 + w^2 \, dV, \tag{5.31}$$

$$\overline{E_p} = \frac{1}{2}\frac{1}{V}\int N^2 \xi^2 \, dV, \tag{5.32}$$

with $V = L_x \times L_y \times L_z$ the domain volume, $U = U(z)$ the mean flow speed, (u, v, w) the full internal wave velocity, and ξ the wave displacement. The potential energy (E_p) is the available potential energy in the internal wave field due to the displacement of isopycnals. We derive the displacement from the perturbation density, $\xi = \rho'/\rho_z$, which is almost exact for the virtually mixing free problems discussed here (refer to Section 5.7). Available potential energy can be calculated for problems with mixing by introducing the concept of background potential energy [Winters et al., 1995].

5.5.2 Hyperdissipation

Hyperdissipation is the local irreversible loss of kinetic energy due to hyperviscosity (refer to Section 5.3.2). The rate of kinetic energy loss can be derived from the momentum equation (5.8)–(5.12) by taking the inproduct with velocity, $E_t = \mathbf{u}_t \cdot \mathbf{u}$. A hyperviscosity of the form (5.13) gives a dissipation rate [MacKinnon, 2003],

$$\epsilon = \sum_i \sum_j \nu_j \left[\frac{\partial}{\partial x_j}^{p/2} u_i \right]^2 . \tag{5.33}$$

The hyperdissipation rate is conveniently calculated in Fourier space, where taking the spatial derivative

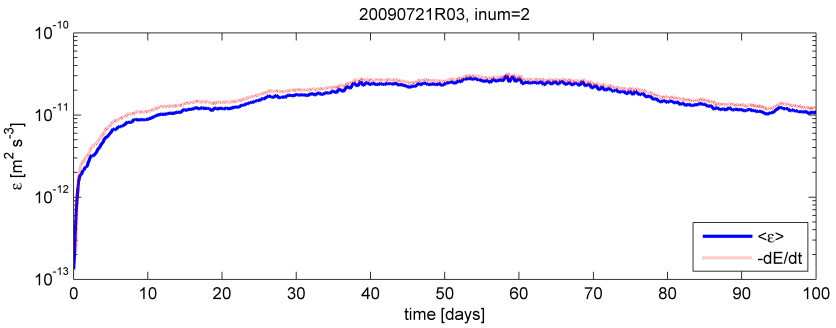

Figure 5.3: Comparison of hyperdissipation (5.33) and the loss rate of total energy dE/dt (refer to (5.31) and (5.32)). The simulation is initialized with a broadband GM-like wave field without a mean flow.

becomes multiplication by wave number. Figure 5.3 compares the dissipation rate calculated directly from the total energy, $\epsilon = dE/dt \approx \Delta E/\Delta t$, and the hyperdissipation rate.

5.6 Numerical experiments

5.6.1 Mean flow stability

In this study we look at the transfer of internal wave energy to dissipative scales in the presence of a mean shear flow. The mean flow itself is designed to be stable, in the sense that shear instabilities are sufficiently suppressed by the density stratification so that the flow is essentially laminar. The design criterion is $Ri = N^2/U_z^2 > 0.25$. To test the usefulness of this criterion we simulate the temporal evolution of the mean flow only, without internal waves.

We use the numerical dissipation rate to diagnose the stability of the mean flow and we compare three different mean shear flows. Each model run is initialized with a hypertangent mean flow profile, as described in Section 5.4.4, and numerically integrated over 10 days. The dissipation rate is averaged along the horizontal dimension and over time from day 9

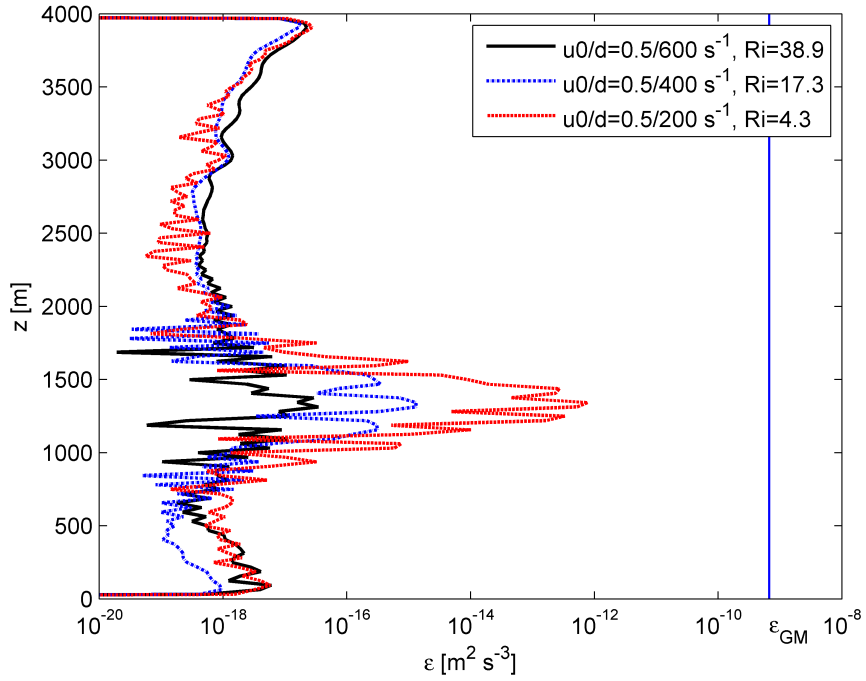

Figure 5.4: Horizontally averaged dissipation profiles for three different mean flows *without* internal waves. The maximum flow speed is 0.5 ms^{-1} for all three cases, but the shear differs, and therefore also the bulk Richardson number $Ri = N^2/U_z^2 \approx d^2N^2/U_0^2$. The straight blue line is a reference showing the GM dissipation level for free waves.

until 10.

Figure 5.4 compares the dissipation profile for flows with identical maximum flow speeds of $U_0 = 0.5$ ms^{-1} and different vertical sales. For reference we recall that the dissipation rate of the generic Garrett–Munk internal wave field is $\epsilon_0 = 6.73 \times 10^{-10}$ $\mathrm{m}^2\mathrm{s}^{-3}$. The dissipation rate of the mean flow is orders of magnitude smaller than this value, even for the flow with the largest vertical shear and a Richardson number of order 1.

	I	II		
L_x	35000	1700	m	Domain size, x direction
L_y	0	0		Domain size, y direction
L_z	4000	4000	m	Domain size, z direction
k	$2\times\frac{2\pi}{L_x}$	$[2,\pm3]\times\frac{2\pi}{L_x}$	rad m^{-1}	Wave number, x direction
l	–	–		Wave number, y direction
m	$8\times\frac{2\pi}{L_z}$	$[8,12]\times\frac{2\pi}{L_z}$	rad m^{-1}	Wave number, z direction
N	0.0052	0.0052	rad s^{-1}	Buoyancy frequency[a]
f	1.3×10^{-5}	1.3×10^{-5}	rad s^{-1}	Inertial frequency[b]
n_x	64	64		Grid points, x direction
n_y	1	1		Grid points, y direction
n_z	64	64		Grid points, z direction
Δt	10	1	s	Integration time step
t_{end}	12.5	12.5	hr	Integration time
p	10	10		Hyperviscosity coefficient
T_{diss}	100	100	s	Hyperviscosity time scale

Table 5.1: Model parameters for single wave (I) and two wave (II) simulations.

[a] Buoyancy frequency is the canonical GM value of 3 cycles per hour.
[b] Inertial frequency corresponds to a latitude of 33°.

5.6.2 Single wave

This simulation provides some basic insight into the dissipation of a single wave approaching a critical level. The mean shear flow is expected to compress the vertical length scale until the wave has dissipated its energy due to numerical viscosity. We assess how the vertical dissipation profile is affected by the amplitude of the wave and the shear of the mean flow.

The parameters for the single wave experiment, which we refer to as 'simulation I', are listed in Table 5.1. The initial wave packet is confined to the top of the domain using an exponential envelope function $F(z) = \exp[-(z - L_z)^2/d^2]$ with fall-off scale $d = L_z/10$. Figure 5.5 shows snapshots of the free evolution of the wave packet without a mean flow. The vertical velocity is shown in the top four panels and the bottom panels show the vertical velocity spectrum.

Note that the vertical mode number counts the number of *half* wave lengths that fit into the domain and the horizontal mode number the number of full wave lengths.

The evolution of the modal spectrum differs for both modal directions. The energy remains in the 2nd horizontal mode during the 12.5 hr evolution, but there is energy exchange between the vertical modes. At $t = 0$ the energy is spread out over many vertical modes with a maximum around the 13-th vertical mode, although the initial vertical mode is 16. This can be explained by the spatial localization of the initial wave. After four hours of free wave propagation we see that vertical mode 16, and neighbouring modes, indeed contain most energy. The snapshot after eight hours shows two distinct spectral peaks at vertical mode 12 and 17 and after 12 hours the bulk of the energy has moved to vertical mode 14. Energy transfer between modes can occur when a wave interacts with its own reflection from the top and bottom of the domain.

Figure 5.6 shows the time evolution of single wave in the presence of a mean flow, refer to simulation I in Table 5.1. The wave propagates freely until it encounters the mean shear flow in the bottom half of the domain. The top panels of Fig. 5.6 show that the wave hardly propagates below the critical level, which is the white line in the figure. The critical level is the depth where the mean flow speed equals, $U_c = (\omega_i - f)/k = 0.38$ ms^{-1}.

The spectral picture at the bottom of Fig. 5.6 shows that the energy gradually moves towards higher vertical modes when the wave approaches the critical level. Waves are numerically damped when the vertical length scale becomes sufficiently small. This effect is demonstrated in the right panel of Fig. 5.7, which shows the

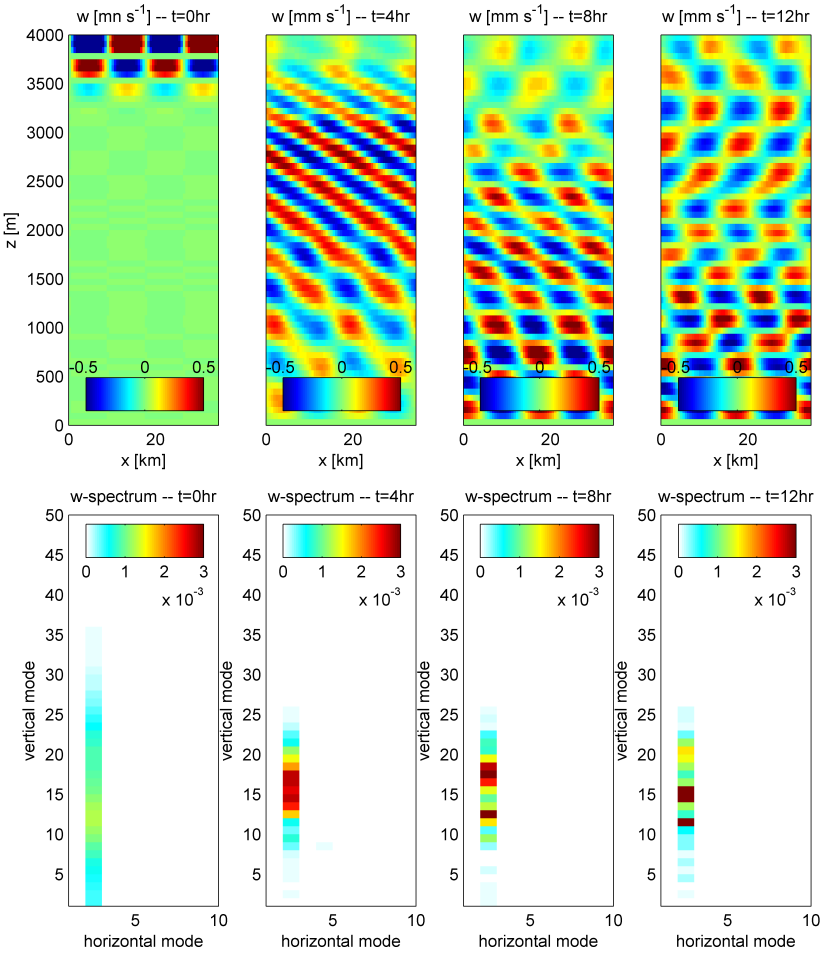

Figure 5.5: Time evolution of a single wave packet without a mean flow. The wave is initialized with modes $[ik, im] = [2, 8]$, displacement amplitude $\xi = 10$m. Top row: four snapshots of the vertical velocity with a variable colour scale in mms^{-1}. Bottom row: vertical velocity spectrum. The time interval between each snapshot is 4 hours.

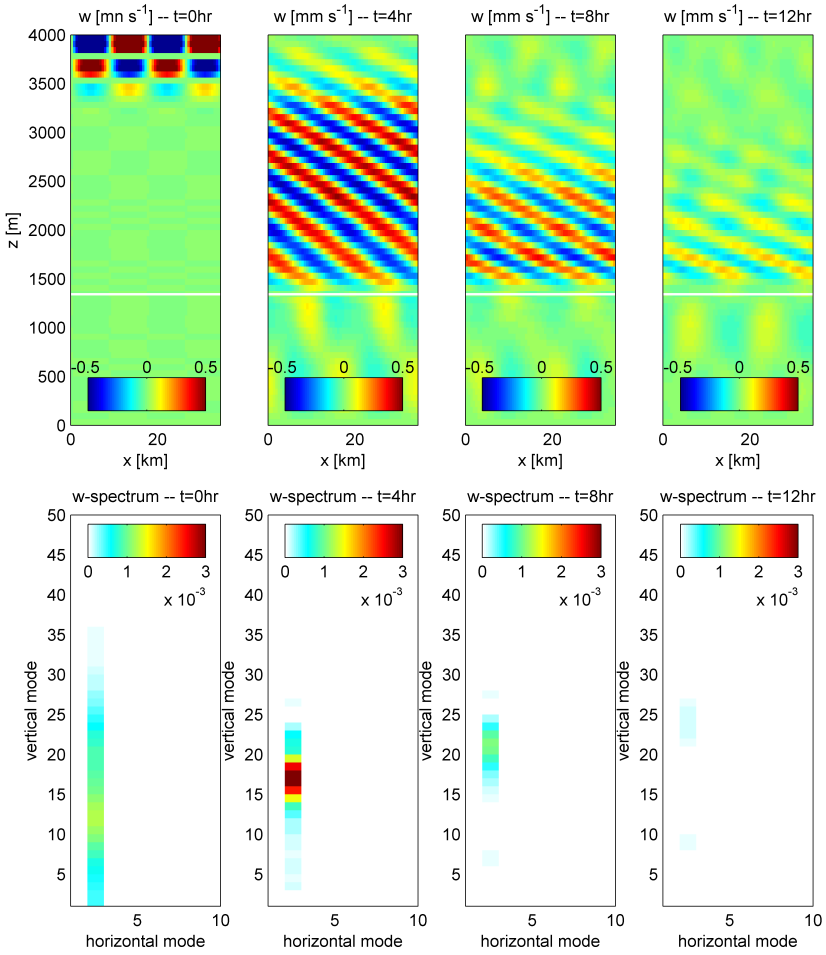

Figure 5.6: Time evolution of a single wave packet with a mean flow and a critical layer. The wave is initialized with modes $[ik, im] = [2, 8]$, with displacement amplitude $\xi = 10$m and the mean flow parameters are $U_0 = 0.8\text{ms}^{-1}$, and $d = 400$m. Top row: four snapshots of the vertical velocity with a variable colour scale in mms^{-1}. Bottom row: vertical velocity spectrum. The time interval between each snapshot is 4 hours. The white line indicates the critical level for the initial wave (refer to Table 5.1).

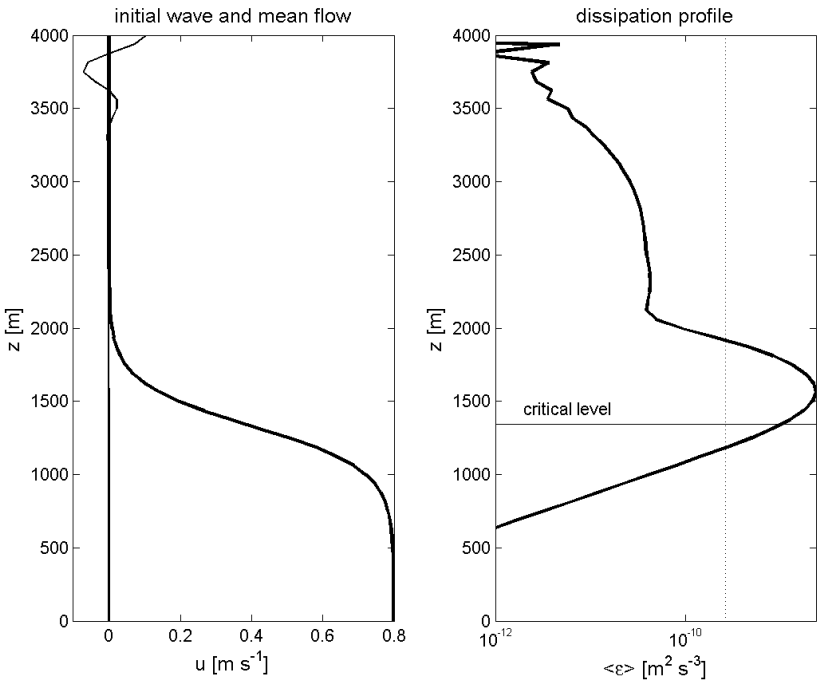

Figure 5.7: Vertical profiles of velocity and dissipation for the single wave simulation. Left panel: mean shear flow (thick) and wave velocity (thin) at t=0. Right panel: dissipation spatially averaged in the x-direction and temporally averaged over 11 hours (thick), and the 'half maximum' value as defined in Section 5.6.2 (dotted). The wave amplitude is 20 m and the shear parameters are $U_0 = 0.8$ m s^{-1} $d = 600$ m.

spatially and temporally averaged dissipation rate for a simulation similar to the one shown in Fig. 5.7, but with $d = 600$m instead of $d = 400$m. The right panel of Fig. 5.7 shows how the mean shear increases the dissipation rate until it reaches a maximum at some distance above the critical level.

Most wave energy is dissipated in the mean shear region with maximum dissipation rates at a distance of a few hundred meters above the critical level. The magnitude of the maximum depends on the energy of the initial wave and scales quadratically with the displacement amplitude as one would expect from (5.28). However, the left panel of figure 5.8 shows the scaling

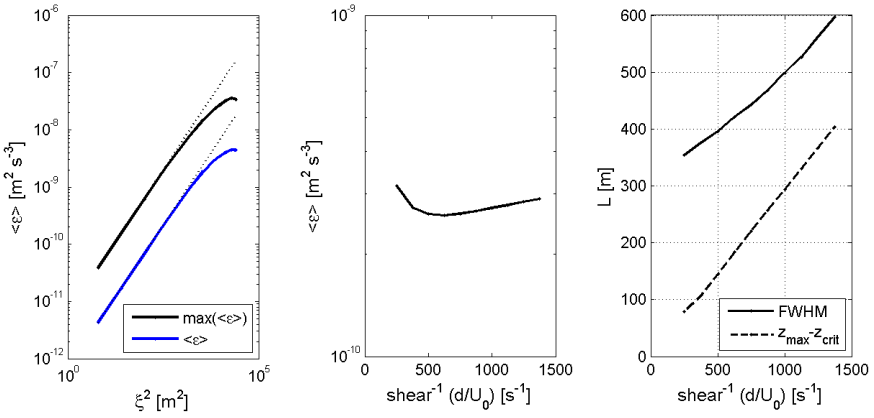

Figure 5.8: Exploration of the single wave parameter space. Dissipation rates are averaged over the entire spatial domain and in time between 5.6 and 12.5 hr. Left: dissipation/energy scaling ($E \propto \xi^2$), with mean flow parameters: $U_0 = 0.8\text{ms}^{-1}$, and $d = 600\text{m}$. Middle: dissipation versus mean flow shear, with $\xi = 20\text{m}$, and $U_0 = 0.8$ m s^{-1}. Right: width of dissipation peak versus mean flow shear, with $\xi = 20\text{m}$, and $U_0 = 0.8\text{ms}^{-1}$.

becomes smaller than quadratic for very large amplitudes, which we attribute to non-linearity of the free wave and loss of energy before it reaches the mean shear zone.

The fact that the dissipation peak is *above* the critical layer can be explained by the finite dissipation length scale of both real and numerical waves. The critical level value is obtained from WKB ray tracing theory and predicts the unphysical value of zero for the wavelength at the critical level. Real waves become unstable at scales of order 1 meter and numerical waves are dissipated at scales close to the Nyquist wave length, which is typically 30m for the experiments discussed here.

The dashed line in the right panel of Fig. 5.8 shows that the distance from the dissipation maximum to the critical level scales almost linearly with the shear scaling parameter d and increases for larger values of d. This behaviour can be explained by the quasi-linearity

of the hyper-tangent profile in the proximity of $U_0/2$. Numerical waves dissipate at some finite wave length at some distance from the critical level, and this distance scales quasi-linearly with the mean flow inverse-shear parameter d.

Most energy is dissipated above the critical level, but some energy makes it past this level (again refer to right panel of Fig. 5.8) and shows that *total* stalling, as predicted by ray tracing theory, is not a reality. The dissipation peak is surprisingly symmetric around its maximum. This allows us to define the width of the dissipation peak. We define the Full Width at Half Maximum (FWHM) with the 'half maximum' given by $(\epsilon_{max} - \langle\epsilon(z)\rangle)/2$, and $\langle . \rangle$ the vertical average operator. Figure 5.8 shows the FWHM of the dissipation peak versus shear parameter d and reveals a quasi-linear relation.

5.6.3 Two waves

In this simulation we investigate the basic effect of non-linearity on wave dissipation. We compare the dissipation of two separately evolving waves with a simulation initialized with two waves with the same wave numbers. The wave– and numerical parameters for this experiment are summarized in column II of Table 5.1.

We have run two simulations initialized with two waves localized at the top of the domain. The wave numbers for one simulation are chosen so that there is a critical level for each of them. The other simulation has a critical level for the wave propagating with the flow and a turning point for the wave going against the flow. The critical flow velocity and the turning velocity for the initial waves are given by, $U_{crit} = (\omega_i - f)/k$ and $U_{turn} = (N - \omega_i)/k$, and fall within the range of quasi-linear mean flow shear (refer to Section 5.4.4).

Two critical waves The time evolution of two critical waves is shown in Fig. 5.9. The top panels show snapshots of the vertical velocity and the bottom panels show the evolution of the modal spectrum. The total kinetic energy, E_k, is also shown in the bottom panels as a percentage of the energy at $t = 0$ and shows that more than 80% of the energy is dissipated in the course of the 12 hour experiment.

Based on the theory presented in Section 5.2 we expect spectral transfer of energy to higher vertical modes when the waves approach the critical layers. Indeed, the critical wave with $[ik_1, im_1] = [2, 16]$ quickly transfers energy to higher vertical modes around $im = 22$. This wave has dissipated almost all its energy after 8 hours. The modal evolution of the other wave, with $[ik_2, im_2] = [3, 24]$, looks different. For example, the energy is still concentrated in the initial vertical mode after 4 hours of free evolution. It looks like the wave has not reached the mean flow by this time, which can be explained by the lower vertical group velocity of waves with higher vertical wave numbers (refer to (5.4)). However, after 8 hours there is hardly any energy left in the $ik = 3$ horizontal mode, which we ascribe to the effect of critical layer interaction.

Energy transfer among horizontal modes is initially to the second harmonics, $2ik_1$ and $2ik_2$, and in particular to the sum of the initial wave numbers, $ik_1 + ik_2$. Subsequently, energy is spread out between the lowest six horizontal modes, with higher levels in mode 4 and 5.

One critical and one turning wave The wave packet with a critical wave, $[ik_1, im_1] = [2, 16]$, and a turning wave, $[ik_2, im_2] = [-3, 24]$, is shown in Fig. 5.10. In the top four panels we observe that wave energy initially propagates downward in the first half of

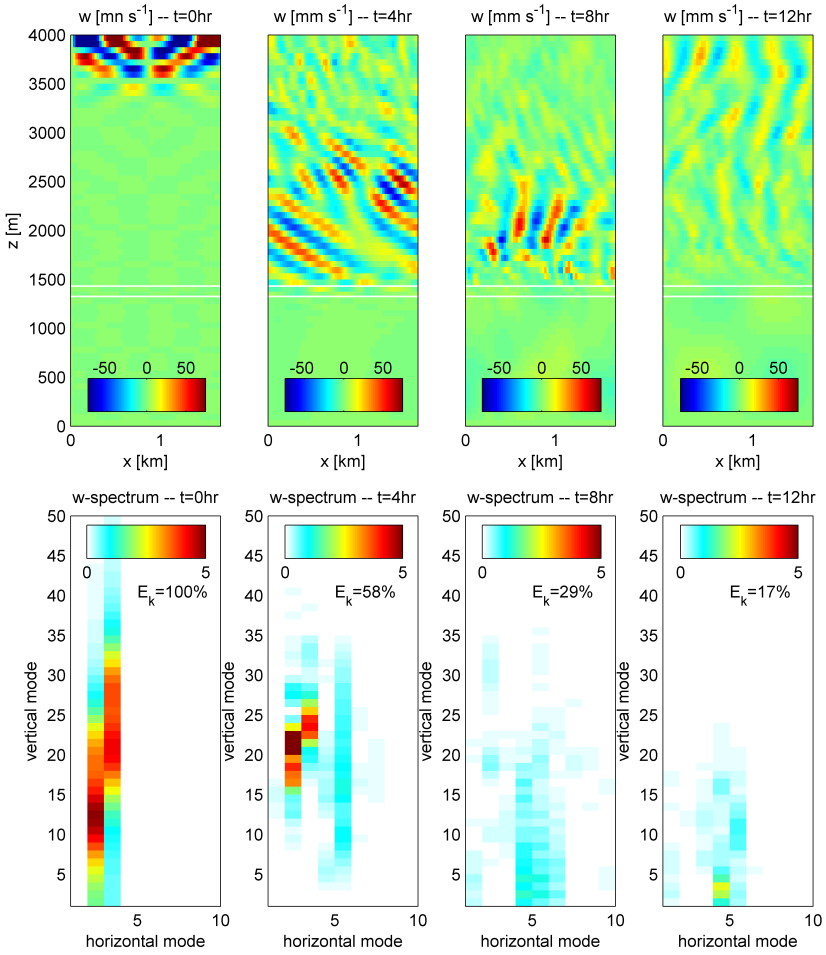

Figure 5.9: Time evolution of wave packet with two critical waves, $[ik_1, im_1] = [2, 16]$ and $[ik_2, im_2] = [3, 24]$. Top row: four snapshots of the vertical velocity with a variable colour scale in mms^{-1}. Bottom row: vertical velocity spectrum. The white lines indicate the critical level for each of the waves (lower level corresponds to wave 1). All waves have equal displacement amplitudes, $\xi = 40$ m, and the mean flow parameters are, $U_0 = 0.7$ ms^{-1}, and $d = 600$ m.

the simulation and upward in the second half. This is consistent with the expected reflection of the turning wave at the turning point. The reflection of wave energy is also reflected in the slower decline rate of total kinetic energy compared to the simulation with two critical waves. More than 60% of the initial kinetic energy is still in the system at the end of the simulation.

The spectral energy distribution also develops differently. Energy quickly concentrates around vertical mode 22 for both waves. This agrees with the previous experiment where we also found that the energy in the wave with initial modes $[2, 16]$ transfers to $[2, \sim 22]$ after 4h. The turning wave is initialized with a higher vertical mode number, $im = 24$, and has not reached the mean flow after 4h. After 8h we find that the critical wave ($ik = 2$) has dissipated almost completely and that some of the energy in the turning wave ($ik = -3$) has been transferred to slightly lower vertical modes, as expected based on (5.5). More remarkably, we also observe a significant transfer of energy to waves with low vertical modes and horizontal mode number $ik = 4$.

Nonlinear effects Figure 5.11 compares dissipation rate for two separately evolving waves and two waves evolving together. One of the waves is critical and the other is a turning wave. The dissipation rate is averaged along the horizontal spatial dimension and plotted against the vertical coordinate and time. The vertical dissipation profile for two initial waves $\langle \epsilon(\mathbf{k}_1 + \mathbf{k}_2) \rangle (z)$ has a larger peak in the mean shear zone compared to the summed dissipation rates of the two single wave simulations $\langle \epsilon(\mathbf{k}_1) + \epsilon(\mathbf{k}_2) \rangle (z)$. In the mean shear zone we observe that dissipation rates are more than 1.5 times larger for the two waves case compared the lin-

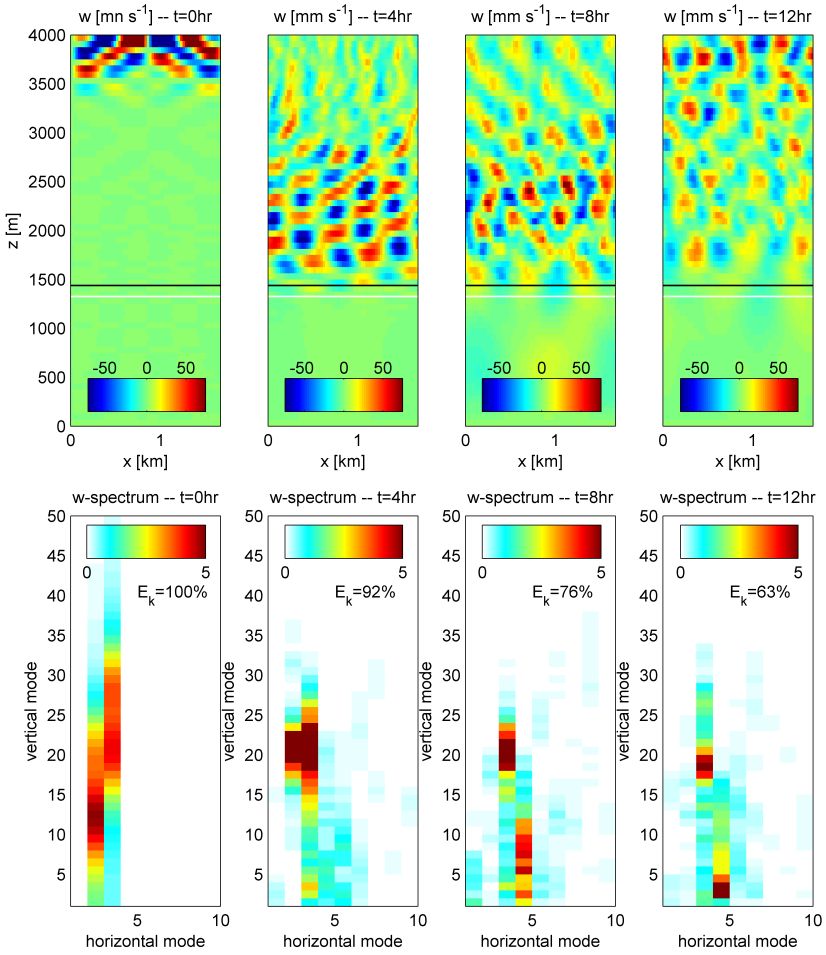

Figure 5.10: Time evolution of wave packet with one critical and one turning wave, $[ik_1, im_1] = [2, 16]$ and $[ik_2, im_2] = [-3, 24]$. Top row: four snapshots of the vertical velocity with a variable colour scale in mms^{-1}. Bottom row: vertical velocity spectrum. The white line indicates the critical level for each of the waves and the black line indicates the turning level. All waves have equal displacement amplitudes, $\xi = 40$ m, and the mean flow parameters are, $U_0 = 0.7$ ms^{-1}, and $d = 600$ m.

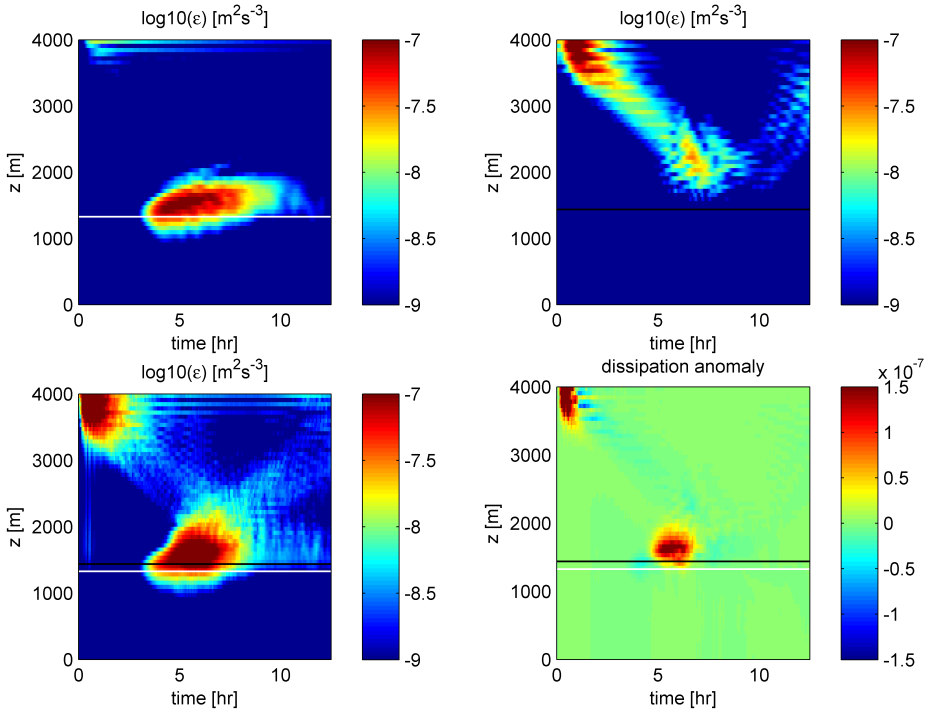

Figure 5.11: Horizontally averaged dissipation profile versus time for two waves: one critical and one turning. Top left: critical wave. Top right: turning wave. Bottom left: critical and turning wave together. Bottom right: dissipation anomaly, i.e. the difference between two waves together and the sum of single waves, $\delta\epsilon = \epsilon(k_1 + k_2) - (\epsilon(k_1) + \epsilon(k_2))$ (refer to Table 5.1 for the used wave numbers). The white line indicates the critical level and the black line the turning point.

ear superposition of the single wave experiments.

Figure 5.12 is comparable to Fig. 5.11, but shows dissipation rate for two critical waves. This figure shows that the dissipation anomaly in the mean shear zone is less pronounced and of opposite sign, compared to the previous case with one critical and one turning wave. This suggests that the net effect of nonlinear interactions among two critical waves is to transfer energy into other, non-critical waves. This means that the waves have lost some energy when they reach the critical layer and dissipate. The individually propagating waves have no other waves to interact with, and

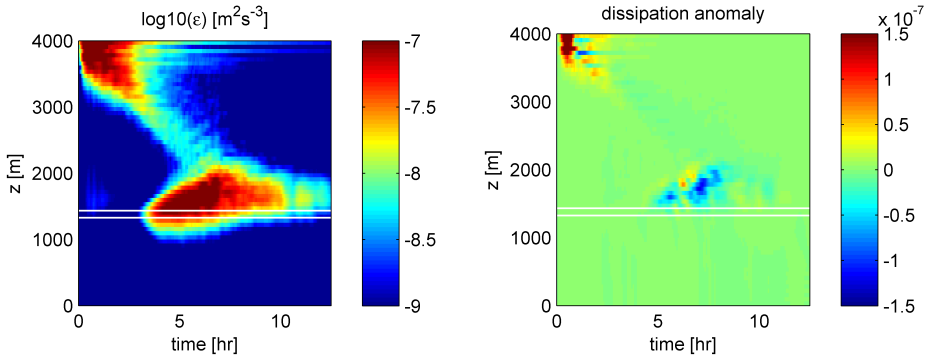

Figure 5.12: Horizontally averaged dissipation profile versus time for two critical waves. Bottom left: two critical waves. Bottom right: dissipation anomaly, $\delta\epsilon = \epsilon(k_1 + k_2) - (\epsilon(k_1) + \epsilon(k_2))$, refer to Table 5.1 for the used wave numbers. The white lines indicate the critical levels.

therefore we expect them to dissipate close to all their initial energy when they reach the critical level.

This experiment demonstrates a significantly larger energy transfer rate to smaller scales by internal wave – mean flow interactions when we allow for wave–wave interactions. The nonlinear coupling between waves is directly evaluated in our model, based on (5.8)–(5.12), without any further assumptions. We will use this advantage of direct numerical simulation to investigate the dynamics of a broad band internal wave field in a mean shear flow.

5.6.4 The broadband wave field

The two-dimensional initial wave field is a superposition of left– and right propagating waves in the $x - z$-plane. Initially, energy and phase propagate horizontally, because of the rigid boundaries at the top and bottom of the domain (refer to Section 5.4.2). The energy in each wave is derived from the GM76 spectrum (refer to Section 5.4.3) and distributed normally among right and left propagating waves (with $\mu = 0.5$ and $\sigma = 0.2$ and at least 1% of the total energy going

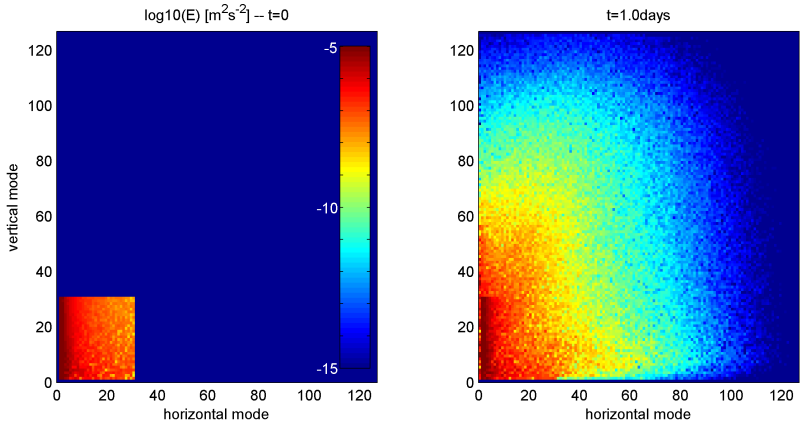

Figure 5.13: Modal spectrum. Left: initial state. Right: spectrum after 1 day evolution.

in either direction). The initial wavefield contains all combinations of the 30 lowest modes (except zero) in both spatial directions, including negative horizontal modes.

Figure 5.13 shows the modal spectrum of the initial wavefield. The spectrum has the general GM energy distribution, with most energy in the lowest horizontal modes, but is not as smooth. We interpret the speckles in the spectra as a result of the interference of left- and right propagating modes. The offset from the GM spectrum differs for each wave number, because all waves have a different energy and different phase. The right panel of Fig. 5.13 shows that energy quickly spreads to higher wave numbers up to the point where the energy is dissipated by hyperviscosity (refer to Section 5.5.2).

The left panel of Figure 5.14 shows the filling of frequency space. The large horizontal extent of the domain accommodates near-inertial waves with frequencies close to f. Pure gravity waves exist in the limit $k \to \infty$ and are limited by the horizontal Nyquist wave number. Each frequency represents an unique aspect ratio $\frac{k}{m}$, which explains the existence of multiple pairs

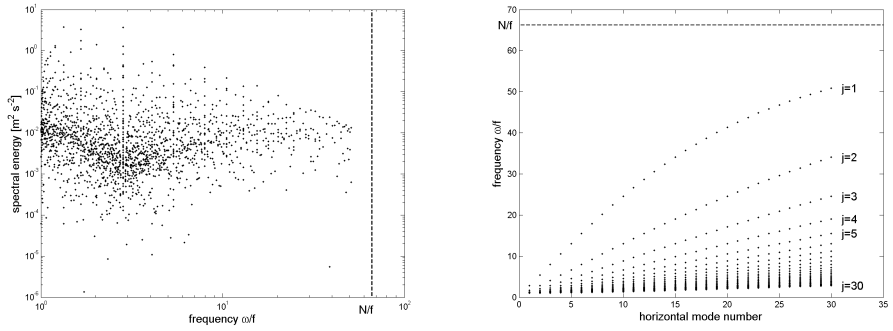

Figure 5.14: Broadband initial state with all combinations of the 30 lowest horizontal and vertical modes. Left: frequency spectrum. Right: frequencies per horizontal mode.

of modes (k, m) per frequency.

Figure 5.15 compares the velocity and shear spectrum with the GM model. Integrating the GM model (5.22) over all frequencies between f and N and using the polarization relations to write $V^2 = u^2 + v^2$ in terms of the vertical mode number j gives velocity spectrum $S[V](j) = 3E_0 b^3 N_0^2 (2j^*\pi)^{-1}(1+j/j^*)^{-2}$. The buoyancy frequency normalized shear can be derived from the velocity spectrum by vertical differentiation, $S[V_z/N^2](j) = N^{-2}m^2 S[V](j)$, with $m = j\pi L_z^{-1}$.

5.6.5 Dissipation versus mean flow shear

In a series of numerical experiments we explore the relation between internal wave dissipation and the shear of the mean flow. All the experiments are initialized with the same internal wave field with an energy density of $0.89E_{GM}$. The mean flow has the same amplitude, $U_0 = 0.5$ m/s, but a different shear length scale, $d \in [200, 400, 600, 800, 1000]$ m (refer to Section 5.4.4).

Figure 5.16 shows the temporal evolution of the dissipation rate for the simulation with lowest shear ($d = 1000$m) and Fig. 5.17 shows the result of the

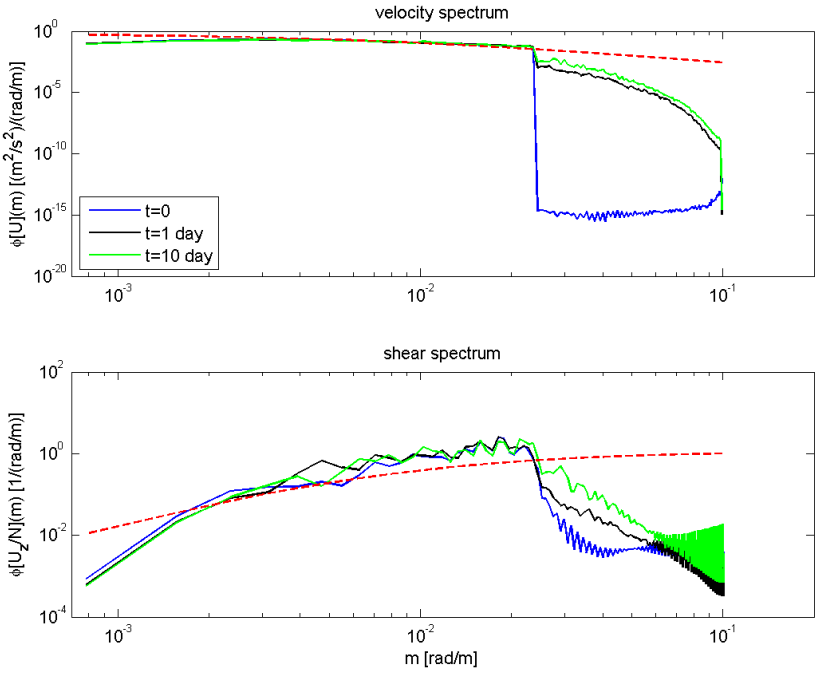

Figure 5.15: Velocity and shear spectrum as calculated from the initial velocity field and after 1 and 10 days of free evolution (no mean flow). The dashed red line indicates the GM76 spectral level.

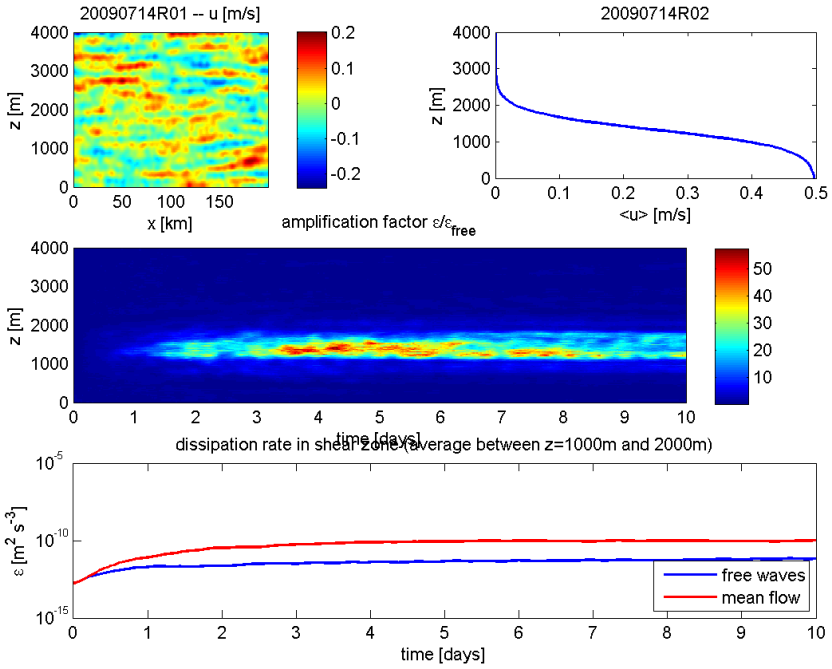

Figure 5.16: Weakly sheared mean flow with $d = 1000$m and a GM-like wavefield. Top left: initial wave field. Top right: mean flow. Middle: horizontally averaged dissipation rate of waves plus mean flow normalized by dissipation rate of waves only. Bottom: dissipation rate averaged in horizontal direction and between $z = 1000$m and $z = 2000$m for waves only and waves plus mean flow (labeled as 'mean flow').

simulation with highest shear ($d = 200$m). The middle panel displays the dissipation rate normalized by the dissipation of free waves without a mean flow, and hence shows how much the dissipation is amplified by mean flow interaction. The maximum amplification of the background dissipation rate due to wave–mean flow interaction is up to 55 times in the low shear case and more than factor 400 in the high shear case.

Interestingly, the bottom panel of Fig. 5.16 and 5.17 shows that the dissipation rate in the shear zone (defined as the vertical range $1000 < z \leq 2000$m) is more or less the same for both shears after an initial ramp up time. Figure 5.18 shows that this is also the

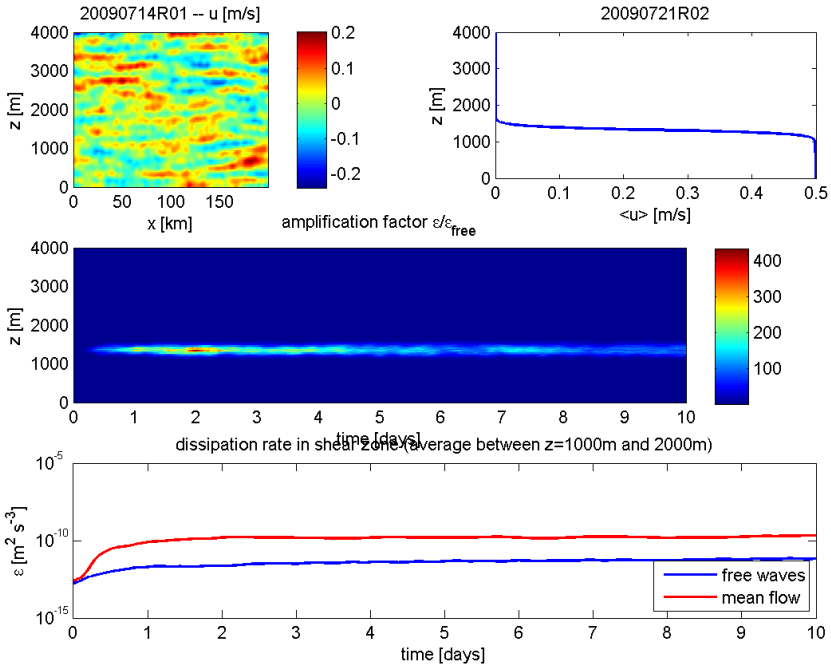

Figure 5.17: Strongly sheared mean flow $d = 200$m and a GM-like wavefield. Top left: initial wave field. Top right: mean flow. Middle: horizontally averaged dissipation rate of waves plus mean flow normalized by dissipation rate of waves only. Bottom: dissipation rate averaged in horizontal direction and between $z = 1000$m and $z = 2000$m for waves only and waves plus mean flow (labeled as 'mean flow').

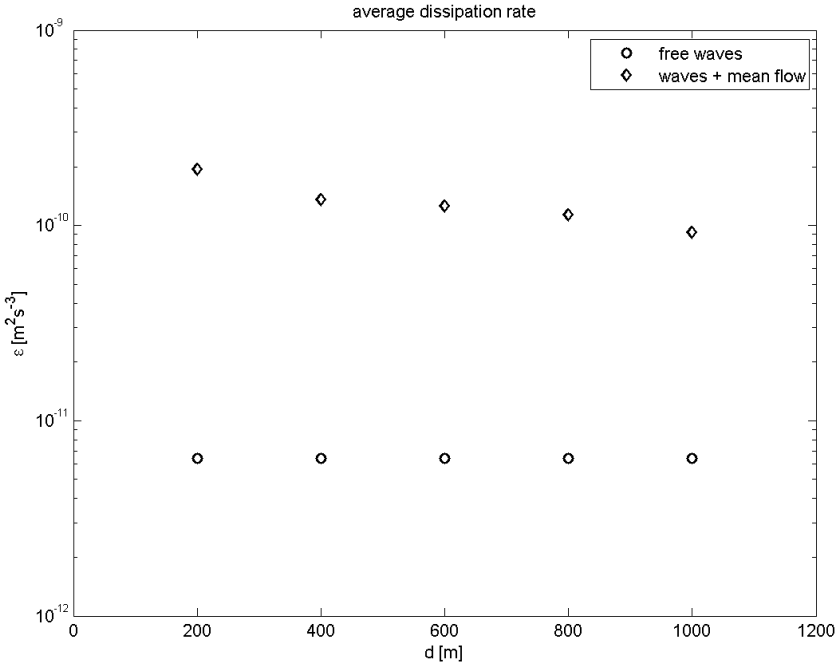

Figure 5.18: Dissipation versus mean flow shear, U_0/d, with $U_0 = 0.5$ ms^{-1}. The dissipation rate is spatially averaged along the horizontal dimension and between $z = 1000$ and $z = 2000$m in the vertical and temporally between day 9 and 10.

case for other values of the shear parameter d. This suggests that the energy transfer rate to smaller scales is not sensitive to the exact location of the critical layers nor to the spacing between these layers.

The ramp up time however is different for different shears. The low shear case gives a long ramp up time of almost two days and the high shear case ramps up quickly in less than half a day.

The dissipation in the shear zone reaches a rate of about 10^{-10} m^{2}s^{-3} after the ramp up and stays almost exactly at this level for the duration of the experiment. This suggests that nonlinear wave–wave and wave–mean flow interactions supply 'critical waves' (here defined as waves for which a critical layer exists) at

a more or less constant rate during the 10 day evolution.

Critical waves however are not merely supplied by nonlinear interactions. Figure 5.22 shows that a fraction of the *initial waves* is critical and thus directly available for critical layer interaction.

We have constructed a simple model to predict the dissipation rate in the shear zone due to initial critical waves only. We define a single critical layer at $z = L_z/3$ and assume that all waves with a horizontal phase speed smaller than U_0 will eventually dissipate when encountering this level. We assume a GM-like wave field and estimate the amount of energy reaching this level using the vertical group velocity,

$$Cg_z \equiv \partial\omega/\partial m = \frac{m}{(f^2m^2 + N^2k^2)^{\frac{1}{2}}} \left[\frac{f^2}{(k^2+m^2)^{\frac{1}{2}}} - \frac{(f^2m^2 + N^2k^2)}{(k^2+m^2)^{\frac{3}{2}}} \right]. \tag{5.34}$$

At time interval $[t, t + \Delta t]$ we expect waves from distance range $Cg_z \times [t, t + \Delta t]$ to arrive at the critical layer. The permissible distance range is limited by the dimensions of the computational domain and multiplied by factor 2 when smaller than $L_z/3$ to account for waves travelling towards the critical layer from above and below.

Assuming uniform spatial distribution of the initial waves we estimate the energy of wave (k, m) arriving at the critical layer at time t as,

$$E(t, k, m) = \frac{Cg_z(k, m)\Delta t}{L_z} E_{GM}(k, m). \tag{5.35}$$

The energy arriving at the layer is dissipated when the vertical wave number gets close to the Nyquist wave number, $m_{nyq} = n_z\pi/L_z$, because the numerical viscosity damps these motions out (refer to Section 5.3.2).

The rate of change of the vertical wave number

in the presence of a mean flow is proportional to the shear, $dm/dt = -kU_z$, according to WKB ray-tracing theory [Kunze, 2000]. For our mean flow profile we approximate $dm/dt = kU_0/d$, where the minus sign has dropped out because $k > 0$ and $U_0 > 0$ and k and U_0 have equal signs for a critical layer (refer to Section 5.2) and $U_z < 0$ for z positive upward. The additional time for a wave (k, m) to reach the dissipation scale is,

$$t' = \frac{m_{nyq} - m}{dm/dt}. \tag{5.36}$$

Adding $t + t'$ gives the time when $E(t, k, m)$ is dissipated and we define the dissipation rate as $E(t, k, m)/(t+t')$. Binning the dissipation rates for all waves in time bins gives the dissipation time series in Fig. 5.19.

From Fig. 5.19 we learn that different ramp up times can be explained by the dependence of the transfer rate to small scales on the magnitude of the shear. We also observe that the dissipation rate decreases after reaching its maximum value, in contrast to the numerical calculations (refer to Fig. 5.16, Fig. 5.17 or Fig. 5.19). The results from our simple model seems to indicate that the energy in the critical waves present at $t = 0$ is quickly depleted and insufficient to explain the magnitude and steadiness of the dissipation rate in the numerical experiments. We therefore conclude that the bulk of the energy at critical wavelengths is supplied through nonlinear interactions.

5.6.6 Dissipation versus mean flow strength

We explore the dependence of the internal wave dissipation on the strength of the mean flow by varying the mean flow amplitude U_0 and keeping the shear constant at a value of $U_0/d = 0.001$ s^{-1}. Figure 5.20 shows the temporal evolution of the mean dissipation in the range 1000m$< z <$ 2000m for three values for

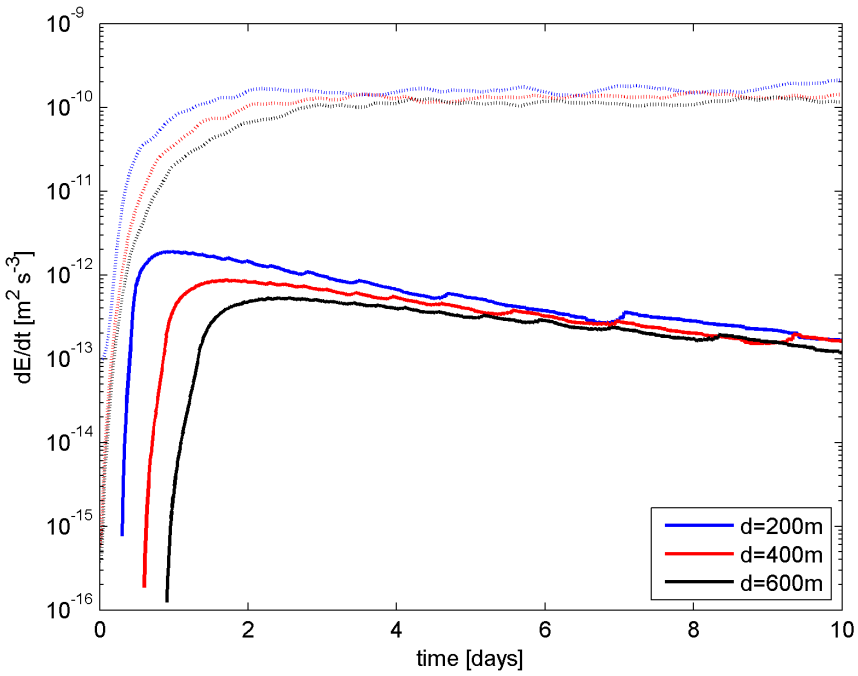

Figure 5.19: Dissipation rate based on a simple model (solid lines) compared to full simulations (dotted lines). The model treats all wave modes as non-interacting except at the critical layer where they transform to smaller scales at a rate, $dm/dt = kU_0/d$, until they dissipate close to the given Nyquist wave number.

U_0: 0.05, 0.25 and 0.5 ms^{-1}. Note that the evolution of the dissipation rate looks remarkably similar for $U_0 = 0.25$ ms^{-1} and $U_0 = 0.5$ ms^{-1}.

Figure 5.21 shows the average dissipation rate in the shear zone. The spatial averaging range is between $z = 1000$ m and $z = 2000$ m vertically and the horizontal domain size. We allow some time for interactions between the internal waves and the mean flow to develop by choosing the temporal averaging window between day 9 and 10. For $U_0 > 0.2$ ms^{-1} we see that the dissipation rate is more or less constant, whereas $U_0 < 0.2$ ms^{-1} shows a collapse towards free wave dissipation rates.

A weak mean flow provides a critical level for waves with high wave numbers, as is shown in Fig. 5.22. These small scale, high wave number waves contain relatively little energy because energy in the initial GM wave field is concentrated in the lower modes. Moreover, the bit of energy that is available at high wave numbers is also viscously damped, as hyperdissipation becomes more important at high wave numbers. We explain the collapse of the dissipation rate at low mean flow strength by the combination of these two effects.

The dissipation plateau for large amplitude mean flows, with $U_0 > 0.2$ ms^{-1}, seems to imply that the replenishment rate of dissipated waves is more or less constant when sufficiently many, lower wave number waves are critical. Whether this presumption can be backed by internal wave theory is subject of ongoing research.

5.6.7 Sensitivity to the number of initial modes

The majority of the energy in the Garrett-Munk field resides in the lowest modes. For example, only the lowest three vertical modes account for 52% of the total

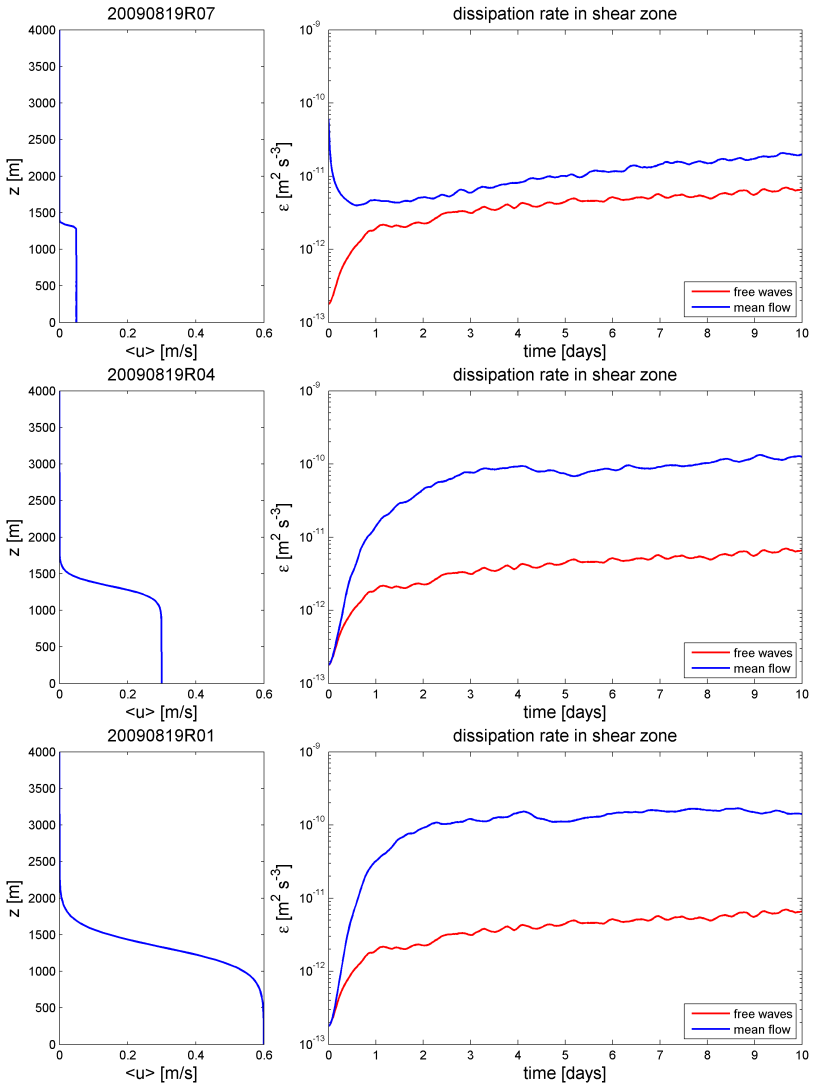

Figure 5.20: Dissipation versus mean flow strength. Top: $U_0 = 0.05$ ms^{-1}. Middle: $U_0 = 0.25$ ms^{-1}. Bottom: $U_0 = 0.5$ ms^{-1}. The shear is the same and has a value of 0.001 s^{-1}.

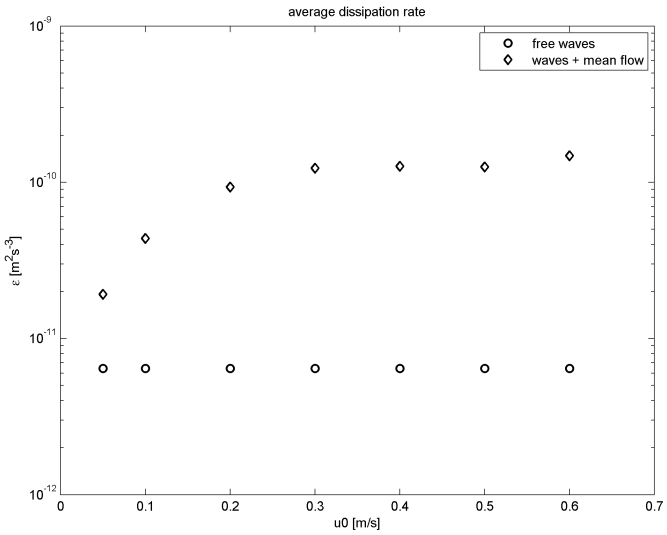

Figure 5.21: Dissipation versus mean flow strength with constant vertical shear, $U_0/d = 0.001$ s^{-1}. The dissipation rate is averaged along the horizontal direction and vertically between $z = 1000$ m and $z = 2000$ m and temporally between day 9 and 10.

energy[3]. Although the bulk of the energy is contained in the lowest modes we chose to initialize our model with an additional number of higher modes. This puts very little extra energy into the system but does provide more resonant wave triads for nonlinear interaction and energy transfer towards dissipative scales.

Many experiments discussed in this chapter are initialized with all combinations of the lowest 30 vertical and horizontal modes. Figure 5.23 compares the time evolution of the dissipation rate for simulations with 20^2, 30^2, and 40^2 initial modes. The figure shows that quadrupling the number of modes, from 20^2 to 40^2, increases the dissipation rate by 700%, although the total initial energy increases only 6%. This supports the notion that the inclusion of higher modes facilitates the transfer of energy to small scales.

[3]The total energy is defined as the energy in the lowest 250 modes.

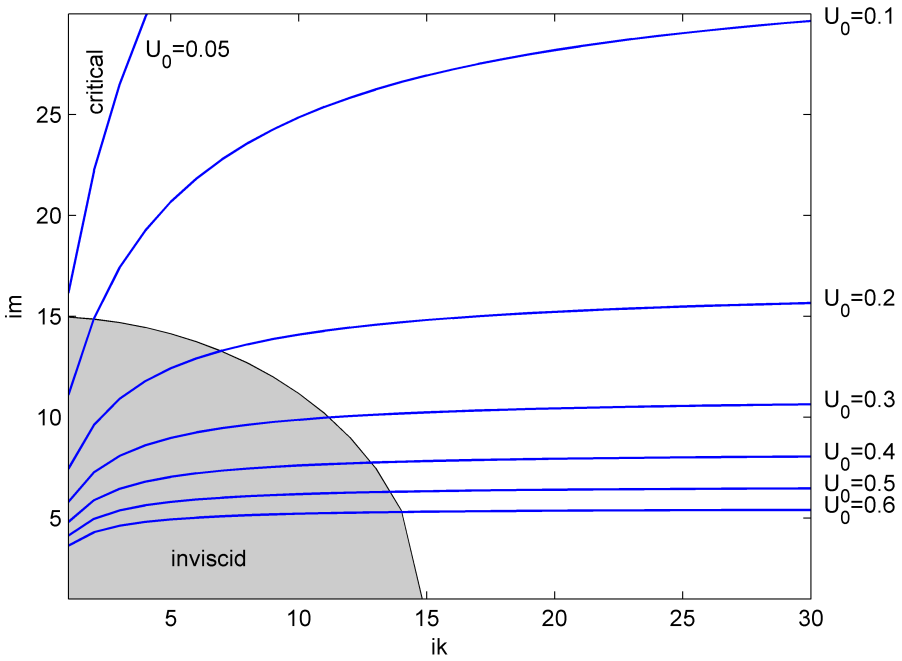

Figure 5.22: Lowest critical wave numbers for a given mean flow amplitude. The grey shaded area indicates the wave numbers for which the numerical viscosity is smaller than the molecular viscosity of water.

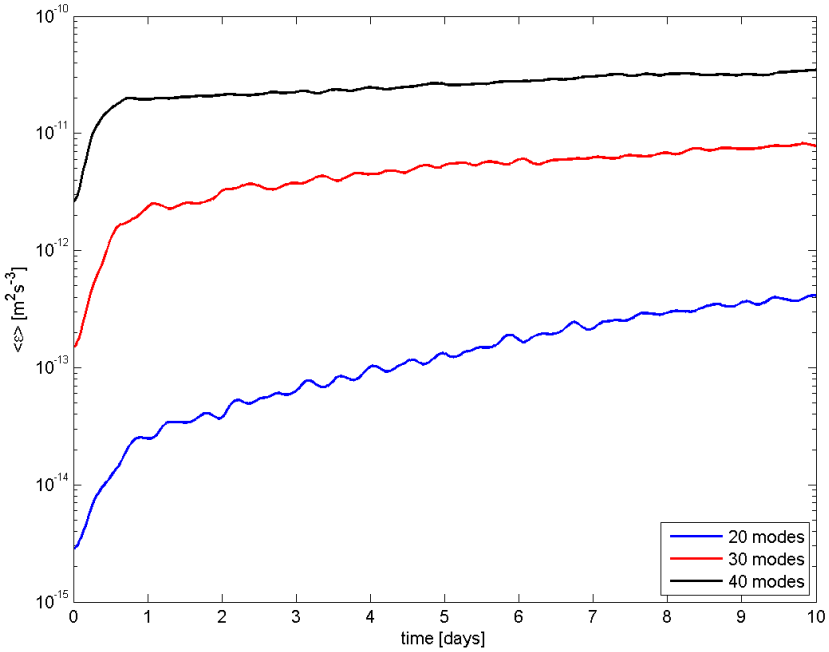

Figure 5.23: Time evolution of the spatially averaged dissipation rate for a different number of initial modes. There is no mean flow in this simulation.

Whether 30^2 initial modes is sufficient appears disputable. Figure 5.3 shows that the dissipation rate reaches its maximum after about 60 days when initialized with 30^2 modes. The maximum rate is about 2×10^{-10} m^{2}s^{-3}, which is about 30% of the GM steady state dissipation rate. The dissipation rate after 10 days is only 12% of the GM value.

The simulation with 40^2 initial modes reaches a dissipation level of 1×10^{-10} m^{2}s^{-3} after only one day and increases only slightly over the next 9 days, which could be regarded as a more adequate representation of the dissipation of a steady and thus forced GM wave field.

5.6.8 Sensitivity to the choice of viscosity parameters

In this section we assess the effect of the choice of hyperviscosity parameters on the dissipation rate. Figure 5.24 shows the time evolution of the spatially averaged dissipation rate for different hyperviscosity coefficients. The simulation is initialized with a GM-like broad band wave field with 30 horizontal and 30 vertical modes and a weakly sheared mean flow with $d =$ 1000m (refer to Section 5.4.4). The figure shows three simulations with hyperviscosity coefficients, $[p, T_{diss}] = [8, 10000], [10, 1000]$ and $[12, 100]$.

The simulations show that the dissipation rate is higher for lower order hyperviscosities, that is smaller p values. The dissipation time scale, T_{diss}, is chosen such that the hyperviscosity crosses the Newtonian viscosity at approximately the same wave number (refer Fig. 5.2). The viscous wave damping becomes significant beyond this wave number, and this happens especially 'quickly' for higher p values. Thus, the p value effectively determines how many higher wave number are permitted in the system.

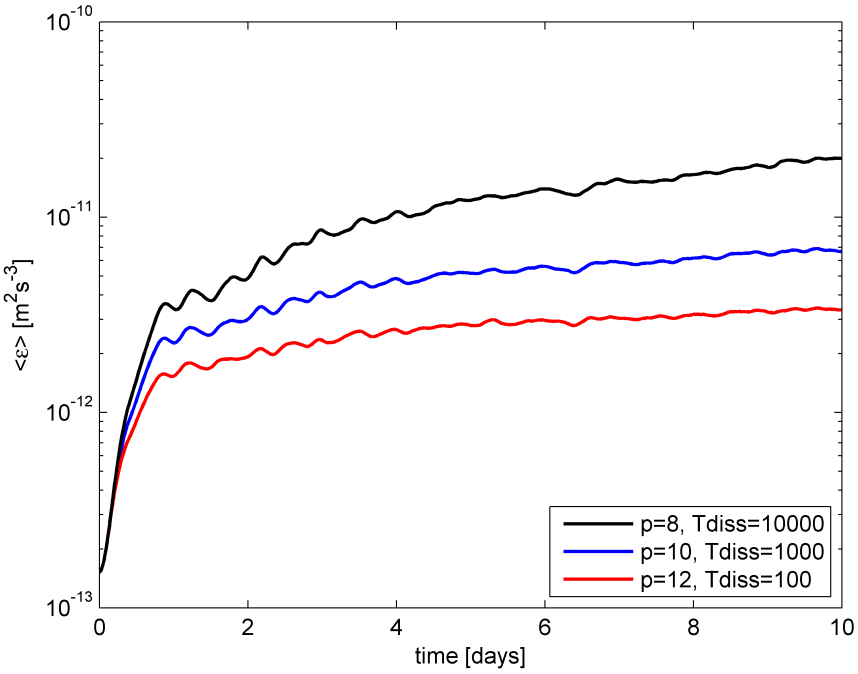

Figure 5.24: Spatially averaged dissipation rate for different hyperviscosity coefficients. Coefficients are chosen such that the wave number at which hyperviscosity surpasses Newtonian viscosity remains more or less the same. The coefficients used for the broadband simulations are $p = 10$ and $T_{diss} = 1000$.

This means that many of the high wave numbers that partake in nonlinear interactions in the simulation with $p = 8$ are non-existent in the simulation with $p = 12$, because they have been damped out by the hyperviscosity. Apparently, there is a higher net flux of energy towards dissipative wave numbers if waves with higher wave numbers are available for interaction with the rest of the wave field.

5.7 Discussion

In this chapter we looked at the dissipation of a broad band, Garret-Munk-like wave field in the presence of a sheared mean flow. This problem was brought to our attention by the observation of a strong jet flow in the Atlantic II Fracture Zone, in the Southwest Indian Ridge [MacKinnon et al., 2008]. The discovery of the jet led us to hypothesize that internal wave mean flow interaction might be an alternative or complementing mechanism to explain the generally observed high dissipation rates in submarine canyons. Canyon mixing has so far been associated mostly with 'hydraulic jumps', downstream of sills [Thurnherr et al., 2005; Thurnherr, 2006; Thorpe, 2007].

Many important features of the upper atmosphere are explained by internal wave mean flow interaction [Lindzen, 1973] and this likely holds true for the deep ocean as well. For example, [Muench and Kunze, 1999, 2000] show that the momentum flux divergence due to internal wave critical layer interactions suffices to maintain the equatorial deep jets. Internal waves are also likely to cause momentum transfer and instabilities in the vicinity of other persistent ocean currents, such as the Antarctic Circumpolar Current, the Gulfstream and other western boundary currents, such as the Agulhas– and the Kuroshio Current. The interac-

tion between internal waves and deep flows is potentially relevant to the deep MOC.

Interactions between the internal wave field and a mean flow may be relevant to the Indian Ocean MOC because it could cause mixing at places where it is most needed. For example, the bulk of the inflow of deep and bottom water into the Indian Ocean across 32°S may be concentrated in jet-like flows through the SWIR [MacKinnon et al., 2008] and deep western boundary currents [Beal and Bryden, 1997]. Strong mixing at the interface between these flows and the lighter overlaying water masses appears advantageously localized to transform the deep limb of the Indian Ocean MOC. However, whether this leads to significant mixing of deep water masses is not obvious, because of the limited contact area between the deep water masses and the critical layers and also because of the short transient times of deep water masses in strong flows.

Our numerical results show an interesting relation between wave dissipation and the strength of the mean flow. As expected, we find higher dissipation rates when we introduce a mean flow in the system. More surprisingly, we also find that the dissipation rate reaches a plateau value for mean flow amplitudes larger than 0.2 ms^{-1}. At this point it is unclear whether this threshold value is related to a fundamental property of the internal wave field, such as the spectral replenishment rate, or a numerical artefact. This issue is subject of ongoing research.

Motions in the oceanic internal wave field span length scales from the size of the basin to centimetres, which makes it impossible to capture the full range in a numerical model. We focus on 'mid-range' scales, which means that largest, near-inertial motions, and the smaller, sub-grid size, motions are not represented

in the model. Therefore we rely on the assumption that there is a negligible upscale energy transfer at scales close to the numerical grid size or smaller.

In fact, we use a relatively coarse grid compared to the displacement amplitude of the internal waves, similar to the numerical setup used by [Winters and D'Asaro, 1997]. This means that the dynamics of wave-breaking are not resolved in our model, but that does not mean that the dissipation rates calculated by the model are unrealistic. Using essentially the same model in a 3D setup, [Winters and D'Asaro, 1997] find that a simulation initialized with a GM-like internal wave field produces a GM-like dissipation rate. Based on their result we believe that the results from our idealized model are in principle comparable to the real ocean when appropriately initialized.

Details of wave-instability near a critical level have been studied using similar numerical methods for a single wave packet in 2D [Winters and D'Asaro, 1989] and in 3D [Winters and D'Asaro, 1994]. These studies focus on the development of shear– and convective instabilities and find that convective instabilities need the third dimension and some random noise to develop vortical motions. It is shown that vortical motions are important in the onset to turbulence, but we do not expect that the two-dimensionality of our simulations affects the dynamics of the scales resolved in our model.

Plans for future research include: (i) more detailed analysis of the spectral transfer of energy in the experiments with a few waves only; (ii) further exploration of how the dissipation rate depends on the initial wave field; (iii) exploration of the relation between dissipation and the energy of the internal wave field, both in 2D and 3D; (iv) and, as mentioned above, a further investigation of the relation between dissipation and

mean flow strength.

5.8 Summary and conclusion

In this chapter we used a spectral numerical model to study the interaction between internal waves and a sheared mean flow. We did a number of numerical experiments with increasing complexity, from one wave and one critical layer to many waves with Garrett-Munk wave amplitudes and various mean flow settings. All simulations are unforced and initialized with a two-dimensional flow field. The model equations however are three-dimensional and fully nonlinear.

In all simulations we observed increased wave dissipation in the presence of a mean flow, as compared to a control run with internal waves only. This is consistent with theory. More interestingly, we find that the dissipation of kinetic energy in the system hardly depends on the shear of the mean flow. The local intensity of the dissipation however does depend on shear and is higher for stronger shear. This is likely to be relevant in the real ocean where wave dissipation is associated with wave breaking and turbulent mixing.

We also found that the strength of the mean flow only matters below a threshold value of 0.2 ms^{-1}. Larger mean flow amplitudes do not affect the mean dissipation level as long as the mean flow itself remains stable. The question whether this result is fundamental to internal waves or a numerical artefact is subject of ongoing research.

Chapter 6

Conclusion

The main result of this dissertation is that turbulent kinetic energy (TKE) production by internal waves is not enough to sustain the deep meridional overturning circulation (MOC) in the subtropical Indian Ocean. This result challenges the view expressed by [Wunsch and Ferrari, 2004] that "Much, if not all, of the mixing energy is bound up in the internal wave field,[...]" (p.28). It looks like internal wave breaking has been over-emphasized as a source of TKE in the deep ocean, which implies that other viable processes, such as drag on the general circulation in passageways, deserve more attention.

The overturning circulation is a bulk carrier of kinetic energy to the deep ocean, but it is unclear how much of this energy is converted to TKE. Hydraulic jumps at sill overflows in narrow passageways provide a mechanism to draw energy from the general circulation and produce turbulence. This energy pathway to TKE production has been explored in the Mid Atlantic Ridge [Thurnherr et al., 2005; St Laurent and Thurnherr, 2007] and may explain the observed elevated mixing rates in Indian Ocean fracture zones and passages [Barton and Hill, 1989; Johnson et al., 1998; McCarthy et al., 1997].

The deep northward limb of the Indian Ocean overturning may be sustained by mixing in the numerous fracture zones, but this seems less likely for the shallower, southward return flow. For example, the 27.18 kg m^{-3} density surface, which is the typical closing density for most overturning solutions, intersects only with the Owen Fracture Zone and the Mascarene Plateau. However, the [McDonagh et al., 2008] solution is based on newer observations and gives a significantly deeper overturning cell that closes at about 27.75 kg m^{-3}. A quick analysis shows that this density surface intersects with almost all major topographic formations in the Indian Ocean. In future research we wish to address the question whether mixing in passages and canyons can close any of the overturning energy budgets considered in this study.

Another source of TKE explored in this dissertation is the dissipation of a broad band internal wave field due to critical layer interactions in a sheared mean flow. Enhanced internal wave dissipation due to mean flow interaction may not be captured adequately by the fine scale shear/strain parameterization of turbulent dissipation. Elevated spectral levels of shear and strain have been observed in the vicinity of mean flows, for example close to equatorial jets in the Indian Ocean by [Dengler and Quadfasel, 2002], but the accuracy of the inferred dissipation rates in unknown in this regime. It would be interesting to assess the performance of the fine scale parameterization in a sheared mean flow.

Appendices

Appendix A

Density resolution advection–diffusion model

This derivation shows that the choice of density levels in the advection–diffusion model does not matter for the turbulent mass transport at a given density level.

F at z_1, one layer Let's start with the single density layer in Fig. A.1a, with a hard bottom at $z = 0$, a density interface at $z = z_1$ with density ρ_1 and advective mass transport $\int_0^{z_1} \rho T \, dz$ through the left hand side, where $T = \int u(y, z) \, dy$ is the transport per unit

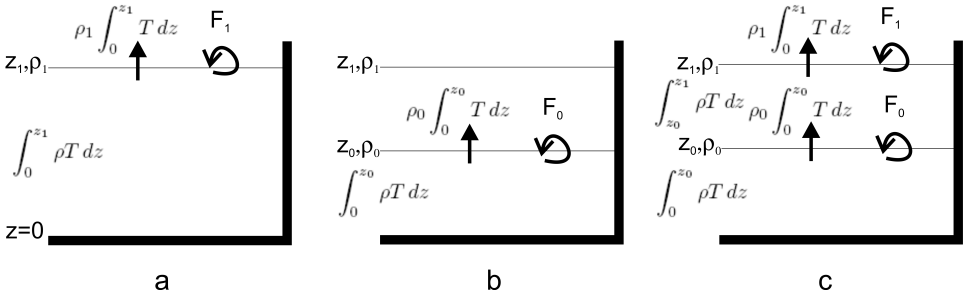

Figure A.1: Vertical cross-section of a box-volume with hard walls on three sides and a hard bottom. Advective transport is allowed through the open left-hand-side. Note that T is transport per unit depth.

depth [$m^2 s^{-1}$]. Assuming a balance between advection and diffusion we can solve for the turbulent mass transport at z_1,

$$F_1 = \int_0^{z_1} \rho T \, dz - \rho_1 \int_0^{z_1} T \, dz. \tag{A.1}$$

F at z_0, one layer Suppose we introduce a new layer at $z = z_0$, with $0 < z_0 < z_1$, see Fig. A.1b. The turbulent mass transport at z_0 is,

$$F_0 = \int_0^{z_0} \rho T \, dz - \rho_0 \int_0^{z_0} T \, dz. \tag{A.2}$$

F at z_1, two layers Let's now calculate the turbulent mass transport at z_1 based on the mass transport into the layer between z_0 and z_1. Collecting all the mass flux terms in Fig. A.1c we get,

$$F_1 = F_0 + \int_{z_0}^{z_1} \rho T \, dz + \rho_0 \int_0^{z_0} T \, dz - \rho_1 \int_0^{z_1} T \, dz. \tag{A.3}$$

Substitution of (A.2) in (A.3) gives,

$$\begin{aligned} F_1 = &\int_0^{z_0} \rho T \, dz - \rho_0 \cancel{\int_0^{z_0} T \, dz} + \\ &\int_{z_0}^{z_1} \rho T \, dz + \rho_0 \cancel{\int_0^{z_0} T \, dz} - \rho_1 \int_0^{z_1} T \, dz = \\ &\int_0^{z_1} \rho T \, dz - \rho_1 \int_0^{z_1} T \, dz, \end{aligned} \tag{A.4}$$

and we get the same expression as in the one layer case, refer to (A.1).

Appendix B

Bottom roughness

We define bottom-roughness as the square root of the mean square distance between a smooth polynomial surface $\tilde{z}(x, y)$ and the Smith and Sandwell bathymetry z_{SS} Smith and Sandwell [1997],

$$r(x, y) = \sqrt{\overline{(z_{SS} - \tilde{z})^2}}, \tag{B.1}$$

where the overline denotes spatial averaging.

The 2D polynomial $\tilde{z}(x, y) = c_1 x + c_2 x^2 + c_3 xy + c_4 y + c_5 y^2 + c_6$ (same as in Morris et al. [2001]) is fitted to one thirtieth degree bathymetry data in 0.5×0.5 degree, non-overlapping patches. For each patch A we find the polynomial coefficients by solving, $Mc = z_{SS}$, where the matrix M contains the polynomial terms evaluated at the points $(x, y) \in A$, and $c = (c_1, c_2, \ldots, c_6)$ is a vector with the unknown polynomial coefficients. In our particular case we deal with an overdetermined set of equations (240 equations, 6 unknowns). We can find a least-squares solution to this problem by solving the normal equations,

$$(M^T M)c = M^T z_{SS}, \tag{B.2}$$

where M^T is the transpose of M, and $(M^T M)$ is invertible (in principle if M is full rank). The unique

solution for the coefficients c gives a least-square fit of $\tilde{z}$ to z_{SS}.

The parabolic polynomial fits well to features of the patch size, that is to length scales of about 50km. The roughness parameter r is therefore a measure for the abundance of smaller features. The lower limit of the topographic length scale is set by the resolution of the Smith and Sandwell bathymetry, which is $2\pi \times depth$ for the bulk of the bathymetry that is obtained from satellite gravity anomaly measurements Morris et al. [2001]. So we expect $r(x, y)$ to reflect roughness at 15-50km length scales.

Appendix C

Bootstrap resampling

The bootstrap method is a non-parametric method to estimate the standard deviation of a statistic. The method is based on a large number of random draws with replacement from the data set, where 'replacement' means that the same sample may be drawn multiple times. How bootstrap resampling can be used to assess the robustness of a statistic is best illustrated with an example. The bootstrap recipe to estimate the standard deviation of for example the mean μ of dataset $X = [x_1, x_2, \ldots, x_N]$ is,

1. randomly sample N elements $\hat{x}_1, \hat{x}_2, \ldots, \hat{x}_N$ from X *with replacement*,
2. calculate the mean $\hat{\mu}$ of the bootstrap sample $\hat{X}$,
3. repeat step 1 and 2 B times
4. calculate the standard deviation of $\hat{\mu}_1, \hat{\mu}_2, \ldots, \hat{\mu}_B$.

See for example Martinez and Martinez [2002] for a more comprehensive discussion about bootstrapping.

Bibliography

Matthew H. Alford. Improved global maps and 54-year history of wind-work on ocean inertial motions. *Geophysical Research Letters*, 30(8):1424+, April 2003.

E. D. Barton and A. E. Hill. Abyssal flow through the amirante trench (western indian ocean). *Deep Sea Research Part A. Oceanographic Research Papers*, 36(7):1121–1126, July 1989.

L. Beal and H. Bryden. Observations of an agulhas undercurrent. *Deep Sea Research Part I: Oceanographic Research Papers*, 44(9-10):1715–1724, September 1997.

L. M. Beal, A. Ffield, and A. L. Gordon. Spreading of red sea overflow waters in the indian ocean. *Journal of Geophysical Research*, 105:8549–8564, 2000.

T. H. Bell. Topographically generated internal waves in the open ocean. *Journal of Geophysical Research*, 80(3):null+, 1975.

Amy S. Bower, Heather D. Hunt, and James F. Price. Character and dynamics of the red sea and persian gulf outflows. *Journal of Geophysical Research*, 105 (C3):6387–6414, 2000.

N. A. Bray and N. P. Fofonoff. Available potential energy for mode eddies. *Journal of Physical Oceanography*, 11(1), 1981.

W. S. Broecker. The great ocean conveyor. *Oceanography*, 4, 1991.

H. L. Bryden and A. J. Nurser. Effects of strait mixing on ocean stratification. *Journal of Physical Oceanography*, 33(8), 2003.

Harry L. Bryden. Rrs charles darwin cruise 139, 01 mar-15 apr 2002. trans-indian hydrographic section across 32s, 2003.

Harry L. Bryden and Lisa M. Beal. Role of the agulhas current in indian ocean circulation and associated heat and freshwater fluxes. *Deep Sea Research Part I: Oceanographic Research Papers*, 48(8):1821–1845, August 2001.

Harry L. Bryden, Lisa M. Beal, and Louise M. Duncan. Structure and transport of the agulhas current and its temporal variability. *Journal of Oceanography*, 61(3):479–492, June 2005.

J. L. Cairns and G. O. Williams. Internal wave observations from a midwater float, 2. *Journal of Geophysical Research*, 81:1943–1950, April 1976.

M. Dengler and D. Quadfasel. Equatorial deep jets and abyssal mixing in the indian ocean. *Journal of Physical Oceanography*, 32(4), 2002.

K. Donohue and J. Toole. A near-synoptic survey of the southwest indian ocean. *Deep Sea Research Part II: Topical Studies in Oceanography*, 50(12-13): 1893–1931, July 2003.

Sybren S. Drijfhout and Alberto C. Garabato. The zonal dimension of the indian ocean meridional overturning circulation. *Journal of Physical Oceanography*, 38(2):359–379, February 2008.

G. D. Egbert and R. D. Ray. Significant dissipation of tidal energy in the deep ocean inferred from satellite altimeter data. *Nature*, 405(6788):775–778, June 2000.

Ming Feng, Gary Meyers, Alan Pearce, and Susan Wijffels. Annual and interannual variations of the leeuwin current at 32s. *Journal of Geophysical Research*, 108(C11):3355+, November 2003.

Raffaele Ferrari and Carl Wunsch. Ocean circulation kinetic energy: Reservoirs, sources, and sinks. *Annual Review of Fluid Mechanics*, 41(1):253–282, 2009.

B. Ferron, H. Mercier, K. Speer, A. Gargett, and K. Polzin. Mixing in the romanche fracture zone. *Journal of Physical Oceanography*, 28(10), 1998.

Bruno Ferron and Jochem Marotzke. Impact of 4d-variational assimilation of woce hydrography on the meridional circulation of the indian ocean. *Deep Sea Research Part II: Topical Studies in Oceanography*, 50(12-13):2005–2021, July 2003.

M. Fieux, C. Andrie, P. Delecluse, A. G. Ilahude, A. Kartavtseff, F. Mantisi, R. Molcard, and J. C. Swallow. Measurements within the pacific-indian oceans throughflow region. *Deep Sea Research Part I: Oceanographic Research Papers*, 41(7):1091–1130, July 1994.

M. Fieux, R. Molcard, and A. G. Ilahude. Geostrophic transport of the pacific-indian oceans throughflow. *Journal of Geophysical Research*, 101(C5):12421–12432, 1996.

T. D. Finnigan, D. S. Luther, and R. Lukas. Observations of enhanced diapycnal mixing near the hawai-

ian ridge. *Journal of Physical Oceanography*, 32(11): 2988–3002, November 2002.

S. M. Flatté, R. Dashen, W. H. Munk, K. M. Watson, and F. Zachariasen. *Sound Transmission through a Fluctuating Ocean*. Cambridge University Press, 1 edition, June 1979. ISBN 052121940X.

L. Fu. Mass, heat and freshwater fluxes in the south indian ocean. *Journal of Physical Oceanography*, 16 (10), 1986.

A. Ganachaud and C. Wunsch. Large-scale ocean heat and freshwater transports during the world ocean circulation experiment. *Journal of Climate*, 16, 2002.

Alexandre Ganachaud. Large-scale mass transports, water mass formation, and diffusivities estimated from world ocean circulation experiment (woce) hydrographic data. *Journal of Geophysical Research*, 108(C7), 2003.

Alexandre Ganachaud and Carl Wunsch. Improved estimates of global ocean circulation, heat transport and mixing from hydrographic data. *Nature*, 408 (6811):453–457, November 2000.

C. Garrett and W. Munk. Space-time scales of internal waves. *Geophysical Fluid Dynamics*, 2:225–264, 1972.

C. Garrett and W. Munk. Space-time scales of internal waves: A progress report. *Journal of Geophysical Research*, 80:291–298, January 1975.

U. Garternicht and F. Schott. Heat fluxes of the indian ocean from a global eddy-resolving model. *Journal of Geophysical Research*, 102(C9):21147–21159, 1997.

M. C. Gregg. Scaling turbulent dissipation in the thermocline. *Journal of Geophysical Research*, 94:9686–9698, July 1989.

Michael C. Gregg, Thomas B. Sanford, and David P. Winkel. Reduced mixing from the breaking of internal waves in equatorial waters. *Nature*, 422(6931): 513–515, April 2003.

Susan L. Hautala, Janet Sprintall, James T. Potemra, Jackson C. Chong, Wahyu Pandoe, Nan Bray, and Gani A. Ilahude. Velocity structure and transport of the indonesian throughflow in the major straits restricting flow into the indian ocean. *Journal of Geophysical Research*, 106(C9):19527–19546, 2001.

F. S. Henyey, J. Wright, and S. M. Flatté. Energy and action flow through the internal wave field: an eikonal approach. *Journal of Geophysical Research*, 91:8487–8496, July 1986.

D. R. Jackett and T. J. McDougall. A neutral density variable for the world's oceans. *Journal of Physical Oceanography*, 27(2), 1997.

Gregory C. Johnson, David L. Musgrave, Bruce A. Warren, Amy Ffield, and Donald B. Olson. Flow of bottom and deep water in the amirante passage and mascarene basin. *Journal of Geophysical Research*, 103(C13):null+, 1998.

A. Klocker and T. McDougall. Water-mass transformation and ocean energetics in a nonlinear ocean. *Journal of Physical Oceanography*, submitted 2009.

A. Koch-Larrouy, G. Madec, P. Bouruet-Aubertot, T. Gerkema, L. Bessières, and R. Molcard. On the transformation of pacific water into indonesian throughflow water by internal tidal mixing. *Geophysical Research Letters*, 2006.

E. Kunze. Internal waves in an inhomogeneous ocean. Lecture notes, 2000.

E. Kunze, M. G. Briscoe, and A. J. Williams. Interpreting shear and strain fine structure from a neutrally buoyant float. *J. Geophys. Res.*, 95:18111–18125, October 1990.

E. Kunze, E. Firing, J. M. Hummon, T. K. Chereskin, and A. M. Thurnherr. Global abyssal mixing inferred from lowered adcp shear and ctd strain profiles. *Journal of Physical Oceanography*, 36(8), 2006.

Eric Kunze, Leslie K. Rosenfeld, Glenn S. Carter, and Michael C. Gregg. Internal waves in monterey submarine canyon. *Journal of Physical Oceanography*, 32(6):1890–1913, June 2002.

J. R. Ledwell, E. T. Montgomery, K. L. Polzin, L. C. St. Laurent, R. W. Schmitt, and J. M. Toole. Evidence for enhanced mixing over rough topography in the abyssal ocean. *Nature*, 403(6766):179–182, January 2000.

T. Lee and J. Marotzke. Inferring meridional mass and heat transports of the indian ocean by fitting a general circulation model to climatological data. *Journal of Geophysical Research - Oceans*, 102(C5): null–10602, May 1997.

Richard Lindzen. Wave-mean flow interactions in the upper atmosphere. *Boundary-Layer Meteorology*, 4 (1):327–343, April 1973.

Rick Lumpkin and Kevin Speer. Global ocean meridional overturning. *Journal of Physical Oceanography*, 37(10):2550–2562, 2007.

Leo R. Maas, Dominique Benielli, Joel Sommeria, and Frans. Observation of an internal wave attractor in

a confined, stably stratified fluid. *Nature*, 388(6642): 557–561, 1997.

Alison M. Macdonald. The global ocean circulation: a hydrographic estimate and regional analysis. *Progress In Oceanography*, 41(3):281–382, June 1998.

J. A. MacKinnon. Hyperviscosity. Notes, January 2003.

J. A. MacKinnon and M. C. Gregg. Mixing on the late-summer new england shelf—solibores, shear, and stratification. *Journal of Physical Oceanography*, 33(7):1476–1492, July 2003.

J. A. MacKinnon and K. B. Winters. Subtropical catastrophe: Significant loss of low-mode tidal energy at 28.9. *Geophysical Research Letters*, 32(15): L15605+, August 2005.

J. A. MacKinnon, T. M. S. Johnston, and R. Pinkel. Strong transport and mixing of deep water through the southwest indian ridge. *Nature Geosci*, 1(11): 755–758, November 2008.

Wendy L. Martinez and Angel R. Martinez. *Computational Statistics Handbook with MATLAB*. Chapman & Hall/CRC, 2002.

S. Matt and W. Johns. Transport and entrainment in the red sea outflow plume. *Journal of Physical Oceanography*, 37(4), 2006.

C. Mauritzen, K. L. Polzin, M. S. Mccartney, R. C. Millard, and D. E. West-Mack. Evidence in hydrography and density fine structure for enhanced vertical mixing over the mid-atlantic ridge in the western atlantic. *Journal of Geophysical Research (Oceans)*, 107:11–1, October 2002.

Mary C. McCarthy, Lynne D. Talley, and Molly O. Baringer. Deep upwelling and diffusivity in the southern central indian basin. *Geophysical Research Letters*, 24(22):null+, 1997.

C. Henry McComas and Peter Müller. The dynamic balance of internal waves. *Journal of Physical Oceanography*, 11(7):970–986, July 1981.

E. McDonagh, H. Bryden, B. King, and R. Sanders. The circulation of the indian ocean at 32s. *Progress In Oceanography*, 79(1):20–36, October 2008.

Michele Y. Morris, Melinda M. Hall, Louis C. St. Laurent, and Nelson G. Hogg. Abyssal mixing in the brazil basin*. *Journal of Physical Oceanography*, 31 (11):3331–3348, November 2001.

Joanna E. Muench and Eric Kunze. Internal wave interactions with equatorial deep jets. part i: Momentum-flux divergences. *Journal of Physical Oceanography*, 29(7):1453–1467, July 1999.

Joanna E. Muench and Eric Kunze. Internal wave interactions with equatorial deep jets. part ii: Acceleration of the jets. *Journal of Physical Oceanography*, 30(8):2099–2110, August 2000.

W. H. Munk. Abyssal recipes. *Deep Sea Research Part I: Oceanographic Research Papers*, 13, 1966.

Walter Munk and Carl Wunsch. Abyssal recipes ii: energetics of tidal and wind mixing. *Deep Sea Research Part I: Oceanographic Research Papers*, 45 (12):1977–2010, December 1998.

S. P. Murray and W. Johns. Direct observations of seasonal exchange through the bab el mandab strait. *Geophysical Research Letters*, 24:2557–2560, November 1997.

A. C. Naveira-Garabato, K. L. Polzin, B. A. King, K. J. Heywood, and M. Visbeck. Widespread intense turbulent mixing in the southern ocean. *Science*, 303 (5655):210–213, 2004a.

Alberto Naveira-Garabato, Kevin I. C. Oliver, Andrew J. Watson, and Marie-José Messias. Turbulent diapycnal mixing in the nordic seas. *Journal of Geophysical Research*, 109:C12010+, December 2004b.

Maxim Nikurashin and Raffaele Ferrari. Radiation and dissipation of internal waves generated by geostrophic motions impinging on small-scale topography: Theory. *Journal of Physical Oceanography*, preprint(2009):0000, November 2009.

J. Nycander. Generation of internal waves in the deep ocean by tides. *Journal of Geophysical Research - Oceans*, 110(C10):C10028+, October 2005.

T. R. Osborn. Estimates of the local rate of vertical diffusion from dissipation measurements. *Journal of Physical Oceanography*, 10(1), 1980.

M. D. Palmer, A. C. Naveira-Garabato, J. D. Stark, J. M. Hirschi, and J. Marotzke. The influence of diapycnal mixing on quasi-steady overturning states in the indian ocean. *Journal of Physical Oceanography*, 37(9), 2007.

W. R. Peltier and C. P. Caulfield. Mixing efficiency in stratified shear flows. *Annual Review of Fluid Mechanics*, 35(1), 2003.

A. Plueddemann and J. Farrar. Observations and models of the energy flux from the wind to mixed-layer inertial currents. *Deep Sea Research Part II: Topical Studies in Oceanography*, 53(1-2):5–30, January 2006.

K. Polzin, E. Kunze, J. Hummon, and E. Firing. The finescale response of lowered adcp velocity profiles. *Journal of Atmospheric and Oceanic Technology*, 19 (2), 2002.

K. L. Polzin. Finescale parameterizations of turbulent dissipation. *Journal of Physical Oceanography*, 25 (3), 1995.

K. L. Polzin, K. G. Speer, J. M. Toole, and R. W. Schmitt. Intense mixing of antarctic bottom water in the equatorial atlantic ocean. *Nature*, 380(6569): 54–57, March 1996.

K. L. Polzin, J. M. Toole, J. R. Ledwell, and R. W. Schmitt. Spatial variability of turbulent mixing in the abyssal ocean. *Science*, 276(5309):93–96, April 1997.

K. L. Polzin, A. C. Naveira-Garabato, and T. N. Huussen. Finescale parameterizations and other minutia. 2010.

J. F. Price and M. O. Baringer. Outflows and deep water production by marginal seas. *Progress In Oceanography*, 33(3):161–200, 1994.

Paul E. Robbins and John M. Toole. The dissolved silica budget as a constraint on the meridional overturning circulation of the indian ocean. *Deep Sea Research Part I: Oceanographic Research Papers*, 44 (5):879–906, May 1997.

William J. Schmitz. On the interbasin-scale thermohaline circulation. *Reviews of Geophysics*, 33(2):null+, 1995.

R. Scott and Y. Xu. An update on the wind power input to the surface geostrophic flow of the world

ocean. *Deep Sea Research Part I: Oceanographic Research Papers*, 56(3):295–304, March 2009.

Bernadette M. Sloyan and Stephen R. Rintoul. The southern ocean limb of the global deep overturning circulation. *Journal of Physical Oceanography*, 31 (1), 2001.

M. B. Sloyan. Antarctic bottom and lower circumpolar deep water circulation in the eastern indian ocean. *Journal of Geophysical Research*, 111, 2006.

Walter H. F. Smith and David T. Sandwell. Global sea floor topography from satellite altimetry and ship depth soundings. *Science*, 277(5334):1956–1962, September 1997.

Louis C. St Laurent and Andreas M. Thurnherr. Intense mixing of lower thermocline water on the crest of the mid-atlantic ridge. *Nature*, 448(7154):680–683, August 2007.

S. A. Thorpe. Dissipation in hydraulic transitions in flows through abyssal channels. *Journal of Marine Research*, 65(1), 2007.

A. M. Thurnherr. Diapycnal mixing associated with an overflow in a deep submarine canyon. *Deep Sea Research Part II: Topical Studies in Oceanography*, 53:194–206, 2006.

A. M. Thurnherr, L. C. St. Laurent, K. G. Speer, J. M. Toole, and J. R. Ledwell. Mixing associated with sills in a canyon on the midocean ridge flank*. *Journal of Physical Oceanography*, 35(8):1370–1381, August 2005.

J. R. Toggweiler and B. Samuels. On the ocean's large-scale circulation near the limit of no vertical mixing. *Journal of Physical Oceanography*, 28(9), 1998.

John M. Toole and Bruce A. Warren. A hydrographic section across the subtropical south indian ocean. *Deep Sea Research Part I: Oceanographic Research Papers*, 40(10):1973–2019, October 1993.

S. Wacongne and R. Pacanowski. Seasonal heat transport in a primitive equations model of the tropical indian ocean. *Journal of Physical Oceanography*, 26 (12), 1996.

B. Warren. Bottom water transport through the southwest indian ridge. *Deep Sea Research*, 25(3): 315–321, March 1978.

B. Warren and G. Johnson. The overflows across the ninetyeast ridge. *Deep Sea Research Part II: Topical Studies in Oceanography*, 49(7-8):1423–1439, 2002.

D. J. Webb and N. Suginohara. Oceanography: Vertical mixing in the ocean. *Nature*, 409(6816):37, January 2001.

K. B. Winters and E. A. D'Asaro. Two-dimensional instability of finite amplitude internal gravity wave packets near a critical level. *J. Geophys. Res.*, 94, 1989.

K. B. Winters and E. A. D'Asaro. Three-dimensional wave instability near a critical level. *Journal of Fluid Mechanics Digital Archive*, 272(-1):255–284, 1994.

K. B. Winters, J. A. MacKinnon, and B. Mills. A spectral model for process studies of rotating, density-stratified flows. *Journal of Atmospheric and Oceanic Technology*, 21(1):69–94, January 2004.

Kraig B. Winters and Eric A. D'Asaro. Direct simulation of internal wave energy transfer. *Journal of Physical Oceanography*, 27(9):1937–1945, September 1997.

Kraig B. Winters, Peter N. Lombard, James J. Riley, and Eric A. D'Asaro. Available potential energy and mixing in density-stratified fluids. *Journal of Fluid Mechanics Digital Archive*, 289(-1):115–128, 1995.

C. Wunsch and R. Ferrari. Vertical mixing, energy, and the general circulation of the oceans. *Annual Review of Fluid Mechanics*, 36(1):281–314, 2004.

C. Wunsch and B. Grant. Towards the general circulation of the north atlantic ocean. *Progress in Oceanography*, 11, 1982.

Carl Wunsch. *The Ocean Circulation Inverse Problem*. Cambridge University Press, 1996.

Carl Wunsch, Dunxin Hu, and Barbara Grant. Mass, heat, salt and nutrient fluxes in the south pacific ocean. *Journal of Physical Oceanography*, 13(5): 725–753, May 1983.

K. Q. Zhang. The importance of open-boundary estimation for an indian ocean gcm-data synthesis. *Journal of Marine Research*, pages 305–334, March 1999.